Broad-spectrum immune suppression encoded in self-amplifying RNA enables non-cytotoxic, non-immunostimulatory, reversible transgene expression

Tony K.Y Lim,[1,*] Anne Ritoux,[1] Luke W. Paine,[1] Larissa Ferguson,[2] and Ewan St. John Smith[1,**]
[1]Department of Pharmacology, University of Cambridge, Cambridge, UK
[2]MRC Laboratory of Molecular Biology, Cambridge, UK
*Correspondence: tony.ky.lim@gmail.com
**Correspondence: es336@cam.ac.uk

ABSTRACT

Self-amplifying RNA (saRNA) has the potential to provide durable, non-integrative transgene expression for transient gene therapy. However, its auto-replicative nature mimics viral infection, triggering innate immune responses that shutdown cap-dependent translation, degrade cellular mRNA, induce cell death, and release cytokines. In non-immunotherapy applications, this immune activation is undesirable as it limits transgene expression, depletes transfected cells, and damages surrounding tissues, undermining therapeutic outcomes. Moreover, the use of exogenous immune suppressants to mitigate these effects often increases treatment complexity and the risk of unintended systemic side effects. To address these challenges, we developed a strategy to encode broad-spectrum innate immune suppression directly within saRNA. This approach leverages cap-independent translation to bypass saRNA-triggered translation shutdown, enabling the expression of multiple inhibitors targeting diverse double-stranded RNA-sensing and inflammatory signaling pathways. In mouse primary fibroblast-like synoviocytes—a model relevant to inflammatory joint diseases—this strategy eliminates the need for external immune inhibitors, reduces cytotoxicity and antiviral cytokine secretion, and enables sustained transgene expression that is reversible with a small-molecule antiviral. These findings support the development of saRNA therapeutics that offer durable, non-integrative, controllable transgene expression without persistent immune activation or reliance on exogenous immune suppressants.

GRAPHICAL ABSTRACT

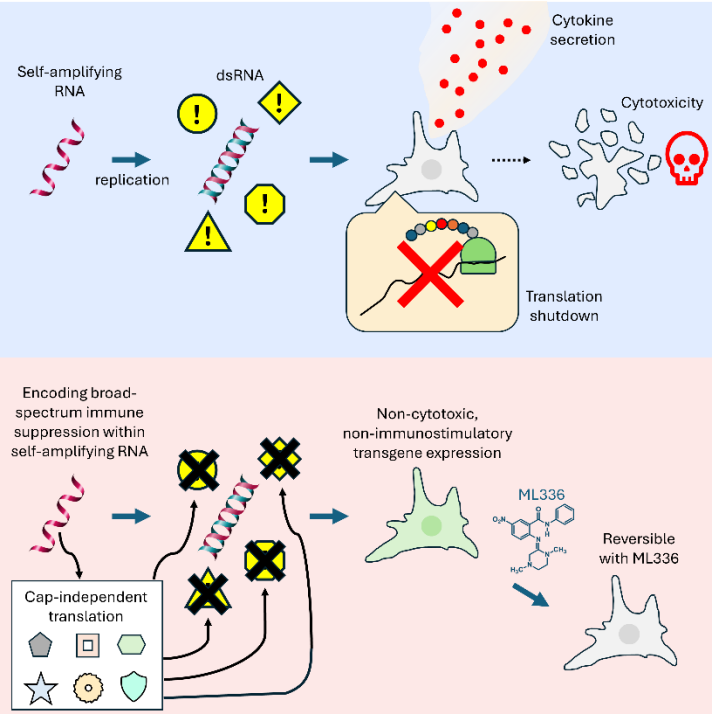

ETOC SYNOPSIS

Targeting diverse double-stranded RNA sensing and inflammatory pathways with cap-independently expressed proteins cis-encoded within self-amplifying RNA enables non-cytotoxic, non-immunostimulatory, and reversible transgene expression in mouse primary fibroblast-like synoviocytes.

INTRODUCTION

Self-amplifying RNA (saRNA) is a promising platform for transient gene therapy due to its ability to encode large therapeutic payloads and achieve sustained, non-integrative protein expression.[1] Upon cellular internalization, saRNA utilizes host machinery to synthesize an RNA-dependent RNA polymerase (RdRp), which drives replication of the saRNA genome.[2] This process involves the production of a negative-strand RNA intermediate that serves as a template for both genomic and subgenomic RNA synthesis.[3] Subgenomic RNA, encoding the gene of interest, is transcribed in excess of the genomic RNA, leading to robust and sustained protein expression.[4]

However, the self-replication of saRNA also generates double-stranded RNA (dsRNA) intermediates, formed both during the synthesis of negative-strand RNA and during the transcription of positive-strand RNA from the negative-strand template.[3] These dsRNA intermediates are potent activators of cytosolic pattern recognition receptors, triggering innate immune responses.[5,6] This recognition results in suppression of cap-dependent translation,[7–10] degradation of cellular mRNA,[6,11] induction of programmed cell death,[6,10,12–16] and release of cytokines and chemokines characteristic of viral infection[9,17,18]. While this innate immune stimulation can enhance the efficacy of immunotherapy applications such as vaccines and cancer therapy,[19] excessive stimulation can undermine potency by reducing antigen expression,[17] necessitating strategies to reduce the immunostimulatory effects of saRNA.[20] In non-immunotherapy applications, sustained activation of innate immune pathways is particularly problematic, as it limits transgene expression, depletes transfected cells, and induces inflammation. While exogenous immunosuppressants can mitigate these effects and restore transgene expression,[9,21–23] they add complexity to treatment regimens and increase the risk of unintended side effects.

Strategies to mitigate saRNA-mediated innate immune responses have included the incorporation of modified nucleotides[24], removal of dsRNA contaminants,[9,25] and co-delivery of non-replicating mRNA encoding viral innate immune inhibiting proteins.[22,26,27] While these approaches can reduce initial innate immune responses to saRNA transfection, they fall short in addressing the continuous immune activation triggered by dsRNA intermediates that arise during saRNA replication.[2] Sequence evolution of the RdRp replicon shows some promise in reducing these responses, but even engineered replicons still induce significant innate immune activation.[6,28] Another strategy involves encoding a viral immune inhibitor within the saRNA construct using a 2A self-cleaving peptide, which improves protein expression in vitro but does not significantly reduce cytokine responses, despite reductions in NF-κB and IRF3 activation.[19]

Building on these insights, we developed a fully saRNA-based approach to mitigate ongoing saRNA-induced innate immune responses. Our strategy incorporates several key innovations. First, innate immune inhibitory proteins are expressed via cap-independent translation, bypassing the cap-dependent translation shutdown commonly triggered by saRNA. Cap-dependent translation requires the presence of a 5′ cap structure on mRNA, which recruits translation initiation factors and ribosomes.[29] By contrast, cap-independent translation uses alternative mechanisms—such as internal ribosome entry sites (IRES)—to recruit ribosomes directly to the mRNA, enabling translation even when cap-dependent pathways are inhibited.[30] Second, by simultaneously targeting multiple dsRNA-sensing and inflammatory signaling pathways, our method provides a more comprehensive suppression of innate immune responses than single target approaches. Third, encoding innate immune inhibitors directly within the saRNA ensures continuous protection against persistent innate immune activation caused by dsRNA intermediates during saRNA replication, eliminating the need for exogenous immunosuppressants.

We evaluated this approach in mouse primary fibroblast-like synoviocytes (FLS), a key cell type in the pathology of inflammatory joint diseases.[31,32] To facilitate this evaluation, we developed a novel microplate assay for straightforward, longitudinal monitoring of saRNA translation control and cytotoxicity in live cells. Our results demonstrate that this strategy effectively reduces saRNA-induced cytotoxicity and cytokine production while enabling sustained cap-dependent transgene expression, which can be

reversed with a small-molecule antiviral. These results pave the way for saRNA-based therapies that offer durable, controllable transgene expression with minimal innate immune activation, achieving this without reliance on exogenous immunosuppressants.

RESULTS

Development of a microplate assay for longitudinal monitoring of translational control and cell number

Since saRNA can induce cap-dependent translation shutdown and cell death, we developed a microplate assay to simultaneously monitor cap-independent translation, cap-dependent translation, and cell number over time. In this assay, primary mouse FLS (Fig. S1) were plated in 6-well plates and transfected with saRNA constructs that used the Venezuelan equine encephalitis virus (VEEV) RdRp to self-replicate. These constructs featured a dual-fluorescence design, with EGFP expressed through encephalomyocarditis virus (EMCV) IRES-mediated, cap-independent translation, and mScarlet3 expressed through subgenomic cap-dependent translation. This dual-reporter system enabled assessment of the effects of saRNA on translational control (Fig. 1a). Spectral overlap between EGFP and mScarlet3 was corrected using linear unmixing (Figs. S2a-c).

To monitor cell number, FLS were stained with BioTracker NIR680, a lipophilic carbocyanine membrane dye that enables long-term fluorescent labeling of cells.[33] Carbocyanine dyes like BioTracker are weakly fluorescent in aqueous solution but exhibit high fluorescence when integrated into lipid bilayers. Consequently, mock transfection with Lipofectamine MessengerMAX—a lipid transfection agent—enhanced BioTracker fluorescence compared to non-transfected cells, likely due to an interaction with the lipid components of Lipofectamine (Figs. S3a, S3b). Despite this interaction, BioTracker remains effective for indicating cell number, as treatment of mock transfected cells with the apoptosis inducer staurosporine[34] reduced BioTracker fluorescence (Figs. S3a, S3b). The BioTracker results were consistent with those obtained using the viability dye calcein AM (Figs. S3c, S3d), with the added advantages of eliminating the need for additional staining and wash steps and avoiding spectral overlap with red and green fluorescent proteins. This assay allows for seamless longitudinal monitoring of cap-independent translation, cap-dependent translation, and cell number using microplate readers or imagers.

Design of saRNA constructs for inhibiting multiple dsRNA sensing pathways

Cells detect cytosolic dsRNA through several sensing pathways, including RIG-I,[35] melanoma differentiation-associated protein 5 (MDA-5),[36] protein kinase R (PKR),[37] and the oligoadenylate synthase (OAS)/RNase L pathway.[38] To broadly inhibit these pathways, we designed an saRNA construct, referred to as ‘E3’, that utilizes EMCV IRES cap-independent translation to express the vaccinia virus E3 protein (Fig. 1a). E3 protein is a pleiotropic inhibitor that binds and sequesters dsRNA, effectively blocking multiple dsRNA sensing pathways.[39]

Given the key roles of PKR in cap-dependent translation shutdown and OAS/RNase L in cellular mRNA degradation in response to dsRNA, we sought to further inhibit these pathways in a second construct. This construct includes Toscana virus NSs, a ubiquitin ligase that promotes PKR degradation,[40] and Theiler’s virus L*, which inhibits RNase L.[41] To enable co-expression of these three proteins—E3, NSs, and L*—we incorporated 2A “self-cleaving” peptide sequences between the proteins, allowing the polyprotein to be cleaved into separate proteins during translation. As prior experiments showed that using multiple identical 2A peptides can reduce protein expression,[42] we selected non-identical 2A peptides for this construct. This construct, named ‘E3-NSs-L*’, is expected to provide a more comprehensive inhibition of dsRNA-sensing pathways than the E3 construct.

Finally, as a control, we designed a ‘native saRNA’ construct that expresses a blue fluorescent protein (moxBFP) as a visual marker of IRES functionality in place of inhibitors of dsRNA-sensing pathways. Importantly, moxBFP expression did not overlap spectrally with the EGFP or mScarlet3 channels (Figs. S2a-c).

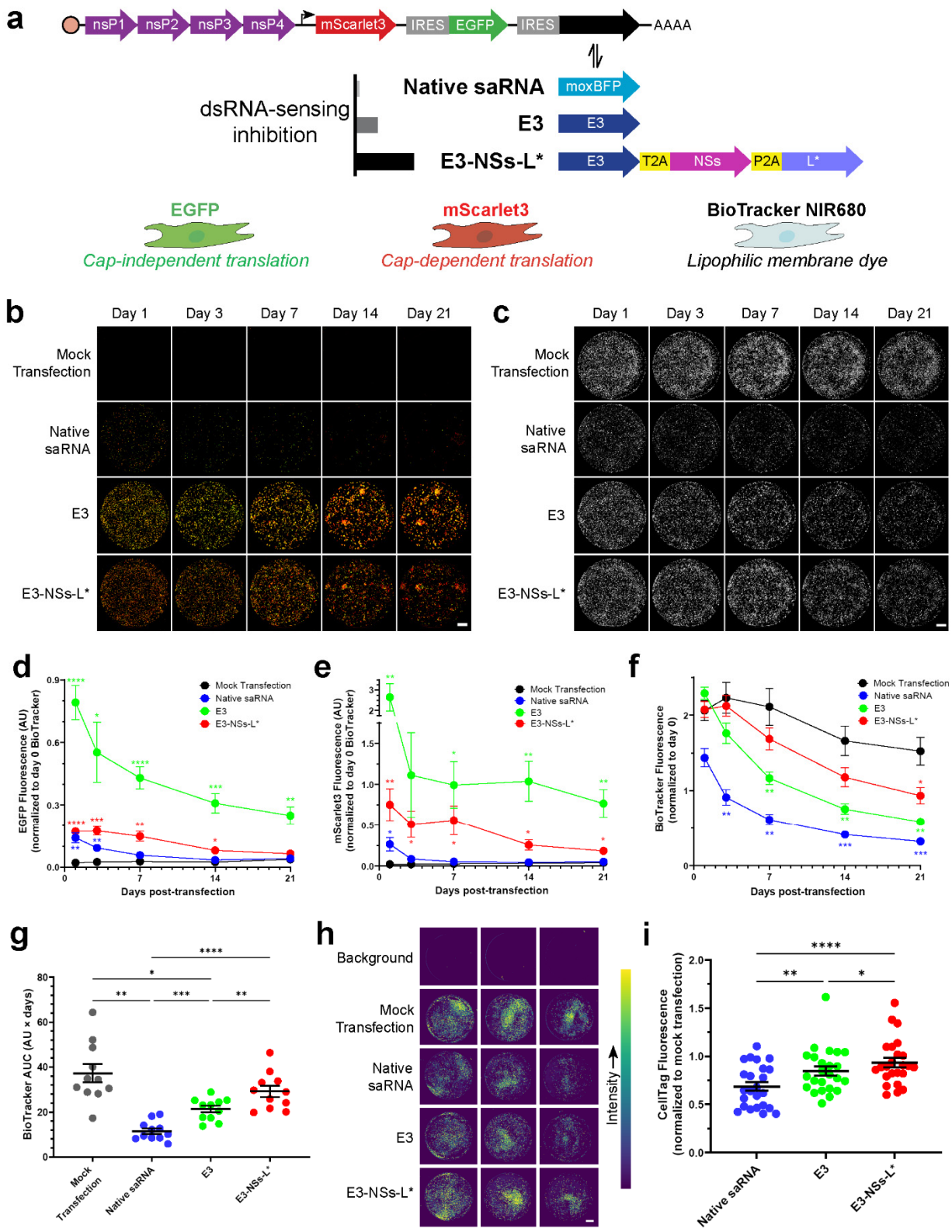

Fig. 1. Differential effects of moderate and strong dsRNA-sensing pathway inhibition on saRNA transgene expression and cell loss

a, Schematic of the native saRNA, E3, and E3-NSs-L* constructs designed to inhibit dsRNA-sensing pathways and report saRNA transgene expression. The native saRNA construct lacks dsRNA-sensing inhibitors. The E3 construct expresses vaccinia virus E3, a pleiotropic inhibitor of dsRNA sensing, expected to provide moderate inhibition. The E3-NSs-L* construct expresses vaccinia virus E3, and additionally includes Toscana virus NSs and Theiler's virus L*, which target the PKR and OAS/RNase L pathways, expected to provide strong inhibition. EGFP is expressed via an IRES to report cap-independent translation, while a subgenomic promoter (depicted with an angled arrow) enables transcription of an RNA transcript that expresses mScarlet3 via cap-dependent translation. saRNA constructs were transfected into primary mouse FLS, which were labeled with BioTracker to monitor cell number.
b, Representative images of EGFP (green) and mScarlet3 (red) expression in FLS transfected with native saRNA, E3, or E3-NSs-L* over 3 weeks. Scale bar = 5 mm.
c, Representative images of FLS transfected with the same constructs, showing BioTracker intensity over time. Scale bar = 5 mm.
d, Quantification of EGFP fluorescence over time (n = 11). The E3 construct provided the greatest EGFP expression, while the E3-NSs-L* construct showed intermediate levels. Statistical significance of treatment effects at each time point compared to mock transfection was determined by two-way RM ANOVA with Greenhouse–Geisser correction and Dunnett's multiple comparisons test.
e, Quantification of mScarlet3 fluorescence over time (n = 11). The E3 construct provided the greatest mScarlet3 expression, while the E3-NSs-L* showed intermediate levels. Statistical significance of treatment effects at each time point compared to mock transfection was determined by two-way RM ANOVA with Greenhouse–Geisser correction and Dunnett's multiple comparisons test.
f, Quantification of BioTracker fluorescence over time (n = 11). The native saRNA and E3 constructs reduced BioTracker fluorescence, indicating cell loss. Statistical significance of treatment effects at each time point compared to mock transfection was determined by two-way RM ANOVA with Greenhouse–Geisser correction and Dunnett's multiple comparisons test.
g, AUC analysis of BioTracker fluorescence data shown in (f), summarizing cumulative effects over the time course (n = 11). Increasing dsRNA-sensing pathway inhibition prevents saRNA-induced reductions in integrated BioTracker signal. Statistical analysis was performed using one-way RM ANOVA with Greenhouse–Geisser correction and Tukey's multiple comparisons test to compare all groups. Mock transfection data is also presented in Fig. S5a.
h, Representative images of FLS stained with the cell number normalization dye, CellTag 700. Columns represent cells plated from the same biological replicate, while rows show different treatments. Scale bar = 2.5 mm.
i, Quantification of mock transfection normalized CellTag signal (n = 24). Increasing dsRNA-sensing pathway inhibition mitigates saRNA-induced reductions in CellTag signal. Statistical analysis was performed using one-way RM ANOVA with Greenhouse–Geisser correction and Holm-Šídák's multiple comparisons test to compare all groups. Assays were performed 2 days post-transfection. Data in this panel were pooled from in-cell western assays, incorporating data presented in Figs. 3 and 6 as well as additional data not shown elsewhere.
For all statistical reporting, *P < 0.05, **P < 0.01, ***P < 0.001 and ****P < 0.0001. Data are presented as mean ± SEM.
For panels (d-f): Data were normalized to starting cell number, indicated by BioTracker intensity on day 0, prior to transfection. The mock transfection control data is also presented in Figs. 5c-e.

Acronyms: saRNA, self-amplifying RNA; dsRNA, double-stranded RNA; nsP, Venezuelan equine encephalitis virus non-structural protein; IRES, encephalomyocarditis virus internal ribosome entry site; moxBFP, monomeric oxidizing environment-optimized blue fluorescent protein; E3, Vaccinia virus E3 protein; NSs, Toscana virus non-structural NSs protein; L*, Theiler's murine encephalomyelitis virus L* protein; T2A, Thosea asigna virus 2A peptide; P2A, porcine teschovirus-1 2A peptide; PKR, protein kinase R; OAS, oligoadenylate synthase; AUC, area under the curve.

Moderate dsRNA-sensing pathway inhibition enables high transgene expression at the cost of cell loss, while strong inhibition preserves cell number at lower expression levels

Following transfection of saRNA constructs, we monitored BioTracker, EGFP, and mScarlet3 fluorescence over 3 weeks (Figs. 1b, 1c). Inhibiting dsRNA-sensing pathways with viral proteins

184 significantly enhanced saRNA transgene expression (Figs. 1d, 1e). Interestingly, the E3 construct
185 produced the highest levels of EGFP and mScarlet3 expression, surpassing both native saRNA and the
186 E3-NSs-L* construct. Native saRNA yielded low levels of transgene expression, while E3-NSs-L* showed
187 intermediate expression.

188 Achieving durable transgene expression depends equally on preserving cell viability and maximizing
189 transgene expression, as constructs that induce cell death undermine the goal of sustained transgene
190 expression. Transfection of FLS with native saRNA caused both immediate and long-term reductions in
191 cell number, as indicated by BioTracker intensity (Fig. 1f). While the E3 construct initially maintained cell
192 number, BioTracker signals gradually diminished over time. In contrast, the E3-NSs-L* construct provided
193 sustained protection against the decline in cell number. To quantify the cumulative effects of different
194 saRNA constructs on cell number over the experimental time course, we performed area under the curve
195 (AUC) analysis, demonstrating that E3-NSs-L* significantly protected against a decline in cell number
196 compared to the E3 construct (Fig. 1g). These findings were further supported by experiments using
197 CellTag, a cell number normalization stain (Fig. 1h), which revealed that increasing dsRNA-sensing
198 pathway inhibition protects against cell loss (Fig. 1i). Together, these results suggest that while the E3
199 construct effectively enhances saRNA transgene expression, it is associated with greater cell loss,
200 underscoring the advantage of the E3-NSs-L* construct for applications requiring sustained, non-cytotoxic
201 gene expression.

202 *Inhibiting dsRNA sensing pathways reduces saRNA-induced cytotoxicity and improves cell*
203 *viability*

204 saRNA is known to induce programmed cell death,[6,10,12–16] which often leads to cell detachment.[43] Thus
205 reductions in BioTracker signal following saRNA treatment are likely indicative of this process. However,
206 since BioTracker is a lipophilic membrane dye, the reduction in signal may not necessarily correlate with
207 cell viability or cytotoxicity. In addition to long-term cell tracking, lipophilic membrane dyes like BioTracker
208 are often used to stain extracellular vesicles, which bud off from the plasma membrane.[44] During cellular
209 stress, increased production of extracellular vesicles[45] could deplete the membrane-associated
210 BioTracker dye from cells, resulting in a lower detectable signal. Therefore, the observed reduction in
211 BioTracker signal could reflect enhanced extracellular vesicle production rather than cell death.

212 To provide more definitive evidence that inhibiting dsRNA-sensing pathways protects against saRNA-
213 induced cytotoxicity, we conducted a longitudinal assay with annexin V staining over 6 days (Fig. 2a),
214 followed by calcein AM staining on day 7 (Fig. 2b). Annexin V, a membrane-impermeable protein, binds
215 to phosphatidylserine, which translocates to the extracellular side of the cell membrane during early
216 apoptosis, enabling the detection of apoptotic cells with intact membranes.[46] If the membrane is
217 compromised, annexin V can enter cells and stain intracellular phosphatidylserine, indicating late
218 apoptosis or necrosis.[47] Calcein AM, a viability dye, accumulates in metabolically active cells with intact
219 membranes, serving both as a marker of live cell number and an indicator of membrane integrity.[48]

220 The apoptosis inducing agent staurosporine caused a transient increase in annexin V staining that
221 decreased after the first day (Fig. 2c), along with a marked reduction in calcein AM fluorescence
222 compared to mock transfection (Fig. 2d), observations that are consistent with extracellular
223 phosphatidylserine translocation and/or increased membrane permeability. Similarly, native saRNA
224 induced a temporary increase in annexin V staining during the first two days post-transfection (Fig. 2c)
225 accompanied by reduced calcein AM staining (Fig. 2d). Co-expression of E3 prevented the initial increase
226 in annexin V staining, but elevated it from day 2 onward, and also resulted in significantly reduced calcein
227 AM intensity (Figs. 2c, 2d). In contrast, E3-NSs-L* had no significant effect on annexin V or calcein AM
228 staining compared to mock transfection, supporting the idea that broader inhibition of dsRNA-sensing
229 pathways, achieved by combining E3, NSs and L*, is more effective than E3 alone in preventing saRNA-
230 induced cell death and preserving cell viability.

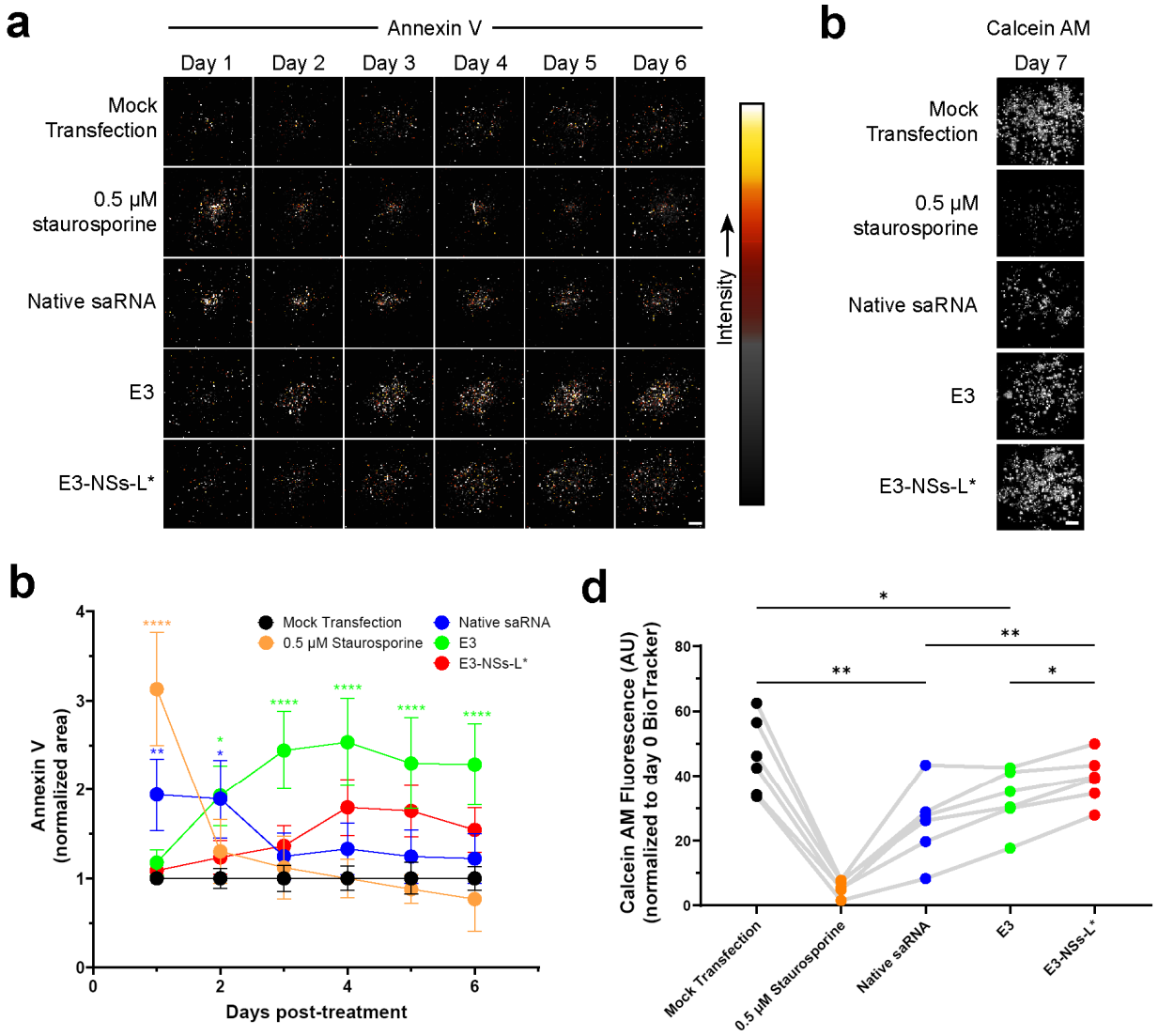

Fig. 2. saRNA induces increased phosphatidylserine staining and reduced viability, which is prevented by E3-NSs-L*

a, Representative cropped images of Annexin V-CF800 staining, indicating phosphatidylserine exposure or loss of membrane integrity, performed daily over 6 days using a microplate imager. Scale bar = 1.5 mm.
b, Representative cropped images of calcein AM staining, indicating viability, on day 7 post-treatment. Scale bar = 1.5 mm.
c, Annexin V staining, quantified as the area of positive pixels determined using Li thresholding (n = 6). Staurosporine, native saRNA, and the E3 construct significantly increased annexin V staining, while E3-NSs-L* did not. Data are normalized to the average of the mock transfection group. Statistical significance of treatment effects at each time point compared to mock transfection was determined using two-way RM ANOVA with Bonferroni's multiple comparisons test. Data are presented as mean ± SEM.
d, Calcein AM intensity measured on day 7 post-treatment (n = 6). Native saRNA, and E3 significantly reduced cell viability compared to mock transfection, while E3-NSs-L* did not. Cell viability in the E3-NSs-L* group was significantly higher than the E3 group. All groups differed significantly from staurosporine; these comparisons are omitted from the figure for clarity due to the large number of statistical comparisons. Data are normalized to cell number on day 0 as determined by BioTracker staining before transfection. Statistical significance was determined by one-way RM ANOVA with Greenhouse–Geisser

correction and Tukey's multiple comparisons test comparing all groups.
saRNA constructs used are shown in Fig. 1a. For all statistical reporting, *P < 0.05, **P < 0.01, ***P < 0.001 and ****P < 0.0001.

E3 and E3-NSs-L prevent saRNA-induced eIF2α phosphorylation and differentially regulate eIF2α levels*

We next explored how the E3 and E3-NSs-L* constructs influence translational control mechanisms during saRNA transfection. Eukaryotic initiation factor 2 alpha (eIF2α) is a central regulator of translation initiation; its phosphorylation serves as a cellular stress response to limit cellular cap-dependent protein synthesis, freeing ribosomes for cap-independent translation initiation instead.[49] Using in-cell western assays, we found that native saRNA transfection increased eIF2α phosphorylation, but both E3 and E3-NSs-L* effectively blocked this phosphorylation (Fig. 3a), consistent with previous reports of E3's inhibitory effect on eIF2α phosphorylation.[26] Interestingly, E3-NSs-L* also increased total eIF2α levels, an effect not observed with the E3 construct (Fig. 3b).

E3-NSs-L counteracts saRNA-induced PKR upregulation*

Given that PKR phosphorylates eIF2α upon activation by dsRNA,[7] we next assessed its levels following saRNA transfection. Consistent with previous reports,[6] native saRNA transfection increased PKR levels (Fig. 3c). The E3 construct similarly increased PKR levels; however, co-expression of E3-NSs-L* mitigated this increase, suggesting that E3-NSs-L* effectively counteracts saRNA-induced PKR upregulation. This is in line with the known role of the Toscana virus NSs protein as a ubiquitin ligase that targets PKR for degradation.[40]

saRNA reduces eIF4E phosphorylation without altering total eIF4E levels

We next examined the impact of saRNA transfection on eIF4E, a key regulator of translation initiation.[50] All constructs reduced eIF4E phosphorylation levels (Fig 3d), while total eIF4E levels remained unchanged (Fig. 3e).

E3-NSs-L preserves RNA integrity compared to E3*

Both the E3 and E3-NSs-L* constructs inhibited saRNA-induced eIF2α phosphorylation (Fig. 3a) and reduced eIF4E phosphorylation (Fig. 3d). However, E3-NSs-L* also reduced PKR levels (Fig. 3c) and increased total eIF2α availability for cap-dependent translation (Fig. 3b). Despite these advantages, the E3-NSs-L* construct unexpectedly produced lower levels of cap-dependent and cap-independent transgene expression compared to the E3 construct, suggesting that mechanisms beyond eIF2α and eIF4E-mediated translational control may contribute to the heightened transgene expression observed with the E3 construct.

When OAS binds dsRNA, it synthesizes 2′-5′-oligoadenylate, which activates RNase L to cleave single-stranded RNA, leading to cellular mRNA degradation[51] and inhibition of mRNA nuclear export,[52] thereby massively reducing host protein synthesis.[53] Many RNA viruses, including dengue and Zika, evade RNase L by localizing their transcripts within viral replication organelles, protecting them from degradation while allowing continued protein production.[52,54] Similarly, the VEEV-derived saRNA used in this study replicates within these organelles,[55] likely protecting its transcripts from RNase L activity. Consequently, RNase L activation by the E3 construct may selectively deplete cytoplasmic host mRNA while sparing saRNA. This depletion reduces competition for ribosomes, thereby enhancing the translation of saRNA transcripts. In contrast, the E3-NSs-L* construct encodes Theiler's virus L*, an RNase L inhibitor,[41] thereby preventing host mRNA degradation and forcing saRNA transcripts to compete directly with cellular mRNA for ribosomal access.

To test the hypothesis that RNase L activation by the E3 construct cleaves cellular mRNA, capillary gel electrophoresis was performed on RNA extracted from FLS transfected with the E3 and E3-NSs-L* constructs. RNA electropherograms were analyzed using the RNA integrity number (RIN) algorithm, an automated Bayesian learning method for measuring RNA integrity.[56] Cells transfected with E3-NSs-L* exhibited higher RIN than cells transfected with E3 (Fig. 3f), supporting the idea that RNase L-mediated reductions in cellular mRNA occur with the E3 construct but not with the E3-NSs-L* construct.

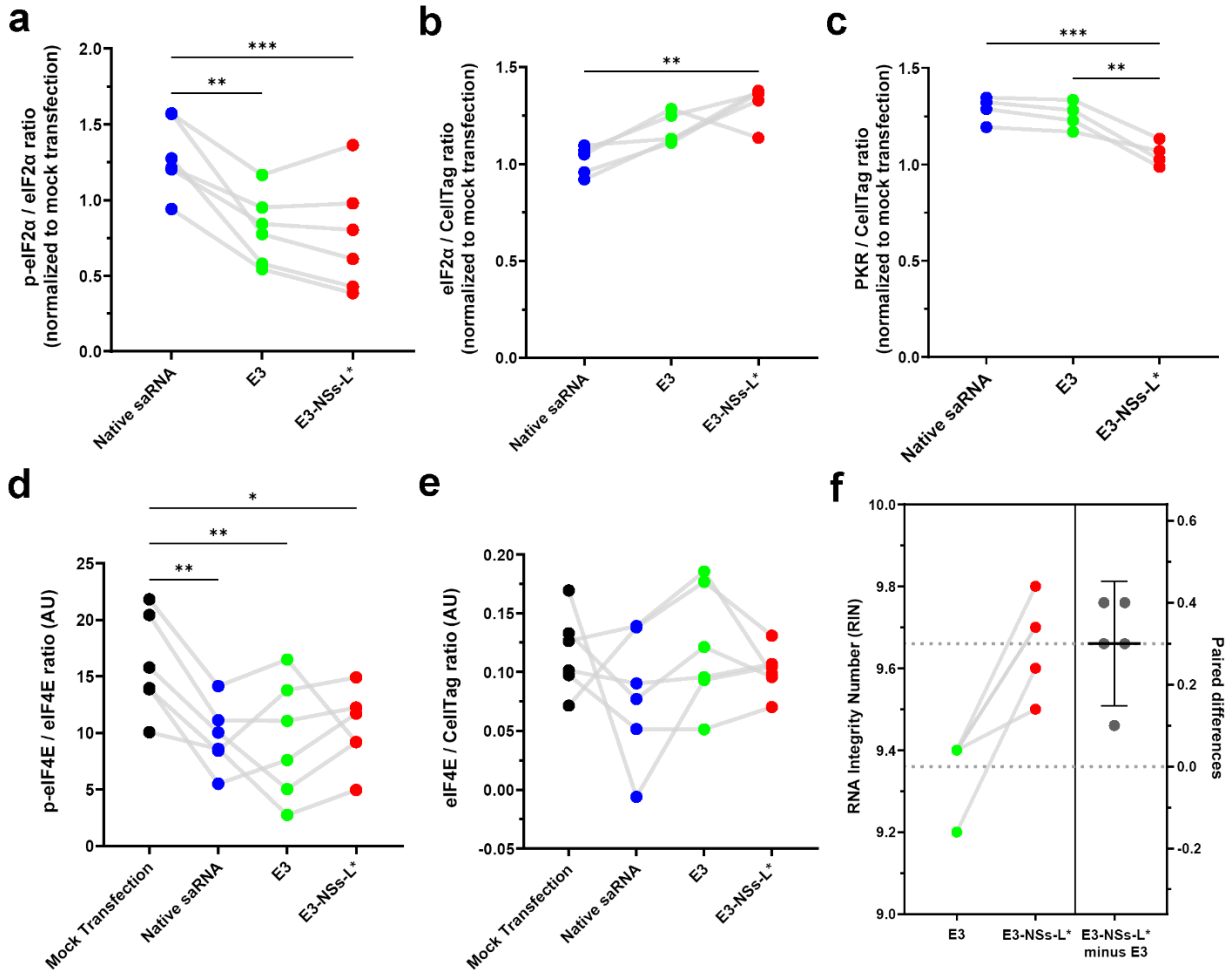

Fig. 3. Translational control alterations induced by saRNA are modulated by dsRNA-sensing pathway inhibitors with differing effects on RNA integrity

a, Phosphorylated eIF2α levels examined day 2 post-transfection by in-cell western assay (n = 6). Both E3 and E3-NSs-L* constructs significantly reduced eIF2α phosphorylation. Data are presented as fold-change relative to mock transfected cells. Statistical significance was determined by one-way RM ANOVA with Tukey's multiple comparisons test.
b, eIF2α levels examined day 2 post-transfection by in-cell western assay (n = 5). E3-NSs-L* significantly increased total eIF2α levels compared to native saRNA transfection. Data are presented as fold-change relative to mock transfected cells. Statistical significance was determined by one-way RM ANOVA with Tukey's multiple comparisons test.
c, PKR levels examined day 2 post-transfection by in-cell western assay (n = 4). E3-NSs-L* significantly reduced PKR levels compared to both native saRNA and E3 transfection. Data are presented as fold-change relative to mock transfected cells. Statistical significance was determined by one-way RM ANOVA with Tukey's multiple comparisons test.
d, Phosphorylated eIF4E levels examined day 2 post-transfection by in-cell western assay (n = 6). All saRNA constructs tested significantly reduced eIF4E phosphorylation levels compared to mock transfection. Statistical significance was determined by one-way RM ANOVA with Dunnett's multiple comparisons test comparing treatments to mock transfection.
e, eIF4E levels examined day 2 post-transfection by in-cell western assay (n = 6). One-way RM ANOVA revealed no significant differences between groups ($F(3,15) = 1.207$, $P = 0.3410$).
f, RNA integrity of FLS transfected with E3-NSs-L* is significantly higher than that of E3-transfected FLS (n = 5). RNA integrity was assessed using the RNA Integrity Number (RIN) algorithm, which ranges from

1 to 10, with 10 indicating fully intact RNA. RNA was extracted from FLS 1 day post-transfection. Data are shown as a Gardner-Altman comparison plot, with the right panel illustrating the mean effect size ± 95% CI. Statistical significance was assessed using a paired t-test (P = 0.0054).
saRNA constructs used are shown in Fig. 1a. Statistical significance is indicated as follows: *P < 0.05, **P < 0.01, ***P < 0.001. The mock transfection control data presented in panels (a), (b), (d) and (f) are also used in Fig. 6.

Design of saRNA constructs for inhibiting multiple inflammatory signaling pathways

Having addressed key saRNA-induced toxicities—including cell death, translation shutdown, and mRNA degradation—with the E3-NSs-L* construct, we next sought to design new saRNA constructs aimed at mitigating cytokine production. In these new constructs, E3-NSs-L*-EGFP was expressed via a single IRES using non-identical 2A peptides (Fig. 4a). On a second IRES, varying amounts of cellular inhibitors of inflammatory signaling were expressed. The control construct, called 'moxBFP', lacks cellular inhibitors of inflammatory signaling and instead expresses a blue fluorescent protein.

Given that activation of nuclear factor-κB (NF-κB) is a hallmark of viral infection and a master regulator of cytokine and chemokine induction,[57,58] we prioritized its inhibition using super repressor inhibitor of κBα (srIκBα). This dominant active form of IκBα cannot be phosphorylated and thus resists ubiquitination and degradation, forming a stable cytoplasmic pool of IκBα that prevents NF-κB nuclear translocation and downstream signaling.[59,60] We generated one construct expressing srIκBα alone (named 'srIκBα') and another expressing srIκBα in combination with Smad7 and suppressor of cytokine signaling 1 (SOCS1) using non-identical 2A peptides (named 'srIκBα-Smad7-SOCS1'). Smad7 negatively regulates both transforming growth factor-β (TGF-β) and NF-κB signaling pathways,[61] while SOCS1 inhibits type I, II, and III interferon (IFN) pathways as well as NF-κB signaling.[62–64]

Inhibiting dsRNA-sensing pathways and inflammatory signaling suppresses saRNA-induced cytokine secretion

Using a bead-based immunoassay on FLS culture supernatants, we observed that native saRNA transfection induced cytokine responses associated with viral infection (Figs. 4b, S4a-m). Cytokine secretion was still apparent when dsRNA-sensing pathways were inhibited, although a reduction in tumor necrosis factor (TNF)-α, IFN-α, and IFN-β levels were observed with E3 expression. Similarly, C-X-C motif chemokine ligand 10 (CXCL10) levels were reduced with E3-NSs-L* expression. On the other hand, srIκBα co-expression broadly suppressed cytokine secretion, reducing all measured cytokines to levels comparable to mock-transfected FLS. The srIκBα-Smad7-SOCS1 construct did not further reduce cytokine levels beyond the suppression achieved by srIκBα alone.

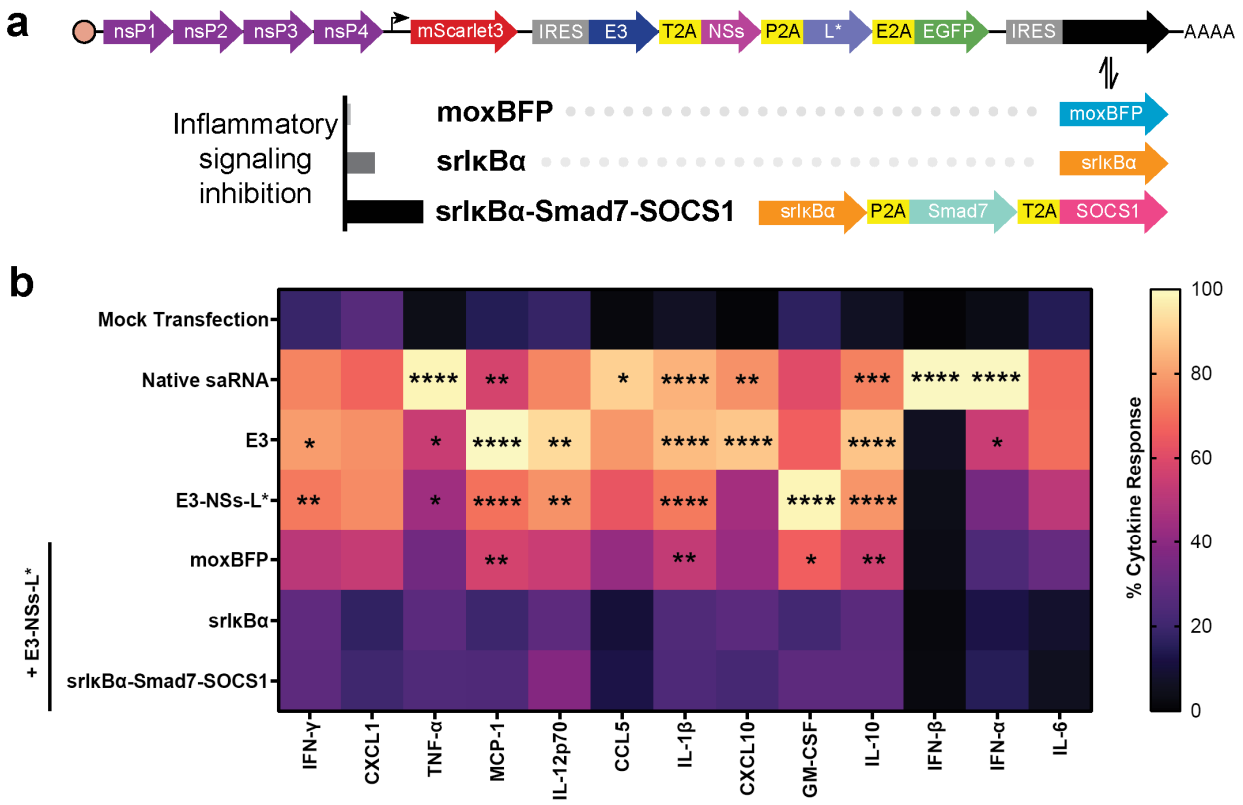

Fig. 4. Inhibiting inflammatory signaling reduces saRNA-induced anti-viral cytokine secretion

a, Schematic of the moxBFP, srIκBα, and srIκBα-Smad7-SOCS1 saRNA constructs designed for inhibition of inflammatory signaling. These constructs include dsRNA-sensing pathway inhibitors (vaccinia virus E3, Toscana virus NSs, and Theiler's virus L*). The moxBFP construct, serving as a control, lacks inflammatory signaling inhibitors. The srIκBα construct co-expresses srIκBα, which blocks the NF-κB inflammatory signaling pathway and represents moderate inflammatory signaling inhibition. The srIκBα-Smad7-SOCS1 construct co-expresses srIκBα, Smad7 and SOCS1 to additionally inhibit TGF-β and IFN pathways, representing strong inflammatory signaling inhibition. The angled arrow denotes the subgenomic promotor.
b, FLS were transfected with saRNA constructs, and anti-viral cytokines were quantified by bead-based immunoassay on day 2 post-transfection (n = 6). dsRNA-sensing pathway inhibition and inflammatory signaling inhibition significantly reduced cytokine secretion induced by saRNA. Cytokine levels were scaled within each biological replicate, with the highest value set to 100%, and the mean value displayed in the heatmap. Detailed graphs of individual cytokines are shown in Supplementary Fig. S4. For statistical analysis, cytokine levels were normalized to pre-transfection cell number (measured using BioTracker). Statistical significance for each cytokine was assessed using one-way RM ANOVA followed by Bonferroni's multiple comparisons test against the mock transfection control. A Bonferroni correction was applied to P values to account for multiple independent hypothesis testing. *$P < 0.05$, **$P < 0.01$, ***$P < 0.001$ and ****$P < 0.0001$.

Acronyms: nsP, Venezuelan equine encephalitis virus non-structural protein; IRES, encephalomyocarditis virus internal ribosome entry site; moxBFP, monomeric oxidizing environment-optimized blue fluorescent protein; E3, Vaccinia virus E3 protein; NSs, Toscana virus non-structural NSs protein; L*, Theiler's murine encephalomyelitis virus L* protein; T2A, Thosea asigna virus 2A peptide; P2A, porcine teschovirus-1 2A peptide, E2A, equine rhinitis A virus 2A peptide, srIκBα, super-repressor inhibitor of κBα; smad7, mothers against decapentaplegic homolog 7; SOCS1, suppressor of cytokine signaling 1; IFN-γ, interferon-γ; CXCL1, C-X-C motif chemokine ligand 1; TNF-α, tumor necrosis factor-α; MCP-1, monocyte chemoattractant protein-1; IL-12p70, interleukin-12; CCL5, chemokine ligand 5; IL-1β, interleukin-1β;

382 CXCL10, C-X-C motif chemokine ligand 10; GM-CSF, granulocyte-macrophage colony-stimulating factor;
383 IL-10, interleukin-10; IFN-β, interferon-β; IFN-α, interferon-α; IL-6, interleukin-6.

384 ***srIκBα* reduces cell number, whereas *srIκBα-Smad7-SOCS1* preserves cell number and enhances**
385 ***transgene expression***

386 We then examined the impact of inhibiting inflammatory signaling on cell number and transgene
387 expression (Figs. 5a, 5b). Interestingly, the srIκBα construct caused both immediate and sustained
388 reductions in cell number, as quantified by BioTracker signal, whereas the srIκBα-Smad7-SOCS1
389 construct maintained cell number comparable to mock transfection throughout the experiment (Fig. 5c).
390 AUC analysis of the BioTracker data confirmed that srIκBα-Smad7-SOCS1 significantly mitigated the
391 srIκBα-induced reduction in integrated BioTracker signal (Fig. S5a). Additional experiments using CellTag
392 and calcein AM staining corroborated these findings, showing that srIκBα negatively impacted both cell
393 number (Fig. S5b) and viability (Fig. S5c), effects that were prevented by co-expression of Smad7 and
394 SOCS1.

395 All three constructs produced low levels of EGFP expression (Fig. 5d), which was expected given EGFP's
396 position as the fourth protein in a quad-cistronic 2A element (Fig. 4a). Previous studies have
397 demonstrated that protein expression decreases significantly for downstream genes in such
398 configurations.[42] Notably, while the moxBFP and srIκBα constructs generated intermediate mScarlet3
399 levels, the srIκBα-Smad7-SOCS1 construct produced 2- to 5-fold higher mScarlet3 fluorescence
400 compared to the others (Fig. 5e).

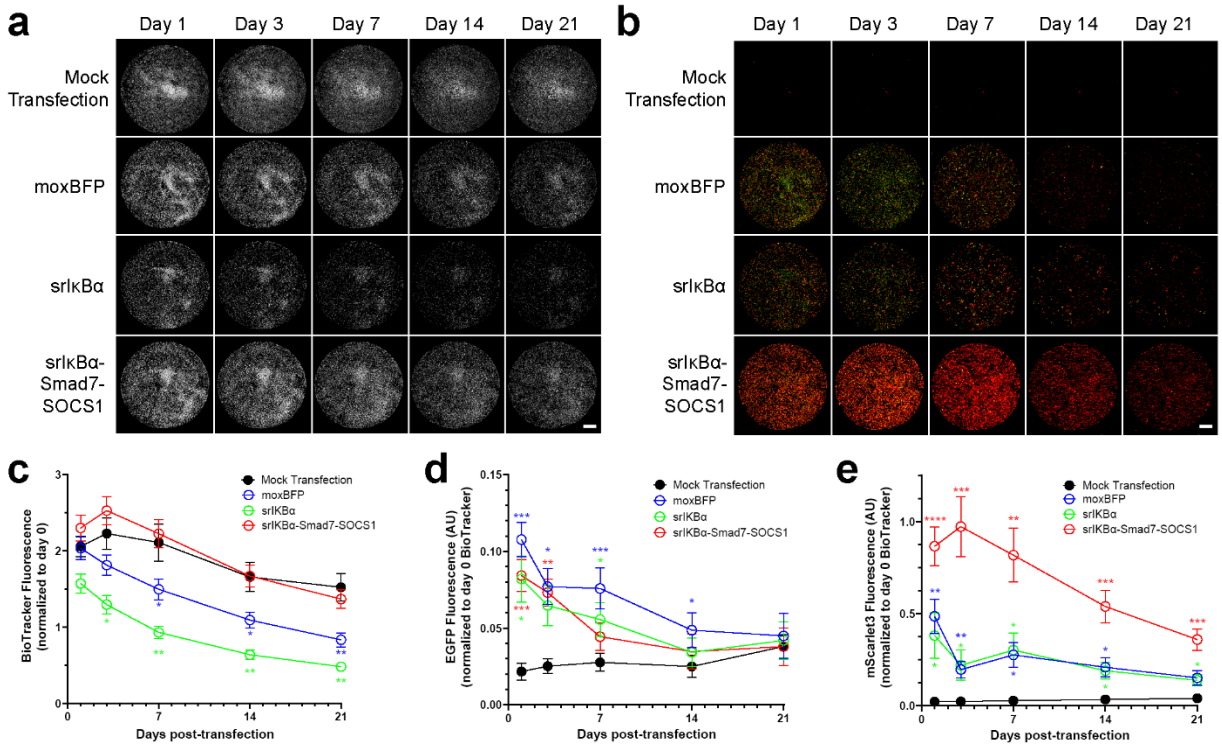

401

402 **Fig. 5. Differential effects of srIκBα and srIκBα-Smad7-SOCS1 on cell number and transgene**
403 **expression.**

404 **a**, Representative images of BioTracker staining over 3 weeks in FLS transfected with different saRNA
405 constructs. Scale bar = 5 mm.
406 **b**, Representative images of EGFP (green) and mScarlet3 (red) expression over 3 weeks in FLS
407 transfected with different saRNA constructs. Scale bar = 5 mm.
408 **c**, Quantification of BioTracker fluorescence intensity over time (n = 11). srIκBα induces reduction in cell
409 number, which is prevented by srIκBα-Smad7-SOCS1. Statistical significance of treatment effects at each

time point compared to mock transfection was determined by two-way RM ANOVA with Greenhouse–Geisser correction and Dunnett's multiple comparisons test.
d, Quantification of EGFP fluorescence intensity over time (n = 11). All constructs showed low levels of EGFP expression. Statistical significance of treatment effects at each time point compared to mock transfection was determined by two-way RM ANOVA with Greenhouse–Geisser correction and Dunnett's multiple comparisons test.
e, Quantification of mScarlet3 fluorescence intensity over time (n = 11). The srIκBα-Smad7-SOCS1 produced 2-5 times more mScarlet3 fluorescence than either moxBFP or srIκBα constructs. Statistical significance of treatment effects at each time point compared to mock transfection was determined by two-way RM ANOVA with Greenhouse–Geisser correction and Dunnett's multiple comparisons test. saRNA constructs used are shown in Fig. 4a. For all statistical reporting, *P < 0.05, **P < 0.01, ***P < 0.001 and ****P < 0.0001. Data were normalized to cell number (BioTracker intensity) on day 0, prior to transfection. The mock transfection control data used in this figure is also presented in Fig. 1. Data are presented as mean ± SEM.

Smad7 and SOCS1 co-expression prevents srIκBα-induced alterations in translational control

We next explored how srIκBα and srIκBα-Smad7-SOCS1 modulate translational regulation. Interestingly, srIκBα expression led to reductions in eIF2α phosphorylation, a change that was prevented by co-expression of Smad7 and SOCS1 (Fig. 6a). While neither construct affected total eIF2α levels or eIF4E phosphorylation compared to the moxBFP construct (Figs. 6b, 6c), srIκBα caused a significant reduction in total eIF4E levels (Fig. 6d). Given the critical role of eIF4E in cap-dependent translation, its depletion likely contributes to the poor transgene expression observed with srIκBα (Fig. 5e). These effects, combined with srIκBα-induced declines in cell number and viability (Figs. 5c, S5a-c), highlight the dual impact of srIκBα on translational machinery and cellular health. Importantly, Smad7 and SOCS1 co-expression preserved eIF4E levels, counteracting the disruption of cap-dependent translation caused by srIκBα.

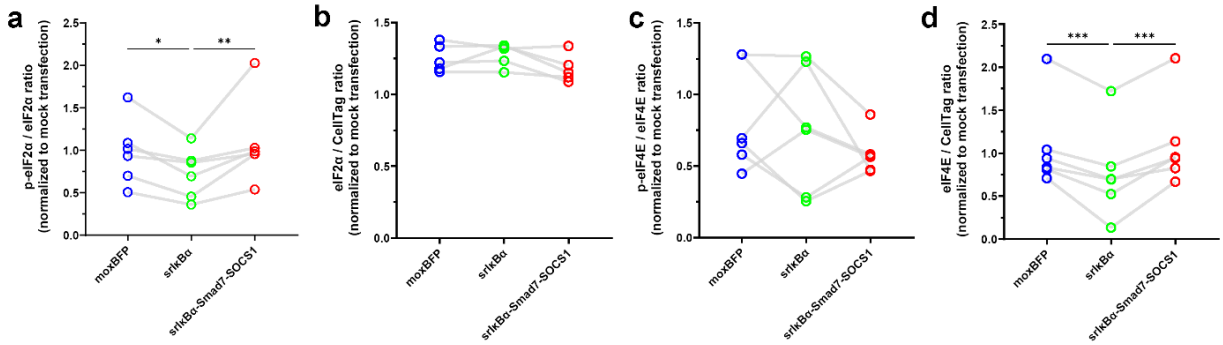

Fig. 6. *srIκBα reduces eIF2α phosphorylation and total eIF4E levels, effects reversed by co-expression of Smad7 and SOCS1*

In-cell western assays were performed 2 days post-transfection. Data are presented as fold change relative to mock-transfected cells.
a, Phosphorylation of eIF2α is significantly reduced by srIκBα, and this reduction is reversed by co-expression of Smad7 and SOCS1 (n = 6). Statistical significance was determined by one-way RM ANOVA and Holm-Šídák's multiple comparisons test to compare all groups.
b, Total eIF2α levels are not significantly affected by srIκBα or srIκBα-Smad7-SOCS1 (n = 6). One-way RM ANOVA revealed no significant differences among groups. $F(2,8)=3.683$, $P=0.0735$.
c, Phosphorylation of eIF4E is not significantly affected by srIκBα or srIκBα-Smad7-SOCS1 (n = 6). One way RM ANOVA revealed no significant difference among groups. $F(2,10)=1.336$, $P=0.3059$.
d, Total eIF4E levels are significantly reduced by srIκBα, an effect reversed by co-expression of Smad7 and SOCS1 (n = 6). Statistical significance was determined by one-way RM ANOVA and Holm-Šídák's multiple comparisons test to compare all groups.
saRNA constructs are described in Fig. 4a. For all statistical reporting, *P < 0.05, **P < 0.01 and ***P < 0.001. Mock transfection data used for normalization are the same as in Fig. 3.

452 ***Prolonged moxBFP transfection does not activate FLS, while srIκBα reduces basal activation***

453 Fibroblast activation protein-α (FAP-α) is a serine protease expressed on the surface of FLS that
454 contributes to extracellular matrix degradation and tissue remodeling.[65,66] Its expression is minimal in
455 normal adult FLS but increases significantly following inflammatory activation, such as in rheumatoid and
456 osteoarthritis.[67,68] Since viral infections can induce fibroblast activation,[69,70] we hypothesized that
457 prolonged saRNA transfection might similarly trigger FLS activation. To test this, we measured FAP-α
458 levels using an in-cell western assay after 11 days of transfection. FLS transfected with moxBFP showed
459 FAP-α levels comparable to those of mock-transfected cells, whereas srIκBα and srIκBα-Smad7-SOCS1
460 constructs resulted in significantly lower FAP-α levels compared to mock transfection (Figs. 7a, 7b).
461 These findings indicate that long-term saRNA transfection does not induce FLS activation, as measured
462 by FAP-α levels, potentially alleviating concerns that saRNA might drive pathological fibroblast
463 responses.

464

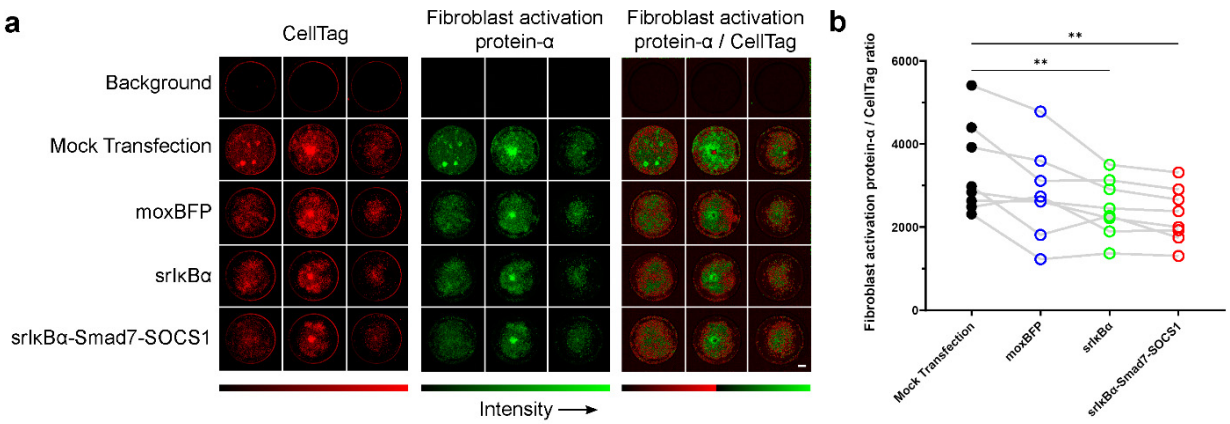

465

466 **Fig. 7. Prolonged transfection with *srIκBα or srIκBα-Smad7-SOCS1* significantly reduces basal**
467 ***fibroblast activation factor-α (FAP-α) levels***

468 **a,** Representative in-cell western images showing FAP-α expression. Columns show different biological
469 replicates, and rows show different treatments. The montage on the right shows FAP-α signal normalized
470 to CellTag signal (FAP-α/CellTag).
471 **b,** In-cell western assay of FAP-α expression (n = 8). Both srIκBα and srIκBα-Smad7-SOCS1 significantly
472 reduce FAP-α levels compared to mock transfection, while moxBFP does not differ significantly from
473 mock. Statistical significance was determined by one-way RM ANOVA with Greenhouse–Geisser
474 correction and Dunnett's multiple comparisons test to compare groups to mock transfection. **P<0.01.

475 ***Reversibility of srIκBα-Smad7-SOCS1 transfection using a small-molecule antiviral***

476 The srIκBα-Smad7-SOCS1 construct, which includes E3-NSs-L*, provides broad suppression of dsRNA
477 sensing and inflammatory signaling pathways. This construct mitigates saRNA-induced cytokine release
478 (Figs. 4b, S4a-m) and counters saRNA- and srIκBα-induced reductions in cell viability (Figs. 5c, S5a–c),
479 enabling sustained cap-dependent transgene expression (Fig. 5e) without inducing fibroblast activation
480 (Fig. 7b) or causing srIκBα-associated reductions in eIF4E levels (Fig. 6d). Together, these attributes
481 position the srIκBα-Smad7-SOCS1 construct as a promising candidate for transient gene therapy
482 applications.
483 To further enhance the therapeutic potential of this construct, we investigated whether its transfection
484 could be reversed. Achieving temporal control of transgene expression would enhance safety and
485 flexibility in therapeutic contexts. The saRNA constructs in this study rely on the VEEV RdRp for self-
486 amplification. VEEV is a mosquito-borne alphavirus capable of causing flu-like illness in humans, with the
487 potential to progress to fatal encephalitis.[71] Due to its pathogenicity, significant efforts have focused on
488 developing small-molecule inhibitors of VEEV. One such compound is ML336, a potent inhibitor of the
489 VEEV RdRp.[72]

To test whether ML336 could reverse srIκBα-Smad7-SOCS1 transfection, ML336 or vehicle was added to the culture medium one day post-transfection. EGFP and mScarlet3 fluorescence were monitored over 13 days (Fig. 8a), followed by calcein AM staining to assess cell viability (Fig. 8b). ML336 treatment significantly reduced EGFP and mScarlet3 expression over time (Figs. 8c, 8d), demonstrating its efficacy in reversing saRNA transfection. While vehicle-treated cultures exhibited lower viability compared to mock-transfected cells—possibly due to reduced proliferation over the experiment's duration—prolonged ML336 treatment did not reduce viability relative to mock-transfected controls (Fig. 8e).

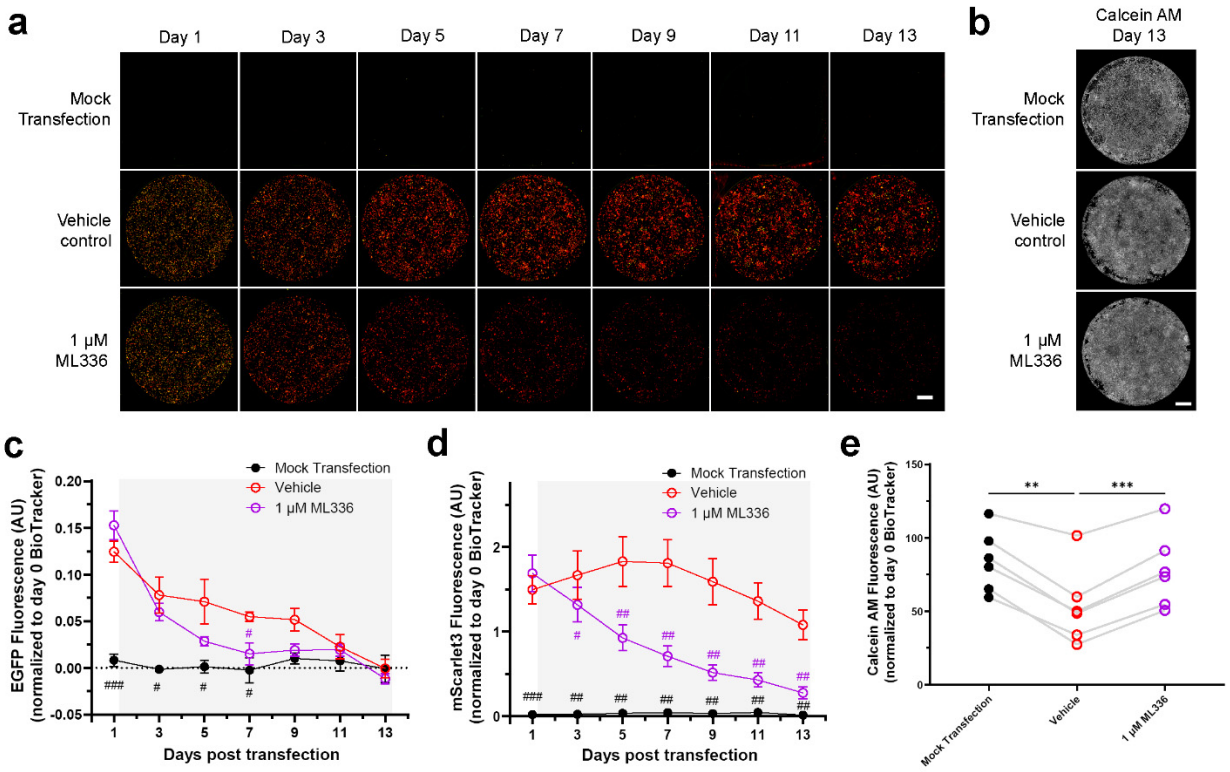

Fig. 8. ML336 reverses srIκBα-Smad7-SOCS1 saRNA transfection

a, Representative images of EGFP (green) and mScarlet3 (red) expression over 13 days in FLS transfected with srIκBα-smad7-SOCS1. Cultures were treated with vehicle or 1 μM ML336, starting 1 day post-transfection. Scale bar = 5 mm.
b, Representative images of calcein AM staining on day 13 post-transfection. Scale bar = 5 mm.
c, Quantification of EGFP fluorescence intensity in srIκBα-Smad7-SOCS1-transfected FLS (n = 6). Cultures were treated with vehicle or 1 μM ML336 (treatment period indicated by shading). EGFP fluorescence was significantly lower in ML336-treated cultures compared to vehicle-treated cultures on day 7. Statistical significance relative to vehicle-treated cells was determined by two-way RM ANOVA with Greenhouse–Geisser correction and Dunnett's multiple comparisons test. #P<0.05, ###P<0.01.
d, Quantification of mScarlet3 fluorescence intensity in srIκBα-Smad7-SOCS1-transfected FLS (n = 6). Cultures were treated with vehicle or 1 μM ML336 (treatment period indicated by shading). mScarlet3 fluorescence was significantly lower in ML336-treated cultures compared to vehicle-treated cultures beginning on day 3. Statistical significance relative to vehicle-treated cells was determined by two-way RM ANOVA with Greenhouse–Geisser correction and Dunnett's multiple comparisons test. #P<0.05, ##P<0.01, ###P<0.001.
e, Quantification of calcein AM staining on day 13 post-transfection, following 12 days of vehicle or ML336 treatment (n = 6). Cultures treated with ML336 showed no significant difference in calcein AM signal compared to mock transfection, while vehicle-treated cultures exhibited significantly lower calcein AM signals compared to both mock-transfected and ML336-treated cultures. Statistical significance was

determined by one-way RM ANOVA with Greenhouse–Geisser correction and Tukey's multiple comparisons test. **P<0.01, ***P<0.001.
Data were normalized to BioTracker intensity on day 0 and are presented as mean ± SEM.

DISCUSSION

saRNA-induced translation shutdown is thought to be mediated by phosphorylation of eIF2α.[20,26,73] During saRNA replication, dsRNA replicative intermediates activate PKR, leading to eIF2α phosphorylation and translation inhibition.[7,26] Our study is consistent with this mechanism and additionally demonstrates that saRNA induces a reduction in eIF4E phosphorylation, a phenomenon previously observed with alphavirus replicons, although the underlying mechanism remains unclear.[74,75] Similar to eIF2α phosphorylation,[76] a reduction in eIF4E phosphorylation decreases global cap-dependent translation initiation,[77] promoting cap-independent translation.[78] These combined effects—phosphorylation of eIF2α and reduced phosphorylation of eIF4E—may explain why IRES-driven, cap-independent transgenes often achieve higher expression compared to those relying on cap-dependent expression when using native saRNA.[21,79]

To counteract saRNA-induced translation shutdown, we designed saRNA constructs that express inhibitors targeting dsRNA-sensing pathways using IRES-mediated translation. During translation shutdown, global mRNA translation decreases, freeing ribosomes that would otherwise be used for translating capped mRNAs, thereby enhancing cap-independent translation.[80] By leveraging this mechanism, IRES-mediated expression of dsRNA-sensing pathway inhibitors ensures their levels increase as translation shutdown intensifies. This approach effectively inhibits dsRNA sensing and alleviates translation shutdown. In contrast, encoding these inhibitors via cap-dependent translation is expected to be less effective, as translation shutdown would lead to reduced inhibitor expression.

In this study, we used vaccinia virus E3 to prevent saRNA-induced translation shutdown, a role that E3 has previously been used to fulfill.[26,27] E3 achieves this by sequestering dsRNA intermediates from sensors like PKR[81] and by directly inhibiting PKR activation.[82] These dual actions prevent eIF2α phosphorylation, alleviating translation inhibition and enhancing transgene expression.[26,27] However, our findings suggest that this mechanism is incomplete. While E3 prevents saRNA-induced eIF2α phosphorylation, its ability to enhance transgene expression also depends on RNase L activity. By alleviating translation inhibition, E3 facilitates unrestrained RdRp production, driving robust saRNA replication and dsRNA synthesis. This dsRNA activates RNase L, which degrades mRNA[51] and inhibits nuclear mRNA export.[52] The resulting depletion of cytoplasmic mRNA[53] reduces competition for ribosomes, enabling enhanced translation of saRNA transcripts. These transcripts are shielded from RNase L degradation due to their localization within plasma membrane-associated micro-compartments called spherules.[3] Consistent with this model, inhibiting RNase L with L* in the E3-NSs-L* construct reduced transgene expression, likely due to restored ribosomal competition from intact host mRNA.

While preventing eIF2α phosphorylation and activating RNase L drive high levels of saRNA transgene expression, this combination also causes significant cytotoxicity with the E3 construct. This dual-edged effect potentially makes the E3 construct suited for immunotherapy applications, such as vaccines and cancer treatments, where robust transgene expression and immunogenic cell death can promote strong immune responses.[83,84] In contrast, non-immunotherapy applications require strategies that prioritize cell viability and minimize tissue damage over maximizing transgene expression.

Alphavirus vectors, including the VEEV replicon used in this study, are known to induce cytotoxicity in mammalian cells.[6,10,12–16] This cytotoxicity arises from dsRNA intermediates, which activate sensors such as PKR, RIG-I, MDA-5, and OAS,[5,7,26,85] despite partial shielding within spherules.[3,20] Studies in HeLa cells using microinjected dsRNA show that PKR is essential for cytosolic dsRNA-induced apoptosis, while RIG-I and MDA-5 are dispensable.[86] Numerous studies further underscore the central role of PKR in mediating apoptosis in response to dsRNA,[87–89] and have shown that PKR can mediate dsRNA-induced apoptosis even in the absence of eIF2α phosphorylation.[90] OAS also contributes to dsRNA-induced apoptosis by producing 2'-5'-oligoadenylates upon binding dsRNA, which activate RNase L, leading to cleavage of single-stranded RNA.[53] This disrupts cellular translation as cleavage of actively translated mRNA causes ribosome stalling. Ribosomes encountering truncated 3' ends of mRNAs are unable to dissociate, resulting in collisions,[91,92] triggering the ribotoxic stress response[93] which can lead to

apoptosis.[91,94] These findings from the literature identify PKR and OAS/RNase L as key contributors to saRNA-associated cytotoxicity and highlight them as valuable targets for mitigation.

While E3 relieves saRNA-induced eIF2α phosphorylation,[26,27] the E3 construct also compromised RNA integrity, suggesting activation of the OAS/RNase L pathway. Furthermore, PKR, an IFN-inducible gene,[95] was upregulated by the E3 construct, potentially allowing partial evasion of E3-mediated inhibition. Thus, vaccinia virus E3 alone did not fully address the cytotoxic actions of dsRNA replicative intermediates produced during saRNA replication. To further suppress PKR and OAS/RNase L pathways, we used Toscana virus NSs[40] and Theiler's virus L*,[41] respectively. While this strategy resulted in lower transgene expression—likely due to the protective actions of RNase L inhibition on cellular mRNA integrity—it effectively mitigated the intrinsic mechanisms of saRNA cytotoxicity. However, the inclusion of multiple viral proteins introduces additional challenges. In vivo, saRNA constructs must contend not only with intrinsic cytotoxic mechanisms but also with adaptive immune responses leading to extrinsic cytotoxicity. The co-expression of several viral proteins, along with the VEEV RdRp, significantly increases the likelihood of viral peptides being presented on major histocompatibility complex class I molecules to cytotoxic T lymphocytes. This is expected to activate adaptive immune responses, which could culminate in the elimination of saRNA-transfected cells. Addressing both intrinsic and immune cell-mediated cytotoxicity will be critical to achieving the long-term viability of saRNA-transfected cells and unlocking the platform's full therapeutic potential.

While we found that inhibiting dsRNA-sensing pathways was an effective means to reduce saRNA-induced cytotoxicity, it was not effective at preventing saRNA-induced cytokine responses. This agrees with prior reports showing that dsRNA activates NF-κB even in the absence of PKR and RNase L,[96] suggesting additional mechanisms contribute to NF-κB activation. One such mechanism may involve eIF4E, a key regulator of translation initiation, whose activity is governed by its phosphorylation status and serves as a rate-limiting step in cap-dependent protein synthesis.[50] In this study, we found that saRNA transfection induces a reduction in eIF4E phosphorylation. Reduced eIF4E phosphorylation has been shown to decrease the levels of the short-lived IκBα protein,[97] an inhibitor of NF-κB that sequesters it in the cytoplasm and prevents nuclear translocation. Decreased IκBα levels thus allow NF-κB to translocate to the nucleus, initiating cytokine expression and inflammatory responses. To address this, we expressed srIκBα using cap-independent translation to produce a stable cytoplasmic pool of IκBα, thereby preventing NF-κB activity. While this strategy effectively reduced saRNA-induced cytokine responses, it also resulted in a reduction in cell viability, highlighting a tradeoff between suppressing inflammation and maintaining cell survival.

The NF-κB pathway is a key regulator of inflammatory cytokine production, making it an important target for suppressing cytokine responses.[98] However, NF-κB also has pro-survival functions as it promotes the transcription of anti-apoptotic genes—though its exact effects depend on tissue type and biological context.[99] In FLS, overexpression of srIκBα reduces inflammatory cytokine production but increases sensitivity to TNF-α-induced apoptosis,[100,101] consistent with our findings that saRNA encoding srIκBα lowered both anti-viral cytokine responses and cell viability. This phenomenon is not unique to FLS; inhibition of NF-κB signaling with srIκBα has also been shown to render liver hepatocytes more susceptible to pro-apoptotic stimuli.[102] This raises a key safety consideration, as saRNA delivery systems such as lipid nanoparticles tend to accumulate in the liver.[103] Therefore, when designing saRNA constructs for sustained, non-immunostimulatory transgene expression in contexts where apoptosis is undesirable, the use of srIκBα to suppress cytokine responses may require co-expression of anti-apoptotic proteins to offset the loss of NF-κB-mediated survival signaling.

In this study, we show that co-expressing Smad7 and SOCS1 effectively counteracted srIκBα-induced cell death in FLS. While we did not assess the individual contributions of each protein, both are known to have anti-apoptotic properties in certain contexts. Smad7 can inhibit TGF-β-induced apoptosis,[104,105] while SOCS1 can suppress apoptosis triggered by IFN-α, IFN-β,[106] IFN-γ,[107] and TNF-α.[108–110] These anti-apoptotic effects likely enable Smad7 and SOCS1 to mitigate srIκBα-induced reductions in FLS cell viability.

We also found that co-expression of Smad7 and SOCS1 significantly enhanced cap-dependent transgene expression. Although we did not distinguish the contributions of each protein to this effect, it is likely mediated by SOCS1. Previous studies have shown that ruxolitinib, a small-molecule inhibitor of

624 Janus kinase (JAK) 1 and JAK2,[111] increases saRNA transgene expression when added to saRNA
625 polyplexes.[18] SOCS1 is an endogenous inhibitor of JAK1 and JAK2,[112] therefore, SOCS1 offers a
626 genetically encoded alternative to the small-molecule approach of ruxolitinib for enhancing saRNA
627 expression.

628 Furthermore, this study presents a straightforward method for controlling saRNA activity. ML336, a VEEV
629 RdRp inhibitor, blocks the synthesis of positive-sense genomic, negative-sense template, and
630 subgenomic RNAs of VEEV without affecting host cellular RNA transcription.[113] It has an in vitro effective
631 concentration 50 (EC_{50}) of 0.02-0.04 μM, and a 50 mg/kg dose offers 100% protection in a lethal VEEV
632 mouse infection model, with no observed toxicity.[114] Thus, ML336 and other RdRp inhibitors could provide
633 a practical means to deactivate saRNA—either to terminate transgene expression once therapeutic
634 objectives are met or as a safety measure to reduce the risks associated with prolonged innate immune
635 suppression and other potential side effects, including adaptive immune responses to the VEEV replicon
636 or viral innate immune inhibitory proteins.

637 Preclinical and clinical data show that saRNA vaccines often trigger an intense innate immune response
638 that can hinder antigen expression.[8,18,26] Additionally, saRNA vaccines can induce significant
639 inflammation,[115,116] which is increasingly recognized as problematic, as common adverse events include
640 pain, headache, tenderness, arthralgia, fever, and chills.[117,118] The approaches described in this study,
641 which reduces the inherent immunostimulatory effects of saRNA replication, could potentially be applied
642 to future saRNA vaccine designs to improve antigen expression and reduce reactogenicity.

643 The approach in this study also underscores the versatility of the saRNA platform, which can efficiently
644 integrate multiple transgenes and genetic elements. Our largest construct included the VEEV RdRP, two
645 IRES sequences, five 2A peptides, and eight transgenes within a 16.5-kilobase saRNA. This ability to
646 encode numerous transgenes without apparent size constraints is a notable yet underutilized strength of
647 the saRNA platform.

648 Leveraging this capacity for multiple transgenes, we encoded diverse inhibitors of dsRNA-sensing and
649 inflammatory signaling pathways directly within saRNA achieving durable and reversible transgene
650 expression with minimal cytotoxicity and immunostimulation. This approach eliminates the need for
651 exogenous immune suppressants, a common requirement in other studies utilizing saRNA for non-
652 immunotherapy applications. For instance, therapeutic antibody production, cellular reprogramming, and
653 retinal cell transfection with saRNA have relied on interferon-α/β receptor-1 blocking antibodies or the
654 vaccinia virus B18R interferon decoy receptor to suppress innate immune responses and achieve
655 effective transgene expression.[9,21–23] Similarly, corticosteroids have been used to enhance antigen
656 expression by reducing saRNA-induced innate immune activation.[25] Here, we demonstrate that encoding
657 broad-spectrum innate immune suppression directly within the saRNA obviates the need for additional
658 immune-modulatory treatments, thereby reducing treatment complexity. Moreover, this strategy localizes
659 immune suppression to transfected cells, which should minimize the risks of off-target effects associated
660 with systemic immune suppression.

661 Expressing multiple transgenes may also be a useful strategy for developing novel therapeutics. The NF-
662 κB, TGF-β, and JAK/signal transducer and activator of transcription (STAT) pathways are central to the
663 progression of osteoarthritis.[119–121] The srIκBα-Smad7-SOCS1 saRNA construct provides a novel strategy
664 to simultaneously target these pathways: srIκBα inhibits NF-κB, Smad7 blocks TGF-β, and SOCS1
665 suppresses the JAK/STAT pathway. Each of these proteins has been independently studied as a
666 treatment for osteoarthritis,[122–124] and their combination within a single construct could represent a
667 synergistic strategy to enhance therapeutic efficacy. While arthritogenic alphaviruses such as
668 chikungunya virus and Ross river virus can drive inflammatory responses in FLS, including upregulation
669 of secreted proteolytic molecules such as matrix metalloproteases,[125,126] the lack of FAP-α upregulation in
670 transfected FLS provides some evidence that saRNA transfection does not trigger comparable
671 responses. Moreover, the reduction in basal FAP-α levels observed with the srIκBα and srIκBα-Smad7-
672 SOCS1 constructs raises the possibility that saRNA could serve as a tool for suppressing fibroblast
673 activation in inflammatory settings. This approach could hold therapeutic potential in arthritis treatment,[127]
674 warranting further investigation in disease models.

675 In addition to expressing therapeutic transgenes, saRNA holds potential for inducing therapeutic effects
676 by modulating translational control. While the strategy outlined in this report mitigated eIF2α

677 phosphorylation, it was not effective at preventing saRNA-induced reductions in eIF4E phosphorylation.
678 In vitro directed evolution of the RdRp replicon[6,28,128] may offer a potential solution to this challenge.
679 Furthermore, we found that srIκBα expression decreased eIF4E levels, consistent with previous
680 findings.[129] While reducing eIF4E activity through saRNA or srIκBα expression could lower transgene
681 expression, it may also have therapeutic value, as lower eIF4E activity is associated with decreased pain
682 sensitivity,[130] inhibition of tumorigenesis[131], improvement of neurodevelopmental social deficits[132], and
683 increased longevity.[133] We also observed that srIκBα expression reduced phosphorylation of eIF2α, while
684 the E3-NSs-L* construct reduced PKR levels. Given that eIF2α phosphorylation activates the integrated
685 stress response, a pathway often driven by PKR in age-related diseases like neurodegeneration,[134]
686 saRNA may represent a novel approach to modulate stress responses in these conditions.

687 Our findings introduce a novel, fully saRNA-based strategy to overcome a key limitation of saRNA:
688 continuous innate immune stimulation. By inhibiting multiple innate immune pathways through proteins
689 expressed via cap-independent translation, we achieve sustained transgene expression with low
690 cytotoxicity and minimal antiviral cytokine induction, all without the use of exogenous
691 immunosuppressants. Building on these in vitro results, the next step will be to evaluate this strategy in
692 vivo to assess its effectiveness in complex biological environments. If successful, this approach could
693 expand the therapeutic applications of saRNA to non-immunotherapy contexts, such as protein
694 replacement therapy, therapeutic antibody production, genome editing, cellular reprogramming, and
695 immune cell engineering, where prolonged innate immune stimulation is undesirable. Importantly, the
696 reversibility of this approach offers significant advantages, enabling precise control over transgene
697 expression and serving as a crucial safety mechanism for future clinical applications.

698

699 MATERIALS & METHODS

700 *Experimental Design*

701 This study aimed to develop and evaluate saRNA constructs that modulate innate immune responses,
702 specifically targeting dsRNA sensing and inflammatory signaling pathways, to reduce saRNA-induced
703 cytotoxicity, cytokine expression, and achieve sustained transgene expression. To this end, we
704 engineered saRNA constructs that co-express multiple viral innate immune inhibitors and cellular
705 inhibitors of inflammatory signaling. The constructs were designed to enable monitoring of cap-dependent
706 and cap-independent translation using distinct fluorescent proteins.

707 The experimental approach included cloning the saRNA constructs using molecular biology techniques,
708 followed by in vitro transcription and transfection into mouse primary FLS. Transfected cells were
709 analyzed using fluorescence-based microplate assays to assess cell number, cell viability,
710 phosphatidylserine exposure, and fluorescent protein expression. Further evaluations of translational
711 control, FLS activation markers, RNA integrity, and cytokine secretion were conducted using in-cell
712 western assays, capillary electrophoresis, and bead-based immunoassays. Finally, the reversibility of
713 saRNA transfection was explored using a small-molecule inhibitor targeting the VEEV RdRp.

714 *Plasmid cloning and construct design*

715 The commercially available TagGFP2 E3L Simplicon vector (SCR725, Merck) served as the saRNA
716 backbone in this study. After removing the TagGFP2-IRES-E3 sequence, various constructs were
717 generated by combining different elements using restriction digests (FastDigest, Thermo Scientific),
718 overlap extension PCR (Phusion, Thermo Scientific), and HiFi assembly (NEBuilder, New England
719 Biolabs).

720 Genetic elements were sourced as follows: mScarlet3 from pDx_mScarlet3 (a gift from Dorus Gadella
721 [Addgene plasmid #189754]),[135] IRES-EGFP from pIRES2-EGFP (Clontech), and IRES-E3 and IRES-
722 PuroR (puromycin resistance) from the original TagGFP2 E3L Simplicon vector.

723 Custom gene synthesis (GeneArt, Thermo Scientific) was used to produce IRES-moxBFP, IRES-E3-T2A-
724 NSs-P2A-L*-E2A-mEGFP, and IRES-srIκBα-P2A-Smad7-T2A-SOCS1 sequences. The IRES sequence

725 was derived from pIRES2-EGFP (Clontech). Other sequences were derived from public databases:
726 moxBFP (FPbase ID: SSTDU),[136] mEGFP (FPbase ID: QKFJN), E3 (UniProt: P21605-1), NSs (UniProt:
727 P21699), L* (UniProt: P0DJX4), Smad7 (UniProt: O35253-1), and SOCS1 (UniProt: O35716). srIκBα was
728 engineered from IκBα (UniProt: Q9Z1E3) by substituting serines 32 and 36 with alanines. All synthesized
729 sequences were codon-optimized for mouse expression (GenSmart, GenScript).

730 Plasmids were cloned in DH5α competent *Escherichia coli* (High Efficiency, New England Biolabs) and
731 purified by maxiprep (PureLink HiPure, Invitrogen). All plasmid sequences were verified using nanopore
732 whole plasmid sequencing (Plasmidsaurus).

733 ***RNA synthesis***

734 Plasmids were linearized using XbaI (FastDigest, Thermo Scientific) at 37°C for 3 hours. The linear
735 plasmids were purified by phenol-chloroform extraction followed by sodium acetate ethanol precipitation.
736 Uncapped RNA was synthesized *in vitro* using the T7 RiboMAX Large Scale RNA Production kit
737 (Promega) at 37°C for 2 hours. After purification by ammonium acetate precipitation, the RNA was
738 denatured at 65°C for 5 minutes. Cap-1 structures were then generated using the Vaccinia Capping
739 System in conjunction with mRNA cap 2'-O-methyltransferase (both from New England Biolabs) for 45
740 minutes at 37°C. Following another ammonium acetate purification, the RNA was treated with Antarctic
741 phosphatase (New England Biolabs) for 30 minutes at 37°C. After a final ammonium acetate purification
742 step, the RNA was resuspended in THE RNA Storage Solution (Invitrogen), aliquoted, and stored at -
743 80°C until use.

744 ***Animals***

745 All mice used in this study were 5- to 12-week-old wildtype C57BL/6J mice (Bicester, UK). Both male and
746 female mice were included, though sex differences in response to saRNA transfection were not analyzed.
747 Mice were housed in groups of up to five in a temperature-controlled room (21°C), with bedding, a red
748 shelter, and enrichment materials provided. They were maintained on a 12-hour light/dark cycle, with food
749 and water available ad libitum. Mice were euthanized by exposure to CO_2 gas in a rising concentration,
750 and death confirmed by dislocation of the atlanto-occipital joint by applying pressure to the side of the
751 neck using thumb and forefinger, procedures in line with the Animals (Scientific Procedures) Act 1986
752 Amendment Regulations 2012.

753 ***Mouse primary FLS culture***

754 We cultured FLS from mouse knee joints following established protocols,[137] with slight modifications. In
755 brief, knee joints were exposed by cutting through the overlying skin with dissecting scissors. The patellar
756 tendon was then grasped near the patella with Dumont tweezers, and spring scissors were used to sever
757 the patellar tendon along with surrounding tissues. Finally, the patella was excised by cutting the
758 quadriceps tendon, and excess muscle and tendons were carefully trimmed away.

759 Both patellae from each animal were collected into a microcentrifuge tube containing ice-cold sterile
760 phosphate buffered saline (PBS), then transferred to a 24-well tissue culture plate (Costar) with FLS
761 culture media. The media consisted of DMEM/F-12 (Invitrogen) supplemented with 25% fetal bovine
762 serum (Sigma), 1X GlutaMAX (Gibco), and 100 µg/ml Primocin (InvivoGen).

763 The patellae were maintained in a humidified incubator at 37°C with 5% CO2, with media changes every
764 1-2 days. FLS outgrowth was observed, and after approximately 10 days, when cells reached 70%
765 confluency, the patellae were transferred to new wells for further FLS collection. Cells attached to the
766 original wells were passaged using 0.1% trypsin-EDTA (Sigma) into a single well of a 6-well plate
767 (Costar). Cells were later expanded into T25 flasks (BioLite, Thermo Scientific or CELLSTAR, Greiner
768 Bio-One) and passaged upon reaching confluency. After the second passage, Versene solution (Gibco)
769 was used for cell dissociation.

770 FLS were used between passages 3 and 8. In most experiments, cells from the same animal were
771 divided and plated onto 6-well or 24-well plates, allowing for parallel manipulations with matched
772 conditions. Occasionally, when cell number was low, cells from different animals were pooled before
773 division. Once plated for experiments, media was changed every 2-3 days.

774 ***Immunocytochemistry and confocal microscopy***

775 Cells were plated on poly-D-lysine-coated glass-bottom 35 mm dishes (P35GC-1.5-14-C, MatTek) and
776 fixed with 4% paraformaldehyde for 10 minutes at room temperature without permeabilization. After
777 fixation, cells were washed twice with PBS, followed by blocking with 10% normal goat serum in PBS for
778 1 hour at room temperature.

779 Cells were then incubated overnight at 4°C in blocking buffer, either without primary antibody (no primary
780 control) or with cadherin-11 (extracellular) rabbit polyclonal antibody (1:200, DF3523, Affinity
781 Biosciences). After three washes with PBS, cells were incubated for 1 hour at room temperature in
782 blocking buffer with 1 µg/ml Hoechst 33342, BioTracker NIR680 (1:2000, Merck), and goat anti-rabbit
783 Alexa Fluor 488 secondary antibody (1:500, Invitrogen).

784 After four additional PBS washes, cells were imaged in PBS using a Leica Stellaris 5 confocal microscope
785 equipped with a 40X oil immersion objective. Tile-scanned images were stitched using Las X microscopy
786 software (Leica) to generate high-resolution panoramic images.

787 ***BioTracker staining***

788 BioTracker NIR680 was diluted 1:2000 in unsupplemented DMEM/F-12. T25 flasks containing FLS were
789 washed once with HBSS (with calcium and magnesium, Gibco), then incubated with the diluted dye for 30
790 minutes at 37°C. After incubation, the flasks were washed three times with FLS media, with each wash
791 lasting 10 minutes at 37°C. The FLS were then dissociated using Versene and plated onto 6- or 24-well
792 plates.

793 ***FLS transfection***

794 For transfection in 6-well plates, the medium was removed and replaced with 1 ml of Opti-MEM I (Gibco).
795 In a microcentrifuge tube, 500 ng of saRNA was diluted in 200 µl of Opti-MEM I. In a separate tube, 3 µl
796 of Lipofectamine MessengerMAX (Invitrogen) was diluted in 100 µl of Opti-MEM I. After gently mixing, the
797 complexes were incubated at room temperature for 5 minutes, then added dropwise to the cells. The cells
798 were incubated with the complexes for 2 hours at 37°C, after which the media was removed and replaced
799 with fresh FLS media. For transfection in 24-well plates, all volumes and amounts of saRNA were
800 reduced fivefold.

801 ***Microplate imaging***

802 Unless otherwise specified, black glass-bottom 6-well plates (P06-1.5H-N, Cellvis) were used for
803 microplate imaging. Prior to imaging, the FLS media was replaced with Live Cell Imaging Solution
804 (Invitrogen). Imaging was performed using the Odyssey M laser scanner (LI-COR), using LI-COR
805 acquisition software with a plate offset of +1.45 mm and 100 µm resolution.

806 EGFP, mScarlet3, and BioTracker NIR680 were imaged using the 488, 520, and 700 channels,
807 respectively. Spectral cross-excitation between EGFP and mScarlet3 in the 488 and 520 channels was
808 corrected through linear unmixing analysis, as described below. Fluorescence intensity was quantified in
809 ImageJ by measuring the integrated density within equal-area regions of interest for each well.
810 Fluorescence values (EGFP, mScarlet3, and BioTracker) were normalized by the day 0 BioTracker signal
811 measured before transfection to account for variations in starting cell number.

812 ***Linear unmixing analysis***

813 saRNA constructs encoding individual fluorescent proteins (moxBFP, EGFP, or mScarlet3) were
814 designed to assess cross-excitation among the fluorescent proteins used in this study. tSA201 cells
815 (96121229, ECACC) were seeded in black glass-bottom 6-well plates coated with poly-D-lysine (Sigma)
816 and transfected with the saRNA constructs. Cells were imaged the following day using an Odyssey M
817 laser scanner, with fluorescence captured through the 488 and 520 channels. Expression of moxBFP was
818 undetectable in both the 488 and 520 channels, and therefore it was excluded from further analysis.
819 Bleed-through of EGFP into the 520 channel and mScarlet3 into the 488 channel was quantified using
820 ImageJ, with cross-excitation determined to be 11.32% and 0.94%, respectively. The emission signals
821 were assumed to be linearly proportional to the sum of the intensities of each fluorophore, and the
822 unmixed EGFP and mScarlet3 signals were calculated using Python.

823 ***Annexin V assay***

824 FLS were stained with BioTracker NIR680 and plated on black glass-bottom 24-well plates (Sensoplate,
825 Greiner Bio-One). Cells were transfected with saRNA or treated with 0.5 μM staurosporine (Cayman
826 Chemical) as a positive control.

827 Annexin V-CF800 conjugate (Biotium) was diluted to 250 ng/ml in Live Cell Imaging Solution (Invitrogen).
828 On each day of the assay, wells were washed with Live Cell Imaging Solution and replaced with diluted
829 Annexin V-CF800 solution. Plates were incubated at 37°C for 15 minutes. Following incubation, plates
830 were washed 3 times with Live Cell Imaging Solution before imaging the 700 and 800 channels with an
831 Odyssey M imager set to +1.45 mm image offset and 100 μm resolution.

832 Image analysis was performed using ImageJ. To correct for unidirectional spectral bleed-through of
833 BioTracker NIR680 into the 800-channel, subtractive compensation was applied by dividing the 700-
834 channel image by a factor of 800 and then subtracting it from the 800-channel image. Due to the
835 presence of a small number of high-intensity speckles in the 800-channel image, area rather than
836 fluorescence intensity was quantified. The display range of the 800-channel image was set between 0.25
837 and 2.5 and the image was thresholded using the method of Li.[138] The area of thresholded pixels within
838 each well was then quantified and adjusted based on the BioTracker signal before transfection to account
839 for variations in cell number. Data was then normalized to the average of the mock transfection condition.

840 ***Calcein AM staining***

841 Calcein AM (Invitrogen) staining was performed according to the manufacturer's protocol. Briefly, cells
842 were washed with HBSS and incubated with 2 μM calcein AM (diluted in HBSS) at 37°C for 30 minutes.
843 Following three washes, cells were imaged in Live Cell Imaging Solution, and the 488-channel image was
844 captured using an Odyssey M imager.

845 Although calcein AM and EGFP share overlapping spectra, calcein AM fluorescence was typically much
846 higher than EGFP, making EGFP's contribution to the measured Calcein AM signal negligible in most
847 cases. However, when the E3 construct was used, EGFP expression was sufficient to interfere with the
848 signal. To address this, in experiments that included use of the E3 construct, a 488-channel image was
849 captured prior to calcein AM application and subtracted from the post-application image to accurately
850 measure calcein AM fluorescence.

851 Fluorescence intensity was quantified using ImageJ. In experiments where BioTracker was used,
852 fluorescence values were corrected by the pre-transfection BioTracker signal to account for differences in
853 starting cell number.

854 ***In-cell western assay***

855 Cells were plated on black, glass-bottom 24-well plates. Alongside mock and saRNA transfections, one
856 well was reserved for background subtraction, which received no treatment. Unless specified otherwise,
857 experiments were conducted 2 days post-transfection. Cells were fixed with 4% paraformaldehyde for 10

858 minutes at room temperature, followed by two washes with tris-buffered saline (TBS). Permeabilization
859 was then performed using 0.1% Triton X-100 in TBS for 10 minutes, followed by two additional TBS
860 washes. After permeabilization, cells were blocked with Intercept TBS Blocking Buffer (LI-COR) for 1 hour
861 at room temperature with gentle agitation.

862 Primary antibodies were diluted in Intercept Blocking Buffer and incubated with the cells overnight at 4°C.
863 The background subtraction well was incubated with blocking buffer alone, without primary antibodies.
864 The following primary antibodies were used: Phospho-eIF2α (Ser51) (D9G8) XP rabbit monoclonal
865 (1:200, #3398, Cell Signaling Technology), eIF2α (L57A5) mouse monoclonal (1:200, #2103, Cell
866 Signaling Technology), PKR rabbit polyclonal (1:500, #18244-1-AP, Proteintech), Phospho-eIF4E (S209)
867 rabbit monoclonal (1:200, #ab76256, Abcam), eIF4E mouse monoclonal (5D11) (1:200, #MA1-089,
868 Invitrogen), and fibroblast activation protein (73.3) mouse monoclonal (20 µg/ml, #BE0374, InVivoMAb).
869 Except for the fibroblast activation protein antibody, which was conjugated to DyLight 800 using the
870 manufacturer's DyLight Antibody Labeling Kit (#53062, Thermo Scientific), all primary antibodies were
871 unconjugated.

872 After washing the wells three times with TBS, cells were incubated for 1 hour at room temperature with
873 the appropriate secondary antibodies or normalization stain, with gentle agitation. The secondary
874 antibodies used were goat anti-mouse IRDye 800CW (1:800), donkey anti-rabbit IRDye 800CW (1:800),
875 donkey anti-mouse IRDye 680RD (1:800), and CellTag 700 (1:500), all from LI-COR. The background
876 subtraction well received secondary antibody but no CellTag. Following four additional washes with TBS,
877 the plate was inverted and gently tapped on absorbent paper to remove excess liquid. The plate was then
878 imaged using the Odyssey M imager with LI-COR Acquisition software using a plate offset of +1.45 and
879 100 µm resolution. Signal quantification was carried out using Empiria Studio software (LI-COR).

880 ***RNA integrity analysis***

881 FLS were plated in 6-well plates and transfected with either saRNA or subjected to mock transfection.
882 After 26-30 hours, cells were harvested by scraping in 350 µl RLT buffer (QIAGEN) supplemented with 10
883 µl/ml β-mercaptoethanol (Sigma). Cell lysates were homogenized using QIAshredder columns (QIAGEN),
884 and total RNA was extracted using the RNeasy Mini Kit (QIAGEN) according to the manufacturer's
885 instructions. RNA quantity and quality were initially assessed using a N60 nanophotometer (Implen).
886 Samples were aliquoted and stored at -80°C until further analysis. For detailed quality assessment,
887 samples were transported on dry ice and analyzed using the RNA Pico Kit on the 2100 Bioanalyzer
888 system (Agilent), performed by Cambridge Genomic Services. RNA Integrity Number (RIN) values were
889 determined for each sample, and the differences in RIN between saRNA-transfected and mock-
890 transfected conditions were calculated.

891 ***Bead-based immunoassay***

892 FLS were stained with BioTracker and seeded onto 6-well plates. After transfection, the saRNA-
893 lipofectamine complexes were replaced with 2 ml of fresh FLS media. Two days later, supernatants were
894 collected and stored at -80°C until analysis. On the day of analysis, the supernatant was thawed on ice,
895 and levels of 13 innate immune-related cytokines (IFN-γ, CXCL1, TNF-α, MCP-1, IL-12p70, CCL5, IL-1β,
896 CXCL10, GM-CSF, IL-10, IFN-β, IFN-α, and IL-6) were measured using the LEGENDplex Mouse Anti-
897 Virus Response Panel (740621, BioLegend) following the manufacturer's protocol. Samples were run in
898 duplicate. A custom 3D-printed PETG vacuum manifold (designed with Fusion 360) was used for vacuum
899 filtration, and beads were analyzed using a CytoPLEX LX flow cytometer (Beckman Coulter). Data
900 analysis was performed with the LEGENDplex Qognit Data Analysis Suite (BioLegend). To account for
901 differences in cell number between wells, cytokine levels were corrected based on the BioTracker signal
902 before transfection.

903 ***ML336 experiments***

ML336 (Cayman Chemical) was dissolved in DMSO (Sigma) at a stock concentration of 10 mM, and aliquots were stored at -20°C. For treatments, ML336 was added to cell cultures at a final concentration of 1 μM, while vehicle control cultures received 0.01% DMSO.

Statistical Analysis

All statistical analyses were conducted using GraphPad Prism 9, with specific tests detailed in the corresponding figure legends. All statistical tests were two-sided tests.

DATA AVAILABILITY STATEMENT

The code for the unmixing analysis is available at https://github.com/lariferg/spectral_unmixing.

The 3D printed vacuum manifold compatible with the LEGENDplex assay has been deposited in the NIH 3D print exchange (3DPX-021388).

All data needed to evaluate the conclusions in the paper are present in the paper, the Supplementary Materials, and the Figshare repository http://doi.org/10.6084/m9.figshare.27091972.

ACKNOWLEDGMENTS

The authors gratefully acknowledge the Cambridge Advanced Imaging Centre, the flow cytometry facility from the School of the Biological Sciences, and Cambridge Genomic Services for their support & assistance in this work. The authors would like to thank Dr. Paul Miller for providing the pDx_mScarlet3 plasmid and Dr. Alex Cloake for providing the pIRES2-EGFP plasmid used in this study. T.K.L. acknowledges support from a Horizon Europe Marie Skłodowska-Curie Actions European Postdoctoral Fellowship (UKRI Guarantee) [EP/X023117/1]. A.R. and L.W.P. disclose support from AstraZeneca PhD studentships [G115018 and G113502, respectively]. L.F. discloses support from funding provided by the MRC Postdoctoral Training Scheme. E.St.J.S. acknowledges funding from the UKRI and Versus Arthritis [MR/W002426/1] as part of the ADVANTAGE visceral pain consortium through the Advanced Pain Discovery Platform (APDP) and the Wellcome Trust [225856/Z/22/Z].

AUTHOR CONTRIBUTIONS

Conceptualization, T.K.L. and E.St.J.S
Formal analysis: T.K.L., E.St.J.S.
Funding acquisition: E.St.J.S., T.K.L.
Investigation: T.K.L., A.R., L.W.P.
Methodology: T.K.L., T.A.
Resources: E.St.J.S., T.K.L.
Software: L.F.
Supervision: E.St.J.S., T.K.L.
Visualisation: T.K.L., E.St.J.S.
Writing—original draft: T.K.L.
Writing—reviewing & editing: E.St.J.S., L.F.

DECLARATION OF INTERESTS

Authors declare that they have no competing interests.

KEYWORDS

Self-amplifying RNA, alphavirus vectors, RNA replicons, fibroblast-like synoviocytes, double-stranded RNA sensors, nuclear factor kappa B, viral innate immune antagonists, RNA vaccines, RNA therapeutics

DECLARATION OF GENERATIVE AI AND AI-ASSISTED TECHNOLOGIES IN THE WRITING PROCESS

During the preparation of this work, the authors used OpenAI's ChatGPT to enhance clarity and flow of the writing. After using this tool, the authors reviewed and edited the content as needed and take full responsibility for the content of the publication.

REFERENCES

1. Frolov, I., Hoffman, T.A., Prágai, B.M., Dryga, S.A., Huang, H.V., Schlesinger, S., and Rice, C.M. (1996). Alphavirus-based expression vectors: strategies and applications. Proc Natl Acad Sci U S A *93*, 11371–11377.

2. Bloom, K., van den Berg, F., and Arbuthnot, P. (2021). Self-amplifying RNA vaccines for infectious diseases. Gene Ther *28*, 117–129. https://doi.org/10.1038/s41434-020-00204-y.

3. Pietilä, M.K., Hellström, K., and Ahola, T. (2017). Alphavirus polymerase and RNA replication. Virus Research *234*, 44–57. https://doi.org/10.1016/j.virusres.2017.01.007.

4. Maruggi, G., Zhang, C., Li, J., Ulmer, J.B., and Yu, D. (2019). mRNA as a Transformative Technology for Vaccine Development to Control Infectious Diseases. Mol Ther *27*, 757–772. https://doi.org/10.1016/j.ymthe.2019.01.020.

5. Akhrymuk, I., Frolov, I., and Frolova, E.I. (2016). Both RIG-I and MDA5 detect alphavirus replication in concentration-dependent mode. Virology *487*, 230–241. https://doi.org/10.1016/j.virol.2015.09.023.

6. Gong, Y., Yong, D., Liu, G., Xu, J., Ding, J., and Jia, W. (2024). A Novel Self-Amplifying mRNA with Decreased Cytotoxicity and Enhanced Protein Expression by Macrodomain Mutations. Advanced Science *n/a*, 2402936. https://doi.org/10.1002/advs.202402936.

7. Gorchakov, R., Frolova, E., Williams, B.R.G., Rice, C.M., and Frolov, I. (2004). PKR-Dependent and -Independent Mechanisms Are Involved in Translational Shutoff during Sindbis Virus Infection. Journal of Virology *78*, 8455–8467. https://doi.org/10.1128/jvi.78.16.8455-8467.2004.

8. Dominguez, F., Palchevska, O., Frolova, E.I., and Frolov, I. (2023). Alphavirus-based replicons demonstrate different interactions with host cells and can be optimized to increase protein expression. Journal of Virology *97*, e01225-23. https://doi.org/10.1128/jvi.01225-23.

9. Vanluchene, H., Gillon, O., Peynshaert, K., De Smedt, S.C., Sanders, N., Raemdonck, K., and Remaut, K. (2024). Less is more: Self-amplifying mRNA becomes self-killing upon dose escalation in immune-competent retinal cells. European Journal of Pharmaceutics and Biopharmaceutics *196*, 114204. https://doi.org/10.1016/j.ejpb.2024.114204.

983 10. Frolov, I., and Schlesinger, S. (1994). Comparison of the effects of Sindbis virus and Sindbis virus
984 replicons on host cell protein synthesis and cytopathogenicity in BHK cells. J Virol *68*, 1721–1727.
985 https://doi.org/10.1128/jvi.68.3.1721-1727.1994.

986 11. Terenzi, F., deVeer, M.J., Ying, H., Restifo, N.P., Williams, B.R., and Silverman, R.H. (1999). The
987 antiviral enzymes PKR and RNase L suppress gene expression from viral and non-viral based vectors.
988 Nucleic Acids Res *27*, 4369–4375. https://doi.org/10.1093/nar/27.22.4369.

989 12. Li, Y., Su, Z., Zhao, W., Zhang, X., Momin, N., Zhang, C., Wittrup, K.D., Dong, Y., Irvine, D.J., and
990 Weiss, R. (2020). Multifunctional oncolytic nanoparticles deliver self-replicating IL-12 RNA to
991 eliminate established tumors and prime systemic immunity. Nat Cancer *1*, 882–893.
992 https://doi.org/10.1038/s43018-020-0095-6.

993 13. Venticinque, L., and Meruelo, D. (2010). Sindbis viral vector induced apoptosis requires translational
994 inhibition and signaling through Mcl-1 and Bak. Mol Cancer *9*, 37. https://doi.org/10.1186/1476-
995 4598-9-37.

996 14. Mastrangelo, A.J., Hardwick, J.M., Bex, F., and Betenbaugh, M.J. (2000). Part I. Bcl-2 and Bcl-x(L)
997 limit apoptosis upon infection with alphavirus vectors. Biotechnol Bioeng *67*, 544–554.

998 15. Frolov, I., Agapov, E., Thomas A Hoffman, J., Prágai, B.M., Lippa, M., Schlesinger, S., and Rice, C.M.
999 (1999). Selection of RNA Replicons Capable of Persistent Noncytopathic Replication in Mammalian
1000 Cells. Journal of Virology *73*, 3854. https://doi.org/10.1128/jvi.73.5.3854-3865.1999.

1001 16. Lundstrom, K., Abenavoli, A., Malgaroli, A., and Ehrengruber, M.U. (2003). Novel semliki forest virus
1002 vectors with reduced cytotoxicity and temperature sensitivity for long-term enhancement of
1003 transgene expression. Molecular Therapy *7*, 202–209. https://doi.org/10.1016/S1525-
1004 0016(02)00056-4.

1005 17. Pepini, T., Pulichino, A.-M., Carsillo, T., Carlson, A.L., Sari-Sarraf, F., Ramsauer, K., Debasitis, J.C.,
1006 Maruggi, G., Otten, G.R., Geall, A.J., et al. (2017). Induction of an IFN-Mediated Antiviral Response
1007 by a Self-Amplifying RNA Vaccine: Implications for Vaccine Design. The Journal of Immunology *198*,
1008 4012–4024. https://doi.org/10.4049/jimmunol.1601877.

1009 18. Blakney, A.K., McKay, P.F., Bouton, C.R., Hu, K., Samnuan, K., and Shattock, R.J. (2021). Innate
1010 Inhibiting Proteins Enhance Expression and Immunogenicity of Self-Amplifying RNA. Mol Ther *29*,
1011 1174–1185. https://doi.org/10.1016/j.ymthe.2020.11.011.

1012 19. Blakney, A.K., Ip, S., and Geall, A.J. (2021). An Update on Self-Amplifying mRNA Vaccine
1013 Development. Vaccines (Basel) *9*, 97. https://doi.org/10.3390/vaccines9020097.

1014 20. Minnaert, A.-K., Vanluchene, H., Verbeke, R., Lentacker, I., De Smedt, S.C., Raemdonck, K., Sanders,
1015 N.N., and Remaut, K. (2021). Strategies for controlling the innate immune activity of conventional
1016 and self-amplifying mRNA therapeutics: Getting the message across. Adv Drug Deliv Rev *176*,
1017 113900. https://doi.org/10.1016/j.addr.2021.113900.

1018 21. Erasmus, J.H., Archer, J., Fuerte-Stone, J., Khandhar, A.P., Voigt, E., Granger, B., Bombardi, R.G.,
1019 Govero, J., Tan, Q., Durnell, L.A., et al. (2020). Intramuscular Delivery of Replicon RNA Encoding

1020 ZIKV-117 Human Monoclonal Antibody Protects against Zika Virus Infection. Molecular Therapy
1021 Methods & Clinical Development *18*, 402–414. https://doi.org/10.1016/j.omtm.2020.06.011.

1022 22. Yoshioka, N., Gros, E., Li, H.-R., Kumar, S., Deacon, D.C., Maron, C., Muotri, A.R., Chi, N.C., Fu, X.-D.,
1023 Yu, B.D., et al. (2013). Efficient Generation of Human iPS Cells by a Synthetic Self-Replicative RNA.
1024 Cell Stem Cell *13*, 10.1016/j.stem.2013.06.001. https://doi.org/10.1016/j.stem.2013.06.001.

1025 23. Kim, Y.G., Baltabekova, A.Z., Zhiyenbay, E.E., Aksambayeva, A.S., Shagyrova, Z.S., Khannanov, R.,
1026 Ramanculov, E.M., and Shustov, A.V. (2017). Recombinant Vaccinia virus-coded interferon inhibitor
1027 B18R: Expression, refolding and a use in a mammalian expression system with a RNA-vector. PLOS
1028 ONE *12*, e0189308. https://doi.org/10.1371/journal.pone.0189308.

1029 24. McGee, J.E., Kirsch, J.R., Kenney, D., Cerbo, F., Chavez, E.C., Shih, T.-Y., Douam, F., Wong, W.W., and
1030 Grinstaff, M.W. (2024). Complete substitution with modified nucleotides in self-amplifying RNA
1031 suppresses the interferon response and increases potency. Nat Biotechnol, 1–7.
1032 https://doi.org/10.1038/s41587-024-02306-z.

1033 25. Zhong, Z., McCafferty, S., Opsomer, L., Wang, H., Huysmans, H., De Temmerman, J., Lienenklaus, S.,
1034 Portela Catani, J.P., Combes, F., and Sanders, N.N. (2021). Corticosteroids and cellulose purification
1035 improve, respectively, the in vivo translation and vaccination efficacy of sa-mRNAs. Molecular
1036 Therapy *29*, 1370–1381. https://doi.org/10.1016/j.ymthe.2021.01.023.

1037 26. Beissert, T., Koste, L., Perkovic, M., Walzer, K.C., Erbar, S., Selmi, A., Diken, M., Kreiter, S., Türeci, Ö.,
1038 and Sahin, U. (2017). Improvement of In Vivo Expression of Genes Delivered by Self-Amplifying RNA
1039 Using Vaccinia Virus Immune Evasion Proteins. Hum Gene Ther *28*, 1138–1146.
1040 https://doi.org/10.1089/hum.2017.121.

1041 27. Xue, Y., Zhang, Y., Zhong, Y., Du, S., Hou, X., Li, W., Li, H., Wang, S., Wang, C., Yan, J., et al. (2024).
1042 LNP-RNA-engineered adipose stem cells for accelerated diabetic wound healing. Nat Commun *15*,
1043 739. https://doi.org/10.1038/s41467-024-45094-5.

1044 28. Li, Y., Teague, B., Zhang, Y., Su, Z., Porter, E., Dobosh, B., Wagner, T., Irvine, D.J., and Weiss, R.
1045 (2019). In vitro evolution of enhanced RNA replicons for immunotherapy. Sci Rep *9*, 6932.
1046 https://doi.org/10.1038/s41598-019-43422-0.

1047 29. Merrick, W.C. (2004). Cap-dependent and cap-independent translation in eukaryotic systems. Gene
1048 *332*, 1–11. https://doi.org/10.1016/j.gene.2004.02.051.

1049 30. Yang, Y., and Wang, Z. (2019). IRES-mediated cap-independent translation, a path leading to hidden
1050 proteome. Journal of Molecular Cell Biology *11*, 911–919. https://doi.org/10.1093/jmcb/mjz091.

1051 31. Maglaviceanu, A., Wu, B., and Kapoor, M. (2021). Fibroblast-like synoviocytes: Role in synovial
1052 fibrosis associated with osteoarthritis. Wound Repair and Regeneration *29*, 642–649.
1053 https://doi.org/10.1111/wrr.12939.

1054 32. Mousavi, M.J., Karami, J., Aslani, S., Tahmasebi, M.N., Vaziri, A.S., Jamshidi, A., Farhadi, E., and
1055 Mahmoudi, M. (2021). Transformation of fibroblast-like synoviocytes in rheumatoid arthritis; from a
1056 friend to foe. Autoimmun Highlights *12*, 3. https://doi.org/10.1186/s13317-020-00145-x.

1057 33. Honig, M.G., and Hume, R.I. (1986). Fluorescent carbocyanine dyes allow living neurons of identified
1058 origin to be studied in long-term cultures. J Cell Biol *103*, 171–187.
1059 https://doi.org/10.1083/jcb.103.1.171.

1060 34. Bertrand, R., Solary, E., O'Connor, P., Kohn, K.W., and Pommier, Y. (1994). Induction of a Common
1061 Pathway of Apoptosis by Staurosporine. Experimental Cell Research *211*, 314–321.
1062 https://doi.org/10.1006/excr.1994.1093.

1063 35. Rehwinkel, J., and Gack, M.U. (2020). RIG-I-like receptors: their regulation and roles in RNA sensing.
1064 Nat Rev Immunol *20*, 537–551. https://doi.org/10.1038/s41577-020-0288-3.

1065 36. Junior, A.G.D., Sampaio, N.G., and Rehwinkel, J. (2019). A Balancing Act: MDA5 in Antiviral Immunity
1066 and Autoinflammation. Trends in Microbiology *27*, 75–85.
1067 https://doi.org/10.1016/j.tim.2018.08.007.

1068 37. Gal-Ben-Ari, S., Barrera, I., Ehrlich, M., and Rosenblum, K. (2019). PKR: A Kinase to Remember.
1069 Front. Mol. Neurosci. *11*. https://doi.org/10.3389/fnmol.2018.00480.

1070 38. Silverman, R.H. (2007). Viral Encounters with 2′,5′-Oligoadenylate Synthetase and RNase L during
1071 the Interferon Antiviral Response. Journal of Virology *81*, 12720–12729.
1072 https://doi.org/10.1128/jvi.01471-07.

1073 39. Szczerba, M., Subramanian, S., Trainor, K., McCaughan, M., Kibler, K.V., and Jacobs, B.L. (2022).
1074 Small Hero with Great Powers: Vaccinia Virus E3 Protein and Evasion of the Type I IFN Response.
1075 Biomedicines *10*, 235. https://doi.org/10.3390/biomedicines10020235.

1076 40. Kalveram, B., and Ikegami, T. (2013). Toscana Virus NSs Protein Promotes Degradation of Double-
1077 Stranded RNA-Dependent Protein Kinase. J Virol *87*, 3710–3718. https://doi.org/10.1128/JVI.02506-
1078 12.

1079 41. Drappier, M., Jha, B.K., Stone, S., Elliott, R., Zhang, R., Vertommen, D., Weiss, S.R., Silverman, R.H.,
1080 and Michiels, T. (2018). A novel mechanism of RNase L inhibition: Theiler's virus L* protein prevents
1081 2-5A from binding to RNase L. PLoS Pathog *14*, e1006989.
1082 https://doi.org/10.1371/journal.ppat.1006989.

1083 42. Liu, Z., Chen, O., Wall, J.B.J., Zheng, M., Zhou, Y., Wang, L., Ruth Vaseghi, H., Qian, L., and Liu, J.
1084 (2017). Systematic comparison of 2A peptides for cloning multi-genes in a polycistronic vector. Sci
1085 Rep *7*, 2193. https://doi.org/10.1038/s41598-017-02460-2.

1086 43. Costigan, A., Hollville, E., and Martin, S.J. (2023). Discriminating Between Apoptosis, Necrosis,
1087 Necroptosis, and Ferroptosis by Microscopy and Flow Cytometry. Current Protocols *3*, e951.
1088 https://doi.org/10.1002/cpz1.951.

1089 44. Liu, Q., Huang, J., Xia, J., Liang, Y., and Li, G. (2022). Tracking tools of extracellular vesicles for
1090 biomedical research. Front. Bioeng. Biotechnol. *10*. https://doi.org/10.3389/fbioe.2022.943712.

1091 45. Chiaradia, E., Tancini, B., Emiliani, C., Delo, F., Pellegrino, R.M., Tognoloni, A., Urbanelli, L., and
1092 Buratta, S. (2021). Extracellular Vesicles under Oxidative Stress Conditions: Biological Properties and
1093 Physiological Roles. Cells *10*, 1763. https://doi.org/10.3390/cells10071763.

1094 46. van Genderen, H., Kenis, H., Lux, P., Ungeth, L., Maassen, C., Deckers, N., Narula, J., Hofstra, L., and
1095 Reutelingsperger, C. (2006). In vitro measurement of cell death with the annexin A5 affinity assay.
1096 Nat Protoc *1*, 363–367. https://doi.org/10.1038/nprot.2006.55.

1097 47. Crowley, L.C., Marfell, B.J., Scott, A.P., and Waterhouse, N.J. (2016). Quantitation of Apoptosis and
1098 Necrosis by Annexin V Binding, Propidium Iodide Uptake, and Flow Cytometry. Cold Spring Harb
1099 Protoc *2016*. https://doi.org/10.1101/pdb.prot087288.

1100 48. Chan, L.L., Wilkinson, A.R., Paradis, B.D., and Lai, N. (2012). Rapid Image-based Cytometry for
1101 Comparison of Fluorescent Viability Staining Methods. J Fluoresc *22*, 1301–1311.
1102 https://doi.org/10.1007/s10895-012-1072-y.

1103 49. Baird, T.D., and Wek, R.C. (2012). Eukaryotic Initiation Factor 2 Phosphorylation and Translational
1104 Control in Metabolism. Advances in Nutrition *3*, 307. https://doi.org/10.3945/an.112.002113.

1105 50. Mars, J.-C., Culjkovic-Kraljacic, B., and Borden, K.L.B. (2024). eIF4E orchestrates mRNA processing,
1106 RNA export and translation to modify specific protein production. Nucleus *15*, 2360196.
1107 https://doi.org/10.1080/19491034.2024.2360196.

1108 51. Burke, J.M., Moon, S.L., Matheny, T., and Parker, R. (2019). RNase L Reprograms Translation by
1109 Widespread mRNA Turnover Escaped by Antiviral mRNAs. Molecular Cell *75*, 1203-1217.e5.
1110 https://doi.org/10.1016/j.molcel.2019.07.029.

1111 52. Burke, J.M., Gilchrist, A.R., Sawyer, S.L., and Parker, R. (2021). RNase L limits host and viral protein
1112 synthesis via inhibition of mRNA export. Science Advances *7*, eabh2479.
1113 https://doi.org/10.1126/sciadv.abh2479.

1114 53. Donovan, J., Rath, S., Kolet-Mandrikov, D., and Korennykh, A. (2017). Rapid RNase L-driven arrest of
1115 protein synthesis in the dsRNA response without degradation of translation machinery. RNA *23*,
1116 1660–1671. https://doi.org/10.1261/rna.062000.117.

1117 54. Whelan, J.N., Li, Y., Silverman, R.H., and Weiss, S.R. (2019). Zika Virus Production Is Resistant to
1118 RNase L Antiviral Activity. J Virol *93*, e00313-19. https://doi.org/10.1128/JVI.00313-19.

1119 55. Paul, D., and Bartenschlager, R. (2013). Architecture and biogenesis of plus-strand RNA virus
1120 replication factories. World J Virol *2*, 32–48. https://doi.org/10.5501/wjv.v2.i2.32.

1121 56. Schroeder, A., Mueller, O., Stocker, S., Salowsky, R., Leiber, M., Gassmann, M., Lightfoot, S., Menzel,
1122 W., Granzow, M., and Ragg, T. (2006). The RIN: an RNA integrity number for assigning integrity
1123 values to RNA measurements. BMC Molecular Biology *7*, 3. https://doi.org/10.1186/1471-2199-7-3.

1124 57. Santoro, M.G., Rossi, A., and Amici, C. (2003). NF-κB and virus infection: who controls whom. The
1125 EMBO Journal *22*, 2552–2560. https://doi.org/10.1093/emboj/cdg267.

1126 58. Mitchell, J.P., and Carmody, R.J. (2018). Chapter Two - NF-κB and the Transcriptional Control of
1127 Inflammation. In International Review of Cell and Molecular Biology Transcriptional Gene Regulation
1128 in Health and Disease., F. Loos, ed. (Academic Press), pp. 41–84.
1129 https://doi.org/10.1016/bs.ircmb.2017.07.007.

1130 59. Lee, Y.-R., Kweon, S.-H., Kwon, K.-B., Park, J.-W., Yoon, T.-R., and Park, B.-H. (2009). Inhibition of IL-
1131 1β-mediated inflammatory responses by the IκBα super-repressor in human fibroblast-like
1132 synoviocytes. Biochemical and Biophysical Research Communications *378*, 90–94.
1133 https://doi.org/10.1016/j.bbrc.2008.11.002.

1134 60. Brown, K., Gerstberger, S., Carlson, L., Franzoso, G., and Siebenlist, U. (1995). Control of IκB-α
1135 Proteolysis by Site-Specific, Signal-Induced Phosphorylation. Science *267*, 1485–1488.
1136 https://doi.org/10.1126/science.7878466.

1137 61. Yan, X., Liu, Z., and Chen, Y. (2009). Regulation of TGF-β signaling by Smad7. Acta Biochimica et
1138 Biophysica Sinica *41*, 263–272. https://doi.org/10.1093/abbs/gmp018.

1139 62. Sobah, M.L., Liongue, C., and Ward, A.C. (2021). SOCS Proteins in Immunity, Inflammatory Diseases,
1140 and Immune-Related Cancer. Front Med (Lausanne) *8*, 727987.
1141 https://doi.org/10.3389/fmed.2021.727987.

1142 63. Dimitriou, I.D., Clemenza, L., Scotter, A.J., Chen, G., Guerra, F.M., and Rottapel, R. (2008). Putting
1143 out the fire: coordinated suppression of the innate and adaptive immune systems by SOCS1 and
1144 SOCS3 proteins. Immunological Reviews *224*, 265–283. https://doi.org/10.1111/j.1600-
1145 065X.2008.00659.x.

1146 64. Blumer, T., Coto-Llerena, M., Duong, F.H.T., and Heim, M.H. (2017). SOCS1 is an inducible negative
1147 regulator of interferon λ (IFN-λ)-induced gene expression in vivo. J Biol Chem *292*, 17928–17938.
1148 https://doi.org/10.1074/jbc.M117.788877.

1149 65. Bauer, S., Jendro, M.C., Wadle, A., Kleber, S., Stenner, F., Dinser, R., Reich, A., Faccin, E., Gödde, S.,
1150 Dinges, H., et al. (2006). Fibroblast activation protein is expressed by rheumatoid myofibroblast-like
1151 synoviocytes. Arthritis Res Ther *8*, R171. https://doi.org/10.1186/ar2080.

1152 66. Zhang, H.E., Hamson, E.J., Koczorowska, M.M., Tholen, S., Chowdhury, S., Bailey, C.G., Lay, A.J.,
1153 Twigg, S.M., Lee, Q., Roediger, B., et al. (2019). Identification of Novel Natural Substrates of
1154 Fibroblast Activation Protein-alpha by Differential Degradomics and Proteomics. Mol Cell
1155 Proteomics *18*, 65–85. https://doi.org/10.1074/mcp.RA118.001046.

1156 67. Fan, A., Wu, G., Wang, J., Lu, L., Wang, J., Wei, H., Sun, Y., Xu, Y., Mo, C., Zhang, X., et al. (2023).
1157 Inhibition of fibroblast activation protein ameliorates cartilage matrix degradation and osteoarthritis
1158 progression. Bone Res *11*, 1–12. https://doi.org/10.1038/s41413-022-00243-8.

1159 68. Croft, A.P., Campos, J., Jansen, K., Turner, J.D., Marshall, J., Attar, M., Savary, L., Wehmeyer, C.,
1160 Naylor, A.J., Kemble, S., et al. (2019). Distinct fibroblast subsets drive inflammation and damage in
1161 arthritis. Nature *570*, 246–251. https://doi.org/10.1038/s41586-019-1263-7.

1162 69. Boyd, D.F., Allen, E.K., Randolph, A.G., Guo, X.J., Weng, Y., Sanders, C.J., Bajracharya, R., Lee, N.K.,
1163 Guy, C.S., Vogel, P., et al. (2020). Exuberant fibroblast activity compromises lung function via
1164 ADAMTS-4. Nature *587*, 466–471. https://doi.org/10.1038/s41586-020-2877-5.

1165 70. Krausgruber, T., Fortelny, N., Fife-Gernedl, V., Senekowitsch, M., Schuster, L.C., Lercher, A., Nemc,
1166 A., Schmidl, C., Rendeiro, A.F., Bergthaler, A., et al. (2020). Structural cells are key regulators of

1167 organ-specific immune response. Nature *583*, 296–302. https://doi.org/10.1038/s41586-020-2424-
1168 4.

1169 71. Nagata, L.P., Wong, J.P., Hu, W., and Wu, J.Q. (2013). Vaccines and Therapeutics for the Encephalitic
1170 Alphaviruses. Future Virology *8*, 661–674. https://doi.org/10.2217/fvl.13.42.

1171 72. Chung, D., Schroeder, C.E., Sotsky, J., Yao, T., Roy, S., Smith, R.A., Tower, N.A., Noah, J.W., McKellip,
1172 S., Sosa, M., et al. (2010). ML336: Development of Quinazolinone-Based Inhibitors Against
1173 Venezuelan Equine Encephalitis Virus (VEEV). In Probe Reports from the NIH Molecular Libraries
1174 Program (National Center for Biotechnology Information (US)).

1175 73. Frolova, E.I., Palchevska, O., Dominguez, F., and Frolov, I. Alphavirus-induced transcriptional and
1176 translational shutoffs play major roles in blocking the formation of stress granules. J Virol *97*,
1177 e00979-23. https://doi.org/10.1128/jvi.00979-23.

1178 74. Berglund, P., Finzi, D., Bennink, J.R., and Yewdell, J.W. (2007). Viral Alteration of Cellular
1179 Translational Machinery Increases Defective Ribosomal Products. Journal of Virology *81*, 7220–
1180 7229. https://doi.org/10.1128/jvi.00137-07.

1181 75. Fros, J.J., and Pijlman, G.P. (2016). Alphavirus Infection: Host Cell Shut-Off and Inhibition of Antiviral
1182 Responses. Viruses *8*, 166. https://doi.org/10.3390/v8060166.

1183 76. Fernandez, J., Yaman, I., Sarnow, P., Snider, M.D., and Hatzoglou, M. (2002). Regulation of Internal
1184 Ribosomal Entry Site-mediated Translation by Phosphorylation of the Translation Initiation Factor
1185 eIF2α*. Journal of Biological Chemistry *277*, 19198–19205.
1186 https://doi.org/10.1074/jbc.M201052200.

1187 77. Scheper, G.C., and Proud, C.G. (2002). Does phosphorylation of the cap-binding protein eIF4E play a
1188 role in translation initiation? European Journal of Biochemistry *269*, 5350–5359.
1189 https://doi.org/10.1046/j.1432-1033.2002.03291.x.

1190 78. Dyer, J.R., Michel, S., Lee, W., Castellucci, V.F., Wayne, N.L., and Sossin, W.S. (2003). An activity-
1191 dependent switch to cap-independent translation triggered by eIF4E dephosphorylation. Nat
1192 Neurosci *6*, 219–220. https://doi.org/10.1038/nn1018.

1193 79. Chang, C., Music, N., Cheung, M., Rossignol, E., Bedi, S., Patel, H., Safari, M., Lee, C., Otten, G.R.,
1194 Settembre, E.C., et al. (2022). Self-amplifying mRNA bicistronic influenza vaccines raise cross-
1195 reactive immune responses in mice and prevent infection in ferrets. Molecular Therapy Methods &
1196 Clinical Development *27*, 195–205. https://doi.org/10.1016/j.omtm.2022.09.013.

1197 80. Koch, A., Aguilera, L., Morisaki, T., Munsky, B., and Stasevich, T.J. (2020). Quantifying the dynamics
1198 of IRES and cap translation with single-molecule resolution in live cells. Nat Struct Mol Biol *27*,
1199 1095–1104. https://doi.org/10.1038/s41594-020-0504-7.

1200 81. Ho, C.K., and Shuman, S. (1996). Physical and Functional Characterization of the Double-Stranded
1201 RNA Binding Protein Encoded by the Vaccinia Virus E3 Gene. Virology *217*, 272–284.
1202 https://doi.org/10.1006/viro.1996.0114.

1203 82. Dueck, K.J., Hu, Y. (Sandy), Chen, P., Deschambault, Y., Lee, J., Varga, J., and Cao, J. (2015).
1204 Mutational Analysis of Vaccinia Virus E3 Protein: the Biological Functions Do Not Correlate with Its
1205 Biochemical Capacity To Bind Double-Stranded RNA. Journal of Virology *89*, 5382–5394.
1206 https://doi.org/10.1128/jvi.03288-14.

1207 83. Leitner, W.W., Hwang, L.N., Bergmann-Leitner, E.S., Finkelstein, S.E., Frank, S., and Restifo, N.P.
1208 (2004). Apoptosis is essential for the increased efficacy of alphaviral replicase-based DNA vaccines.
1209 Vaccine *22*, 1537–1544. https://doi.org/10.1016/j.vaccine.2003.10.013.

1210 84. Wu, Y.-Y., Sun, T.-K., Chen, M.-S., Munir, M., and Liu, H.-J. (2023). Oncolytic viruses-modulated
1211 immunogenic cell death, apoptosis and autophagy linking to virotherapy and cancer immune
1212 response. Front. Cell. Infect. Microbiol. *13*. https://doi.org/10.3389/fcimb.2023.1142172.

1213 85. Li, Y., Banerjee, S., Wang, Y., Goldstein, S.A., Dong, B., Gaughan, C., Silverman, R.H., and Weiss, S.R.
1214 (2016). Activation of RNase L is dependent on OAS3 expression during infection with diverse human
1215 viruses. Proc Natl Acad Sci U S A *113*, 2241–2246. https://doi.org/10.1073/pnas.1519657113.

1216 86. Zuo, W., Wakimoto, M., Kozaiwa, N., Shirasaka, Y., Oh, S.-W., Fujiwara, S., Miyachi, H., Kogure, A.,
1217 Kato, H., and Fujita, T. (2022). PKR and TLR3 trigger distinct signals that coordinate the induction of
1218 antiviral apoptosis. Cell Death Dis *13*, 1–15. https://doi.org/10.1038/s41419-022-05101-3.

1219 87. Xu, C., Gamil, A.A.A., Munang'andu, H.M., and Evensen, Ø. (2018). Apoptosis Induction by dsRNA-
1220 Dependent Protein Kinase R (PKR) in EPC Cells via Caspase 8 and 9 Pathways. Viruses *10*, 526.
1221 https://doi.org/10.3390/v10100526.

1222 88. Gil, J., and Esteban, M. (2000). The interferon-induced protein kinase (PKR), triggers apoptosis
1223 through FADD-mediated activation of caspase 8 in a manner independent of Fas and TNF-α
1224 receptors. Oncogene *19*, 3665–3674. https://doi.org/10.1038/sj.onc.1203710.

1225 89. Zhang, P., and Samuel, C.E. (2007). Protein Kinase PKR Plays a Stimulus- and Virus-Dependent Role
1226 in Apoptotic Death and Virus Multiplication in Human Cells. Journal of Virology *81*, 8192–8200.
1227 https://doi.org/10.1128/jvi.00426-07.

1228 90. Roretz, C. von, and Gallouzi, I.-E. (2010). Protein Kinase RNA/FADD/Caspase-8 Pathway Mediates
1229 the Proapoptotic Activity of the RNA-binding Protein Human Antigen R (HuR). The Journal of
1230 Biological Chemistry *285*, 16806. https://doi.org/10.1074/jbc.M109.087320.

1231 91. Xi, J., Snieckute, G., Martínez, J.F., Arendrup, F.S.W., Asthana, A., Gaughan, C., Lund, A.H., Bekker-
1232 Jensen, S., and Silverman, R.H. (2024). Initiation of a ZAKα-dependent ribotoxic stress response by
1233 the innate immunity endoribonuclease RNase L. Cell Reports *43*.
1234 https://doi.org/10.1016/j.celrep.2024.113998.

1235 92. Guydosh, N.R., Kimmig, P., Walter, P., and Green, R. (2017). Regulated Ire1-dependent mRNA decay
1236 requires no-go mRNA degradation to maintain endoplasmic reticulum homeostasis in S. pombe.
1237 eLife *6*, e29216. https://doi.org/10.7554/eLife.29216.

1238 93. Snieckute, G., Genzor, A.V., Vind, A.C., Ryder, L., Stoneley, M., Chamois, S., Dreos, R., Nordgaard, C.,
1239 Sass, F., Blasius, M., et al. (2022). Ribosome stalling is a signal for metabolic regulation by the

1240 ribotoxic stress response. Cell Metab *34*, 2036-2046.e8.
1241 https://doi.org/10.1016/j.cmet.2022.10.011.

1242 94. Li, G., Xiang, Y., Sabapathy, K., and Silverman, R.H. (2004). An Apoptotic Signaling Pathway in the
1243 Interferon Antiviral Response Mediated by RNase L and c-Jun NH2-terminal Kinase *. Journal of
1244 Biological Chemistry *279*, 1123–1131. https://doi.org/10.1074/jbc.M305893200.

1245 95. Samuel, C.E., Kuhen, K.L., George, C.X., Ortega, L.G., Rende-Fournier, R., and Tanaka, H. (1997). The
1246 PKR protein kinase--an interferon-inducible regulator of cell growth and differentiation. Int J
1247 Hematol *65*, 227–237. https://doi.org/10.1016/s0925-5710(96)00544-0.

1248 96. Iordanov, M.S., Wong, J., Bell, J.C., and Magun, B.E. (2001). Activation of NF-κB by Double-Stranded
1249 RNA (dsRNA) in the Absence of Protein Kinase R and RNase L Demonstrates the Existence of Two
1250 Separate dsRNA-Triggered Antiviral Programs. Molecular and Cellular Biology *21*, 61–72.
1251 https://doi.org/10.1128/MCB.21.1.61-72.2001.

1252 97. Herdy, B., Jaramillo, M., Svitkin, Y.V., Rosenfeld, A.B., Kobayashi, M., Walsh, D., Alain, T., Sean, P.,
1253 Robichaud, N., Topisirovic, I., et al. (2012). Translational control of the activation of transcription
1254 factor NF-κB and production of type I interferon by phosphorylation of the translation factor eIF4E.
1255 Nat Immunol *13*, 543–550. https://doi.org/10.1038/ni.2291.

1256 98. Liu, T., Zhang, L., Joo, D., and Sun, S.-C. (2017). NF-κB signaling in inflammation. Sig Transduct Target
1257 Ther *2*, 1–9. https://doi.org/10.1038/sigtrans.2017.23.

1258 99. Luo, J.-L., Kamata, H., and Karin, M. (2005). IKK/NF-κB signaling: balancing life and death – a new
1259 approach to cancer therapy. Journal of Clinical Investigation *115*, 2625–2632.
1260 https://doi.org/10.1172/JCI26322.

1261 100. Miagkov, A.V., Kovalenko, D.V., Brown, C.E., Didsbury, J.R., Cogswell, J.P., Stimpson, S.A.,
1262 Baldwin, A.S., and Makarov, S.S. (1998). NF-κB activation provides the potential link between
1263 inflammation and hyperplasia in the arthritic joint. Proceedings of the National Academy of Sciences
1264 *95*, 13859–13864. https://doi.org/10.1073/pnas.95.23.13859.

1265 101. Zhang, H.G., Huang, N., Liu, D., Bilbao, L., Zhang, X., Yang, P., Zhou, T., Curiel, D.T., and Mountz,
1266 J.D. (2000). Gene therapy that inhibits nuclear translocation of nuclear factor kappaB results in
1267 tumor necrosis factor alpha-induced apoptosis of human synovial fibroblasts. Arthritis Rheum *43*,
1268 1094–1105. https://doi.org/10.1002/1529-0131(200005)43:5<1094::AID-ANR20>3.0.CO;2-V.

1269 102. Xu, Y., Bialik, S., Jones, B.E., Iimuro, Y., Kitsis, R.N., Srinivasan, A., Brenner, D.A., and Czaja, M.J.
1270 (1998). NF-kappaB inactivation converts a hepatocyte cell line TNF-alpha response from
1271 proliferation to apoptosis. Am J Physiol *275*, C1058-1066.
1272 https://doi.org/10.1152/ajpcell.1998.275.4.C1058.

1273 103. Sago, C.D., Krupczak, B.R., Lokugamage, M.P., Gan, Z., and Dahlman, J.E. (2019). Cell Subtypes
1274 Within the Liver Microenvironment Differentially Interact with Lipid Nanoparticles. Cellular and
1275 Molecular Bioengineering *12*, 389. https://doi.org/10.1007/s12195-019-00573-4.

1276 104. Yamamura, Y., Hua, X., Bergelson, S., and Lodish, H.F. (2000). Critical Role of Smads and AP-1
1277 Complex in Transforming Growth Factor-β-dependent Apoptosis. Journal of Biological Chemistry
1278 *275*, 36295–36302. https://doi.org/10.1074/jbc.M006023200.

1279 105. Patil, S., Wildey, G.M., Brown, T.L., Choy, L., Derynck, R., and Howe, P.H. (2000). Smad7 is
1280 induced by CD40 and protects WEHI 231 B-lymphocytes from transforming growth factor-beta -
1281 induced growth inhibition and apoptosis. J Biol Chem *275*, 38363–38370.
1282 https://doi.org/10.1074/jbc.M004861200.

1283 106. Zitzmann, K., Brand, S., De Toni, E.N., Baehs, S., Göke, B., Meinecke, J., Spöttl, G., Meyer,
1284 H.H.H.D., and Auernhammer, C.J. (2007). SOCS1 Silencing Enhances Antitumor Activity of Type I IFNs
1285 by Regulating Apoptosis in Neuroendocrine Tumor Cells. Cancer Research *67*, 5025–5032.
1286 https://doi.org/10.1158/0008-5472.CAN-06-2575.

1287 107. Mann-Chandler, M.N., Kashyap, M., Wright, H.V., Norozian, F., Barnstein, B.O., Gingras, S.,
1288 Parganas, E., and Ryan, J.J. (2005). IFN-γ Induces Apoptosis in Developing Mast Cells1. The Journal of
1289 Immunology *175*, 3000–3005. https://doi.org/10.4049/jimmunol.175.5.3000.

1290 108. Kimura, A., Naka, T., Nagata, S., Kawase, I., and Kishimoto, T. (2004). SOCS-1 suppresses TNF-
1291 alpha-induced apoptosis through the regulation of Jak activation. Int Immunol *16*, 991–999.
1292 https://doi.org/10.1093/intimm/dxh102.

1293 109. Madonna, S., Scarponi, C., Pallotta, S., Cavani, A., and Albanesi, C. (2012). Anti-apoptotic effects
1294 of suppressor of cytokine signaling 3 and 1 in psoriasis. Cell Death Dis *3*, e334–e334.
1295 https://doi.org/10.1038/cddis.2012.69.

1296 110. Yan, L., Tang, Q., Shen, D., Peng, S., Zheng, Q., Guo, H., Jiang, M., and Deng, W. (2008). SOCS-1
1297 Inhibits TNF-α-Induced Cardiomyocyte Apoptosis via ERK1/2 Pathway Activation. Inflammation *31*,
1298 180–188. https://doi.org/10.1007/s10753-008-9063-5.

1299 111. Goker Bagca, B., and Biray Avci, C. (2020). The potential of JAK/STAT pathway inhibition by
1300 ruxolitinib in the treatment of COVID-19. Cytokine & Growth Factor Reviews *54*, 51–61.
1301 https://doi.org/10.1016/j.cytogfr.2020.06.013.

1302 112. Liau, N.P.D., Laktyushin, A., Lucet, I.S., Murphy, J.M., Yao, S., Whitlock, E., Callaghan, K., Nicola,
1303 N.A., Kershaw, N.J., and Babon, J.J. (2018). The molecular basis of JAK/STAT inhibition by SOCS1. Nat
1304 Commun *9*, 1558. https://doi.org/10.1038/s41467-018-04013-1.

1305 113. Skidmore, A.M., Adcock, R.S., Jonsson, C.B., Golden, J.E., and Chung, D.-H. (2020). Benzamidine
1306 ML336 inhibits plus and minus strand RNA synthesis of Venezuelan equine encephalitis virus
1307 without affecting host RNA production. Antiviral Research *174*, 104674.
1308 https://doi.org/10.1016/j.antiviral.2019.104674.

1309 114. Schroeder, C.E., Yao, T., Sotsky, J., Smith, R.A., Roy, S., Chu, Y.-K., Guo, H., Tower, N.A., Noah,
1310 J.W., McKellip, S., et al. (2014). Development of (E)-2-((1,4-Dimethylpiperazin-2-ylidene)amino)-5-
1311 nitro-N-phenylbenzamide, ML336: Novel 2-Amidinophenylbenzamides as Potent Inhibitors of
1312 Venezuelan Equine Encephalitis Virus. J. Med. Chem. *57*, 8608–8621.
1313 https://doi.org/10.1021/jm501203v.

1314 115. Tregoning, J.S., Stirling, D.C., Wang, Z., Flight, K.E., Brown, J.C., Blakney, A.K., McKay, P.F.,
1315 Cunliffe, R.F., Murugaiah, V., Fox, C.B., et al. (2023). Formulation, inflammation, and RNA sensing
1316 impact the immunogenicity of self-amplifying RNA vaccines. Molecular Therapy Nucleic Acids *31*,
1317 29–42. https://doi.org/10.1016/j.omtn.2022.11.024.

1318 116. Bathula, N.V., Friesen, J.J., Casmil, I.C., Wayne, C.J., Liao, S., Soriano, S.K.V., Ho, C.H., Strumpel,
1319 A., and Blakney, A.K. (2024). Delivery vehicle and route of administration influences self-amplifying
1320 RNA biodistribution, expression kinetics, and reactogenicity. Journal of Controlled Release *374*, 28–
1321 38. https://doi.org/10.1016/j.jconrel.2024.07.078.

1322 117. Oda, Y., Kumagai, Y., Kanai, M., Iwama, Y., Okura, I., Minamida, T., Yagi, Y., Kurosawa, T.,
1323 Greener, B., Zhang, Y., et al. (2024). Immunogenicity and safety of a booster dose of a self-
1324 amplifying RNA COVID-19 vaccine (ARCT-154) versus BNT162b2 mRNA COVID-19 vaccine: a double-
1325 blind, multicentre, randomised, controlled, phase 3, non-inferiority trial. The Lancet Infectious
1326 Diseases *24*, 351–360. https://doi.org/10.1016/S1473-3099(23)00650-3.

1327 118. Saraf, A., Gurjar, R., Kaviraj, S., Kulkarni, A., Kumar, D., Kulkarni, R., Virkar, R., Krishnan, J., Yadav,
1328 A., Baranwal, E., et al. (2024). An Omicron-specific, self-amplifying mRNA booster vaccine for COVID-
1329 19: a phase 2/3 randomized trial. Nat Med *30*, 1363–1372. https://doi.org/10.1038/s41591-024-
1330 02955-2.

1331 119. Roman-Blas, J.A., and Jimenez, S.A. (2006). NF-κB as a potential therapeutic target in
1332 osteoarthritis and rheumatoid arthritis. Osteoarthritis and Cartilage *14*, 839–848.
1333 https://doi.org/10.1016/j.joca.2006.04.008.

1334 120. Shen, J., Li, S., and Chen, D. (2014). TGF-β signaling and the development of osteoarthritis. Bone
1335 Res *2*, 1–7. https://doi.org/10.1038/boneres.2014.2.

1336 121. Zhou, Q., Ren, Q., Jiao, L., Huang, J., Yi, J., Chen, J., Lai, J., Ji, G., and Zheng, T. (2022). The
1337 potential roles of JAK/STAT signaling in the progression of osteoarthritis. Front. Endocrinol. *13*.
1338 https://doi.org/10.3389/fendo.2022.1069057.

1339 122. Blackwell, N.M., Sembi, P., Newson, J.S., Lawrence, T., Gilroy, D.W., and Kabouridis, P.S. (2004).
1340 Reduced infiltration and increased apoptosis of leukocytes at sites of inflammation by systemic
1341 administration of a membrane-permeable IκBα repressor. Arthritis & Rheumatism *50*, 2675–2684.
1342 https://doi.org/10.1002/art.20467.

1343 123. Chen, S.-Y., Shiau, A.-L., Wu, C.-L., and Wang, C.-R. (2016). Intraarticular overexpression of
1344 Smad7 ameliorates experimental arthritis. Sci Rep *6*, 35163. https://doi.org/10.1038/srep35163.

1345 124. Ha, Y.-J., Choi, Y.S., Kang, E.H., Shin, K., Kim, T.K., Song, Y.W., and Lee, Y.J. (2016). SOCS1
1346 suppresses IL-1β-induced C/EBPβ expression via transcriptional regulation in human chondrocytes.
1347 Exp Mol Med *48*, e241–e241. https://doi.org/10.1038/emm.2016.47.

1348 125. Freppel, W., Lim, E.X.Y., Rudd, P.A., and Herrero, L.J. (2024). Synoviocytes assist in modulating
1349 the effect of Ross River virus infection in micromass-cultured primary human chondrocytes. J Med
1350 Microbiol *73*, 001859. https://doi.org/10.1099/jmm.0.001859.

1351 126. Legros, V., Belarbi, E., Jeannin, P., Kümmerer, B., Hardy, D., Desprès, P., Gessain, A., Roques, P.,
1352 Ceccaldi, P.-E., and Choumet, V. (2024). A recombinant CHIKV-NLuc virus identifies chondrocytes as
1353 target of Chikungunya virus in a immunocompetent mouse model. Preprint at bioRxiv,
1354 https://doi.org/10.1101/2024.05.20.594924 https://doi.org/10.1101/2024.05.20.594924.

1355 127. Wäldele, S., Koers-Wunrau, C., Beckmann, D., Korb-Pap, A., Wehmeyer, C., Pap, T., and Dankbar,
1356 B. (2015). Deficiency of fibroblast activation protein alpha ameliorates cartilage destruction in
1357 inflammatory destructive arthritis. Arthritis Res Ther *17*, 12. https://doi.org/10.1186/s13075-015-
1358 0524-6.

1359 128. Petrakova, O., Volkova, E., Gorchakov, R., Paessler, S., Kinney, R.M., and Frolov, I. (2005).
1360 Noncytopathic Replication of Venezuelan Equine Encephalitis Virus and Eastern Equine Encephalitis
1361 Virus Replicons in Mammalian Cells. J Virol *79*, 7597–7608. https://doi.org/10.1128/JVI.79.12.7597-
1362 7608.2005.

1363 129. Hariri, F., Arguello, M., Volpon, L., Culjkovic-Kraljacic, B., Nielsen, T.H., Hiscott, J., Mann, K.K.,
1364 and Borden, K.L.B. (2013). The eukaryotic translation initiation factor eIF4E is a direct transcriptional
1365 target of NF-κB and is aberrantly regulated in acute myeloid leukemia. Leukemia *27*, 2047–2055.
1366 https://doi.org/10.1038/leu.2013.73.

1367 130. Uttam, S., Wong, C., Price, T.J., and Khoutorsky, A. (2018). eIF4E-Dependent Translational
1368 Control: A Central Mechanism for Regulation of Pain Plasticity. Front Genet *9*, 470.
1369 https://doi.org/10.3389/fgene.2018.00470.

1370 131. Siddiqui, N., and Sonenberg, N. (2015). Signalling to eIF4E in cancer. Biochemical Society
1371 Transactions *43*, 763–772. https://doi.org/10.1042/BST20150126.

1372 132. Gkogkas, C.G., Khoutorsky, A., Ran, I., Rampakakis, E., Nevarko, T., Weatherill, D.B., Vasuta, C.,
1373 Yee, S., Truitt, M., Dallaire, P., et al. (2013). Autism-related deficits via dysregulated eIF4E-
1374 dependent translational control. Nature *493*, 371–377. https://doi.org/10.1038/nature11628.

1375 133. Syntichaki, P., Troulinaki, K., and Tavernarakis, N. (2007). eIF4E function in somatic cells
1376 modulates ageing in Caenorhabditis elegans. Nature *445*, 922–926.
1377 https://doi.org/10.1038/nature05603.

1378 134. Costa-Mattioli, M., and Walter, P. (2020). The integrated stress response: From mechanism to
1379 disease. Science *368*, eaat5314. https://doi.org/10.1126/science.aat5314.

1380 135. Gadella, T.W.J., van Weeren, L., Stouthamer, J., Hink, M.A., Wolters, A.H.G., Giepmans, B.N.G.,
1381 Aumonier, S., Dupuy, J., and Royant, A. (2023). mScarlet3: a brilliant and fast-maturing red
1382 fluorescent protein. Nat Methods *20*, 541–545. https://doi.org/10.1038/s41592-023-01809-y.

1383 136. Costantini, L.M., Baloban, M., Markwardt, M.L., Rizzo, M.A., Guo, F., Verkhusha, V.V., and Snapp,
1384 E.L. (2015). A palette of fluorescent proteins optimized for diverse cellular environments. Nat
1385 Commun *6*, 7670. https://doi.org/10.1038/ncomms8670.

1386 137. Chakrabarti, S., Hore, Z., Pattison, L.A., Lalnunhlimi, S., Bhebhe, C.N., Callejo, G., Bulmer, D.C.,
1387 Taams, L.S., Denk, F., and Smith, E.S.J. (2020). Sensitization of knee-innervating sensory neurons by

tumor necrosis factor-α-activated fibroblast-like synoviocytes: an in vitro, coculture model of inflammatory pain. Pain *161*, 2129–2141. https://doi.org/10.1097/j.pain.0000000000001890.

138. Li, C.H., and Lee, C.K. (1993). Minimum cross entropy thresholding. Pattern Recognition *26*, 617–625. https://doi.org/10.1016/0031-3203(93)90115-D.

SUPPLEMENTAL INFORMATION

Document S1. Figures S1–S6

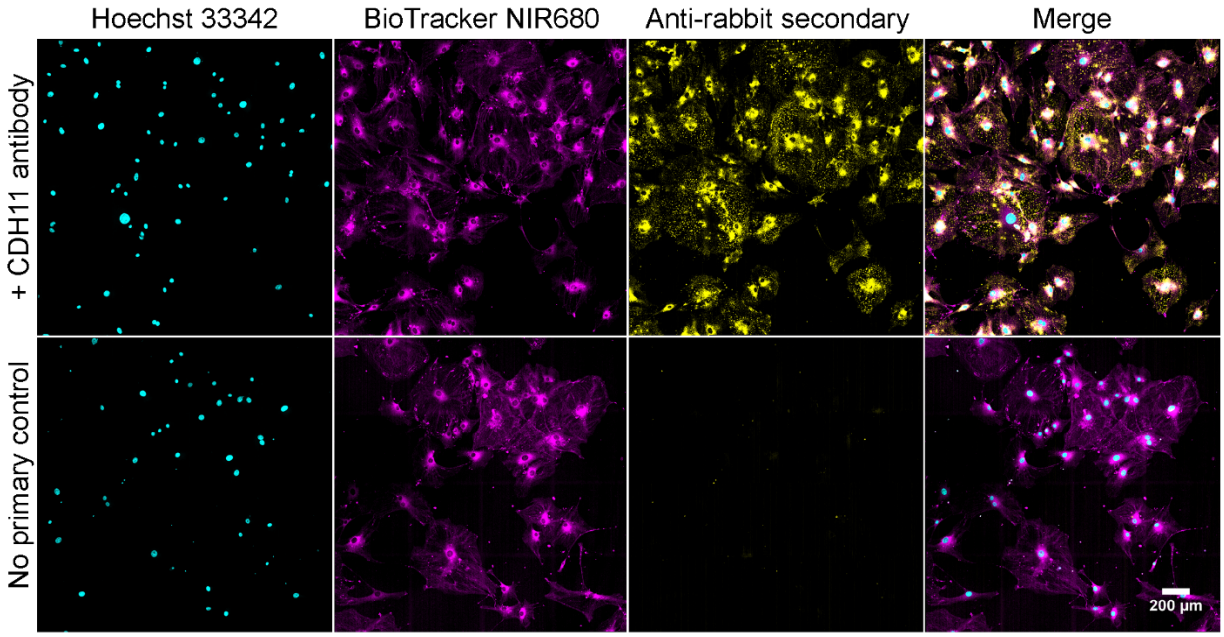

Fig. S1. Cadherin-11, a marker of fibroblast-like synoviocytes (FLS), stains cells isolated from mouse knee explants

Representative microscopy images of FLS isolated from mouse knee explants, stained with cadherin-11 (CDH11), an FLS marker. From left to right, columns show nuclear staining (Hoechst 33342, cyan), lipophilic membrane dye labeling (Biotracker NIR680, magenta), and Alexa 488 anti-rabbit secondary immunostaining (yellow), followed by a merged image. The top row shows cells treated with rabbit anti-CDH11 primary antibody, confirming CDH11 expression in isolated cells. The bottom row presents a no primary antibody control, showing no signal in the 488 channel. Scale bar = 200 µm.

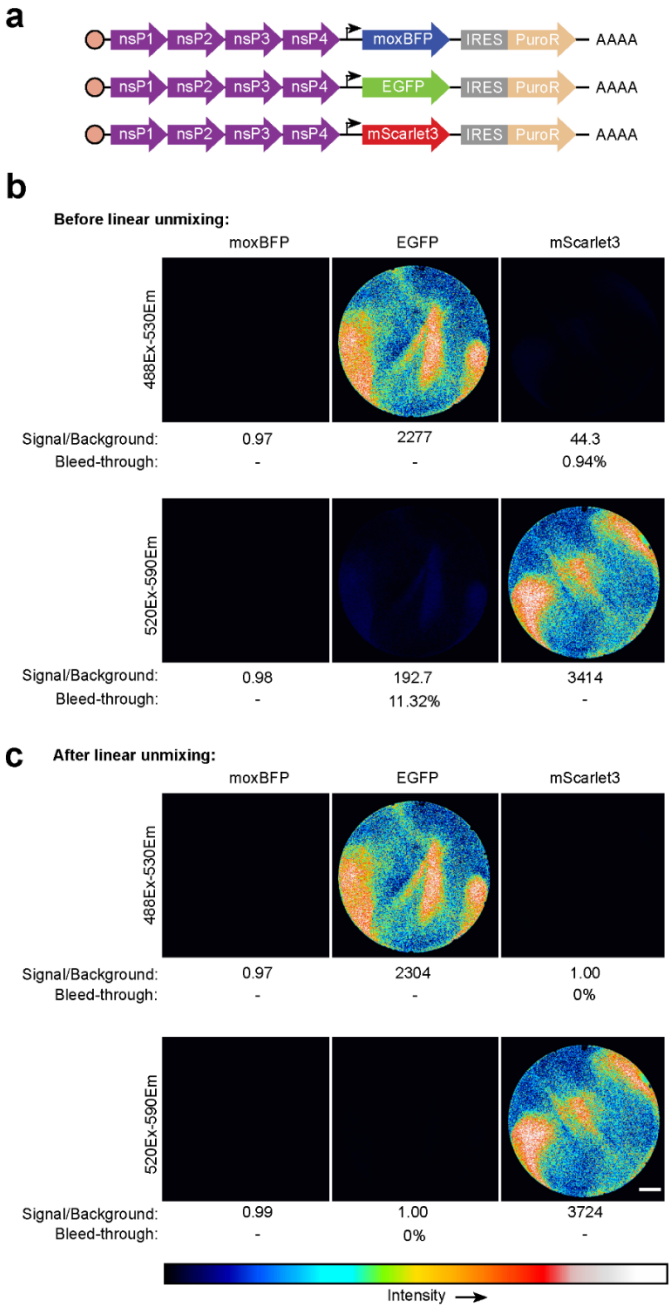

Fig. S2. Linear unmixing corrects spectral overlap of EGFP and mScarlet3 fluorescent signals imaged using the Odyssey M laser scanner

Schematic of the saRNA constructs used for linear unmixing, each expressing a different fluorescent protein: moxBFP, EGFP, and mScarlet3. These constructs were transfected into tSA201 cells. **b,** Representative imaging results showing fluorescence in the 488 and 520 channels, 1 day after transfection. moxBFP-transfected cells were not detected in either channel. EGFP was primarily detected in the 488 channel, with 11.32% bleedthrough into the 520 channel. mScarlet3 was primary detected in the 520 channel, with 0.94% bleedthrough into the 488 channel. Background signal was determined from mock transfected cells. **c,** Corrected images using linear unmixing to negate spectral bleedthrough from mScarlet3 and EGFP signals. Scale bars = 5 mm.

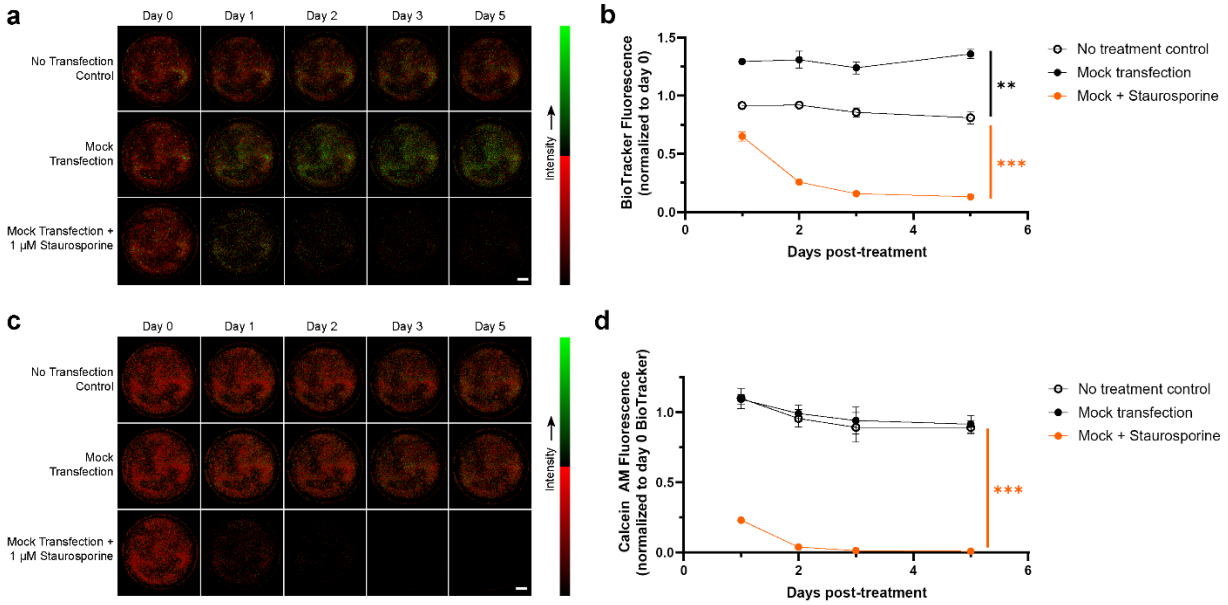

Fig. S3. BioTracker fluorescence indicates cell number following staurosporine-induced apoptosis, despite an increase after mock transfection

Validation of BioTracker fluorescence as a marker for cell number in the presence of apoptotic stimuli.
a, Representative images of FLS stained with BioTracker under three conditions: no transfection control, mock transfection, and mock transfection with 1 μM staurosporine. BioTracker fluorescence intensity increases after mock transfection but decreases following staurosporine treatment, indicating cell loss. Scale bar = 5 mm.
b, Quantification of BioTracker fluorescence over time for the three conditions (n = 3). Statistical significance was determined by two-way RM ANOVA with Dunnett's multiple comparisons test comparing groups to the no treatment control.
c, Representative images of the same FLS stained with Calcein AM. Unlike BioTracker, Calcein AM fluorescence does not increase after mock transfection but decreases after staurosporine treatment, reflecting apoptotic cell death. Scale bar = 5 mm.
d, Quantification of BioTracker fluorescence over time for the three conditions (n = 3). Fluorescence decreases following staurosporine treatment, consistent with findings in (a, b). Statistical significance was determined by two-way RM ANOVA with Dunnett's multiple comparisons test comparing groups to the no treatment control.
For all statistical reporting, **$P < 0.01$ and ***$P < 0.001$. Data are presented as mean ± SEM.

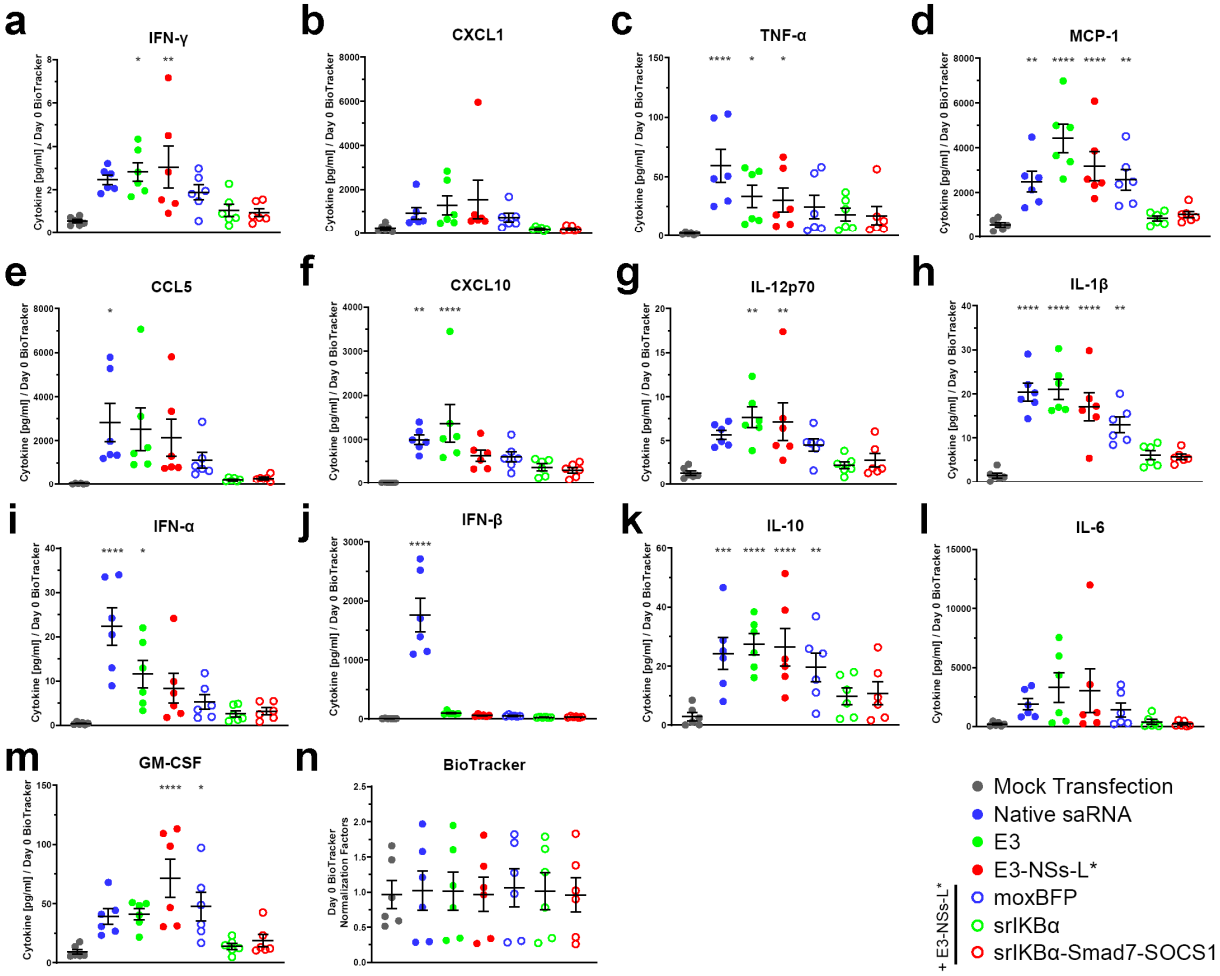

Fig. S4. Inhibition of dsRNA-sensing pathways and inflammatory signaling reduces saRNA-induced anti-viral cytokine secretion

Cytokines were collected from FLS 2 days post-transfection, quantified by bead-based immunoassay, and normalized by cell number using the BioTracker signal on day 0 (n = 6). Statistical significance for each cytokine was assessed using one-way RM ANOVA followed by Bonferroni's multiple comparisons test against the mock transfection control. A Bonferroni correction was applied to P values to account for multiple independent hypothesis testing. *P < 0.05, **P < 0.01, ***P < 0.001 and ****P < 0.0001. Data are presented as mean ± SEM.

a-m, Native saRNA induces anti-viral cytokine secretion. E3 reduces TNF-α (c), IFN-α (i), and IFN-β (j), secretion. E3-NSs-L* reduces CXCL10 secretion (f). srIκBα appears to reduce secretion of all cytokines tested. srIκBα-Smad7-SOCS1 does not reduce cytokine secretion more than srIκBα.

n, The BioTracker signal from day 0, used for normalizing differences in starting cell number, is shown.

Acronyms: IFN-γ, interferon-γ; CXCL1, C-X-C motif chemokine ligand 1; TNF-α, tumor necrosis factor-α; MCP-1, monocyte chemoattractant protein-1; IL-12p70, interleukin-12; CCL5, chemokine ligand 5; IL-1β, interleukin-1β; CXCL10, C-X-C motif chemokine ligand 10; GM-CSF, granulocyte-macrophage colony-stimulating factor; IL-10, interleukin-10; IFN-β, interferon-β; IFN-α, interferon-α; IL-6, interleukin-6.

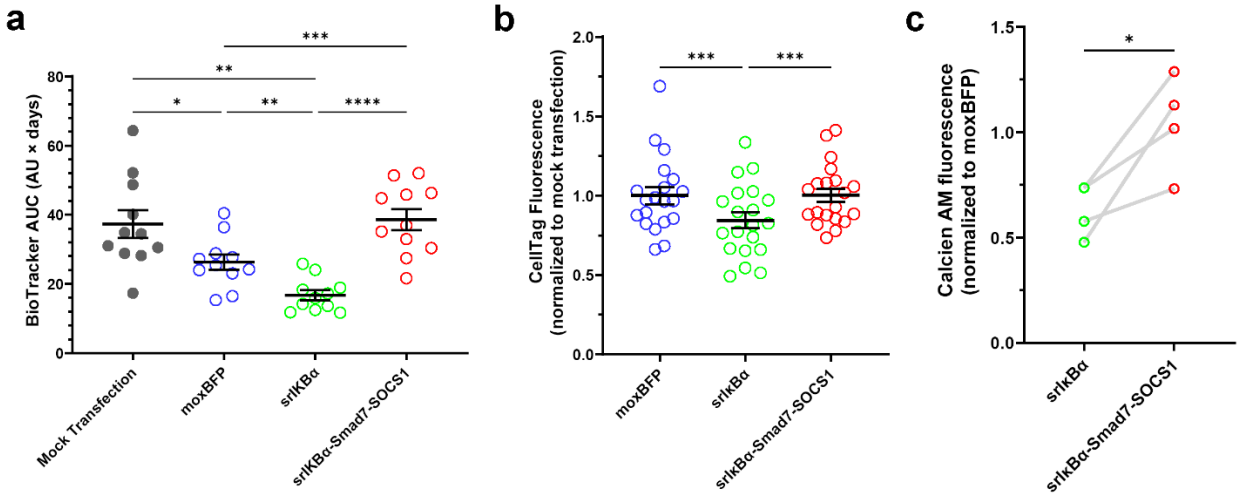

Fig. S5. srIκBα reduces cell number and viability, while srIκBα-Smad7-SOCS1 preserves both
a, AUC analysis of BioTracker fluorescence data shown in Fig. 5c, summarizing cumulative effects over the time course (n = 11). srIκBα induces reductions in integrated BioTracker signal, which is prevented by srIκBα-Smad7-SOCS1. Statistical analysis was performed using one-way RM ANOVA with Greenhouse–Geisser correction and Tukey's multiple comparisons test to compare all groups. Mock transfection data is also presented in Fig. 1g.
b, Quantification of mock transfection normalized CellTag signal (n = 20). The srIκBα construct reduces cell number, whereas this reduction is prevented by the srIκBα-Smad7-SOCS1 construct. Data were normalized to mock transfection. Statistical significance was determined by one-way RM ANOVA with Greenhouse–Geisser correction, and Tukey's multiple comparisons test. Data in this panel were pooled from in-cell western assays performed on day 2 post-transfection, incorporating data presented in Figs. 3 and 6 as well as additional data not shown elsewhere. ***$P < 0.001$.
c, Calcein AM staining performed 3 days post-transfection (n = 4). The srIκBα-Smad7-SOCS1 construct protects against reductions in cell viability induced by srIκBα. Data were normalized to the moxBFP construct. Statistical significance was determined by a paired t test. *$P<0.05$.
Data are presented as mean ± SEM. saRNA constructs used are shown in Fig. 4a.

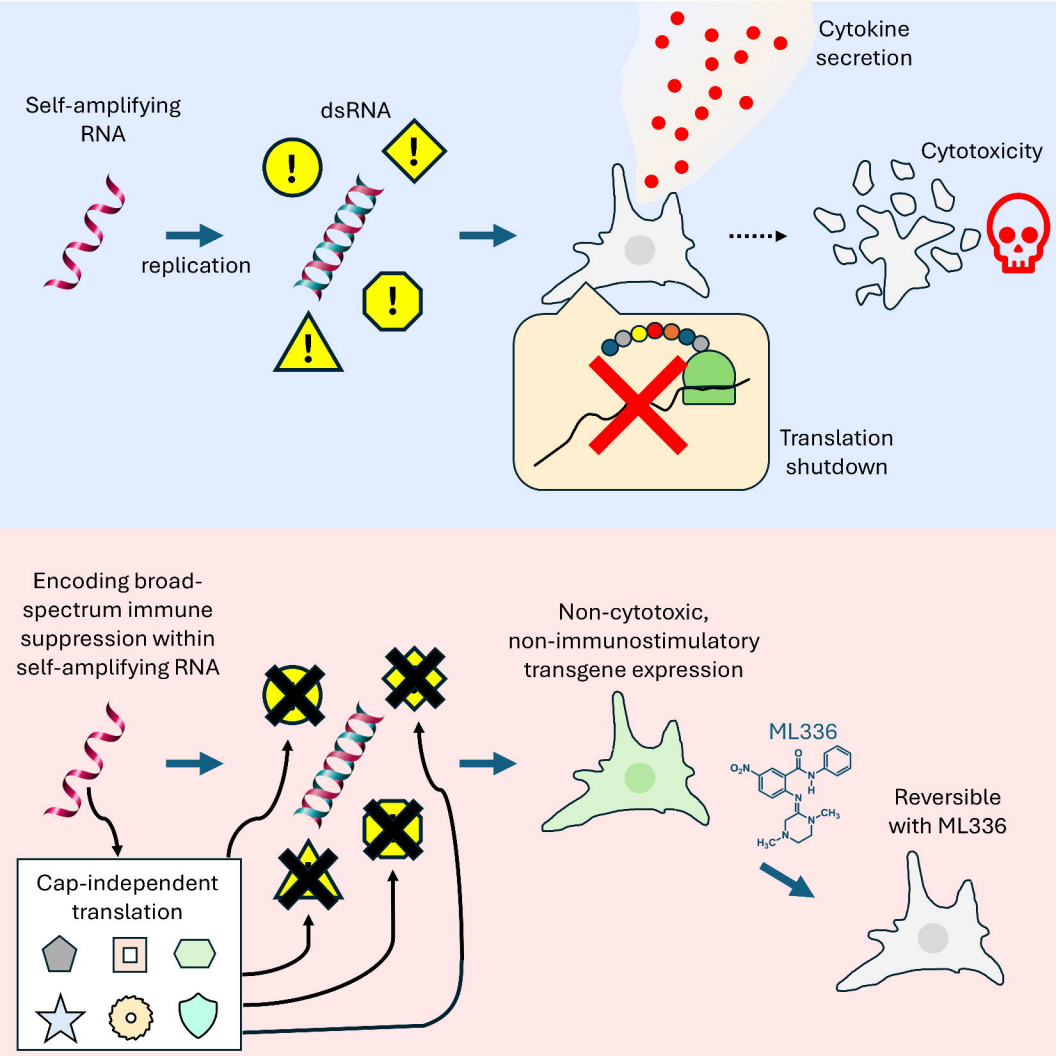
Self-amplifying RNA
replication
dsRNA
Cytokine secretion
Cytotoxicity
Translation shutdown
Encoding broad-spectrum immune suppression within self-amplifying RNA
Cap-independent translation
Non-cytotoxic, non-immunostimulatory transgene expression
ML336
Reversible with ML336

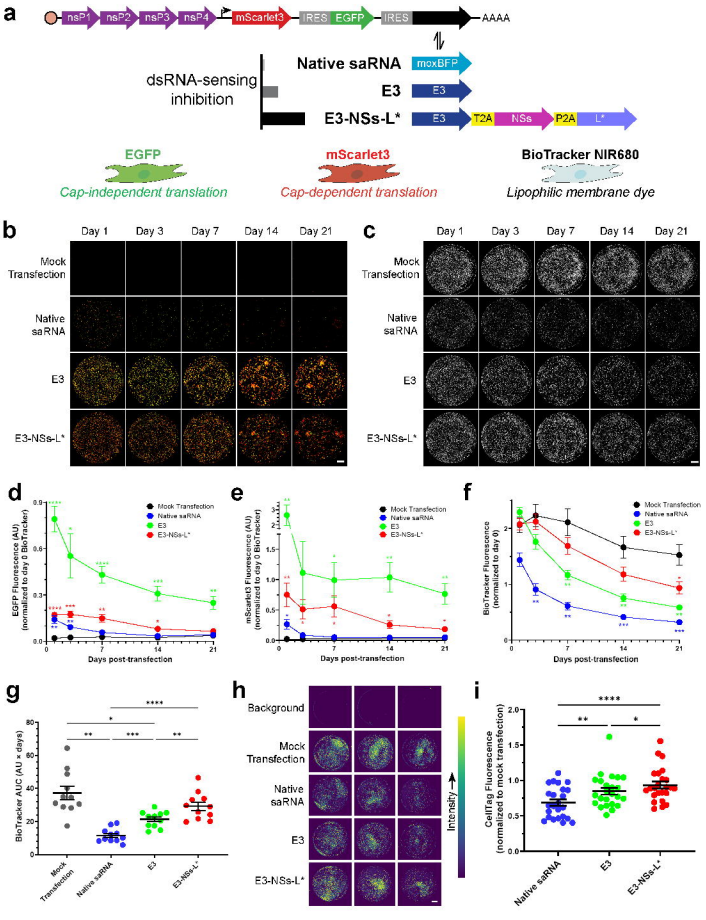
a
nsP1
nsP2
nsP3
nsP4
mScarlet3
IRES
EGFP
IRES
AAAA
dsRNA-sensing inhibition
Native saRNA
mcxBFP
E3
E3
E3-NSs-L*
E3
T2A
NSs
P2A
L*
EGFP
Cap-independent translation
mScarlet3
Cap-dependent translation
BioTracker NIR680
Lipophilic membrane dye
b
Day 1
Day 3
Day 7
Day 14
Day 21
Mock Transfection
Native saRNA
E3
E3-NSs-L*
c
Day 1
Day 3
Day 7
Day 14
Day 21
Mock Transfection
Native saRNA
E3
E3-NSs-L*
d
Mock Transfection
Native saRNA
E3
E3-NSs-L*
EGFP Fluorescence (AU)
(normalized to day 0 BioTracker)
Days post-transfection
e
Mock Transfection
Native saRNA
E3
E3-NSs-L*
mScarlet3 Fluorescence (AU)
(normalized to day 0 BioTracker)
Days post-transfection
f
Mock Transfection
Native saRNA
E3
E3-NSs-L*
BioTracker Fluorescence
(normalized to day 0)
Days post-transfection
g
BioTracker AUC (AU × days)
Mock Transfection
Native saRNA
E3
E3-NSs-L*
h
Background
Mock Transfection
Native saRNA
E3
E3-NSs-L*
Intensity
i
CellTag Fluorescence
(normalized to mock transfection)
Native saRNA
E3
E3-NSs-L*

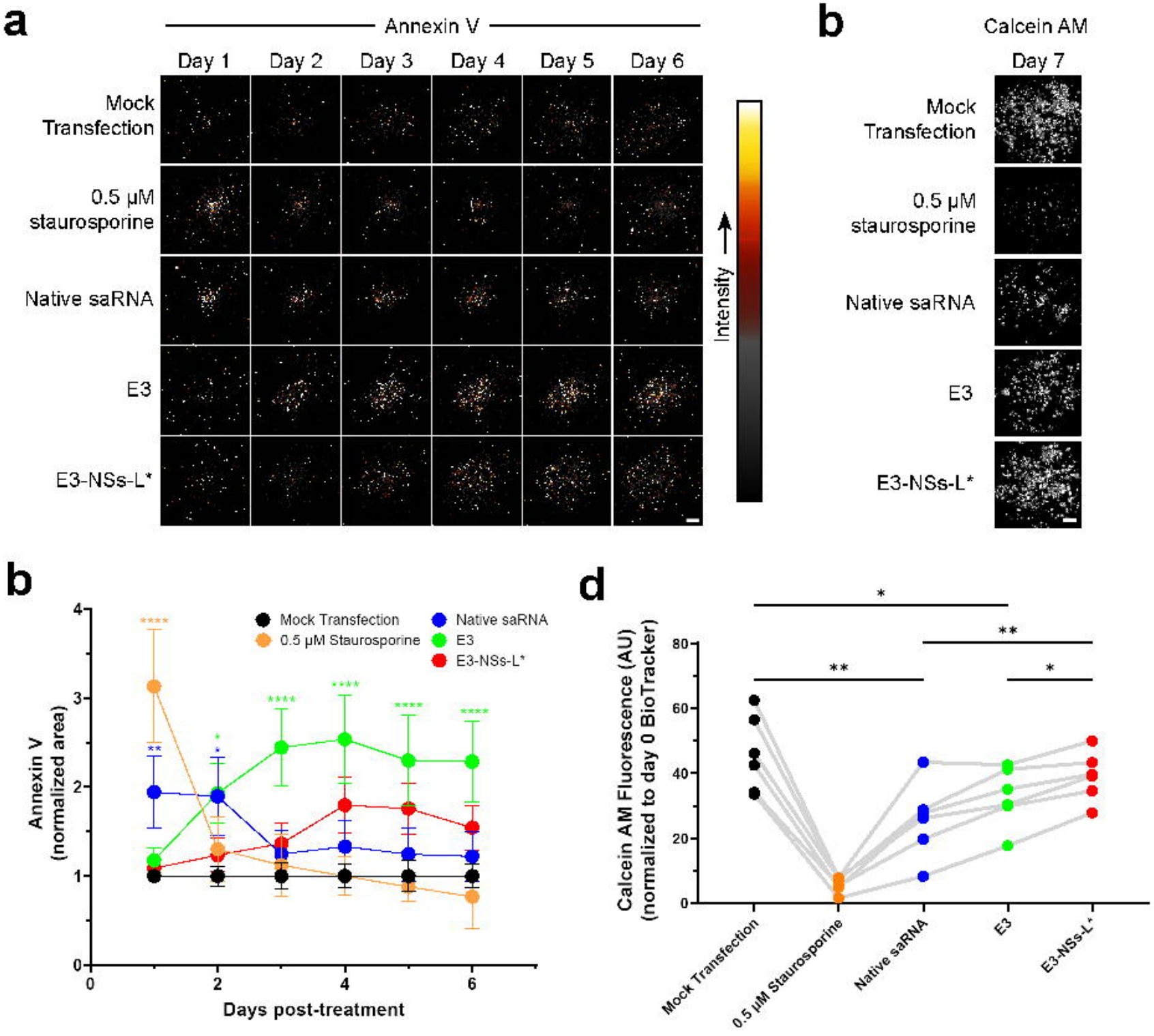
a
Annexin V
Day 1
Day 2
Day 3
Day 4
Day 5
Day 6
Mock Transfection
0.5 μM staurosporine
Native saRNA
E3
E3-NSs-L*
Intensity
b
Calcein AM
Day 7
Mock Transfection
0.5 μM staurosporine
Native saRNA
E3
E3-NSs-L*
b
Mock Transfection
0.5 μM Staurosporine
Native saRNA
E3
E3-NSs-L*
Annexin V (normalized area)
Days post-treatment
d
Calcein AM Fluorescence (AU) (normalized to day 0 BioTracker)
Mock Transfection
0.5 μM Staurosporine
Native saRNA
E3
E3-NSs-L*

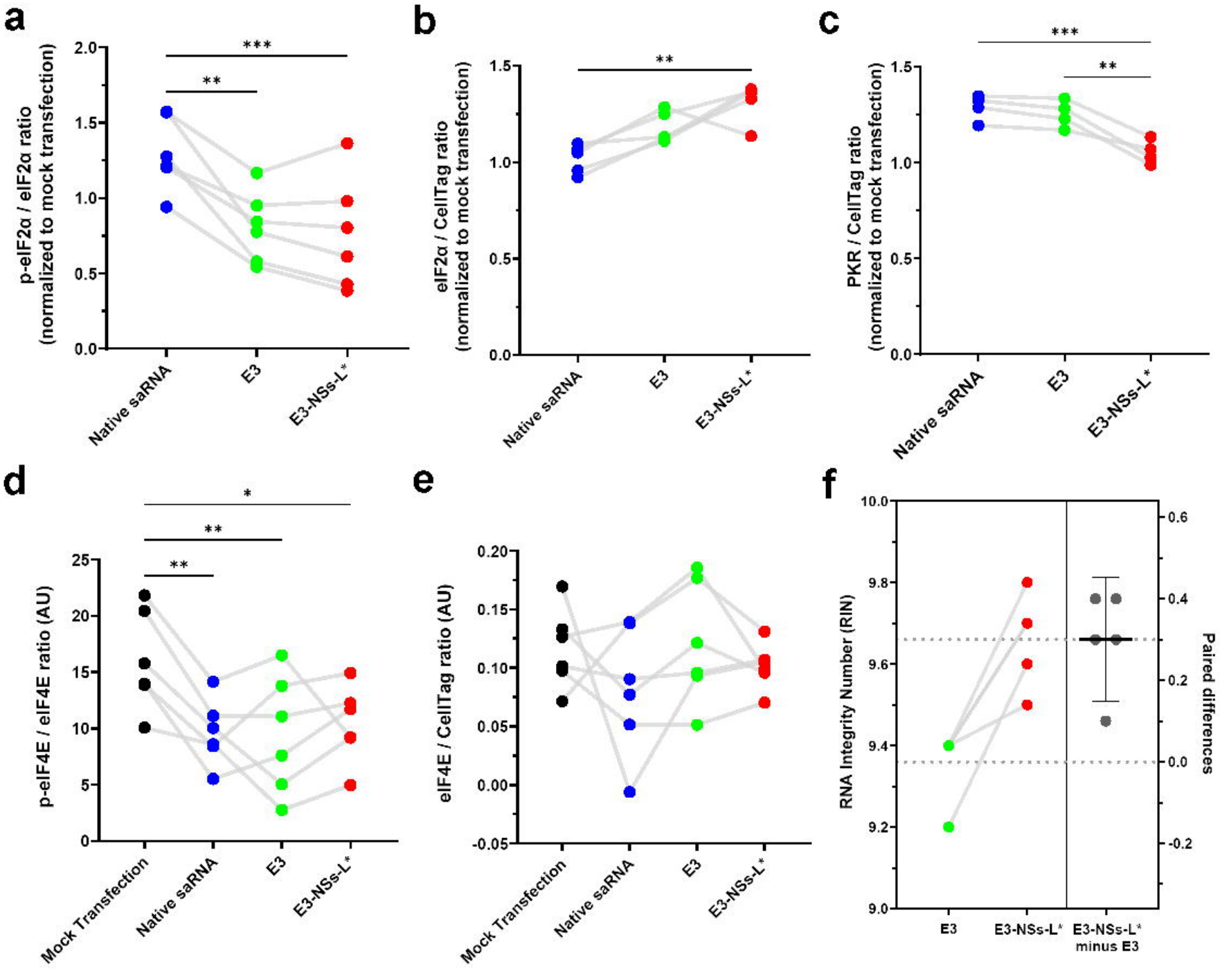
a
p-eIF2α / eIF2α ratio
(normalized to mock transfection)
2.0
1.5
1.0
0.5
0.0
***
**
Native saRNA
E3
E3-NSs-L*
b
eIF2α / CellTag ratio
(normalized to mock transfection)
1.5
1.0
0.5
0.0
**
Native saRNA
E3
E3-NSs-L*
c
PKR / CellTag ratio
(normalized to mock transfection)
1.5
1.0
0.5
0.0
***
**
Native saRNA
E3
E3-NSs-L*
d
p-eIF4E / eIF4E ratio (AU)
25
20
15
10
5
0
*
**
**
Mock Transfection
Native saRNA
E3
E3-NSs-L*
e
eIF4E / CellTag ratio (AU)
0.20
0.15
0.10
0.05
0.00
-0.05
Mock Transfection
Native saRNA
E3
E3-NSs-L*
f
RNA Integrity Number (RIN)
10.0
9.8
9.6
9.4
9.2
9.0
Paired differences
0.6
0.4
0.2
0.0
-0.2
E3
E3-NSs-L*
E3-NSs-L*
minus E3

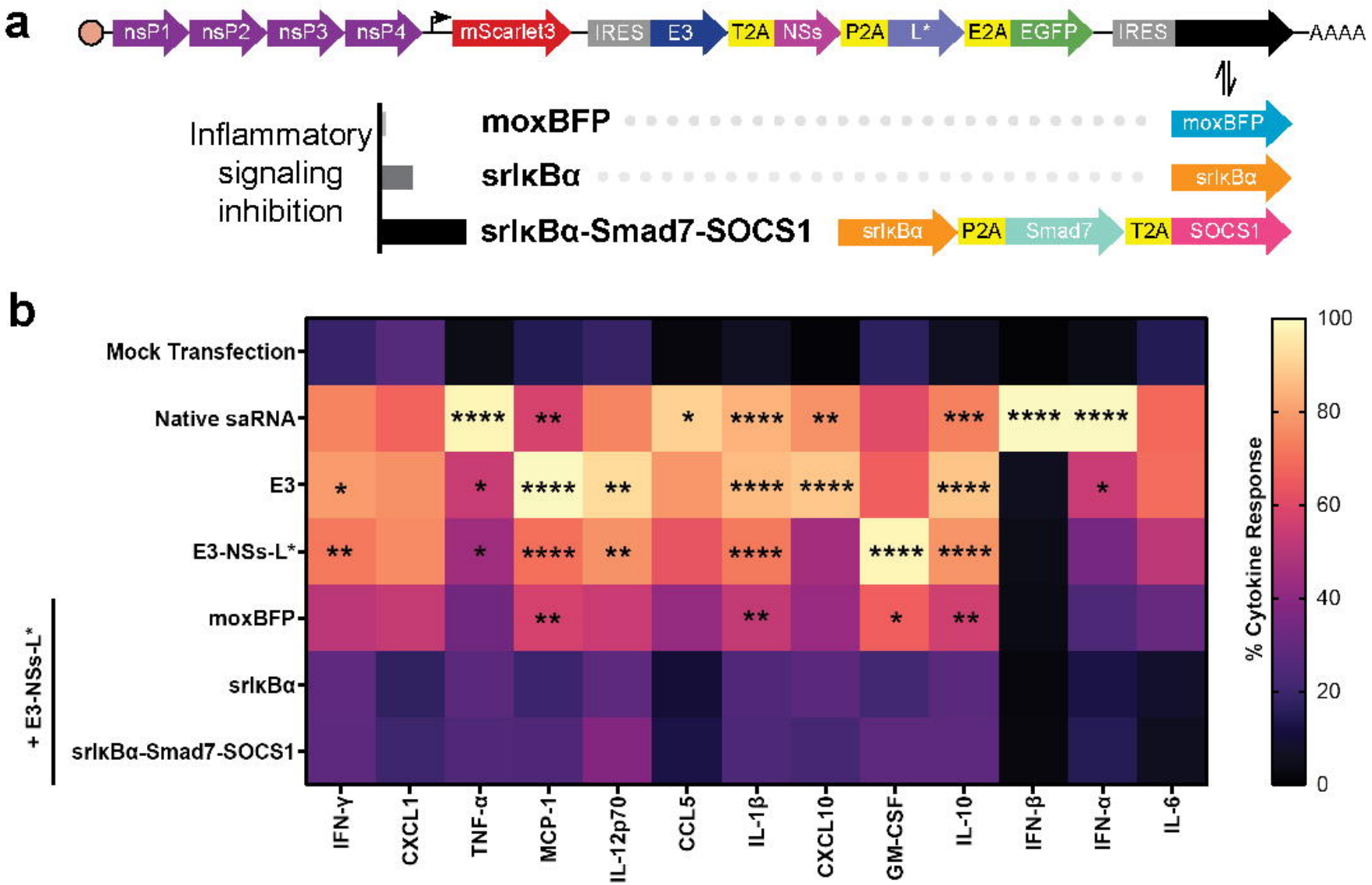
a
nsP1
nsP2
nsP3
nsP4
mScarlet3
IRES
E3
T2A
NSs
P2A
L*
E2A
EGFP
IRES
AAAA
Inflammatory signaling inhibition
moxBFP
srIκBα
srIκBα-Smad7-SOCS1
moxBFP
srIκBα
srIκBα
P2A
Smad7
T2A
SOCS1
b
Mock Transfection
Native saRNA
E3
E3-NSs-L*
moxBFP
srIκBα
srIκBα-Smad7-SOCS1
+ E3-NSs-L*
IFN-γ
CXCL1
TNF-α
MCP-1
IL-12p70
CCL5
IL-1β
CXCL10
GM-CSF
IL-10
IFN-β
IFN-α
IL-6
% Cytokine Response
100
80
60
40
20
0

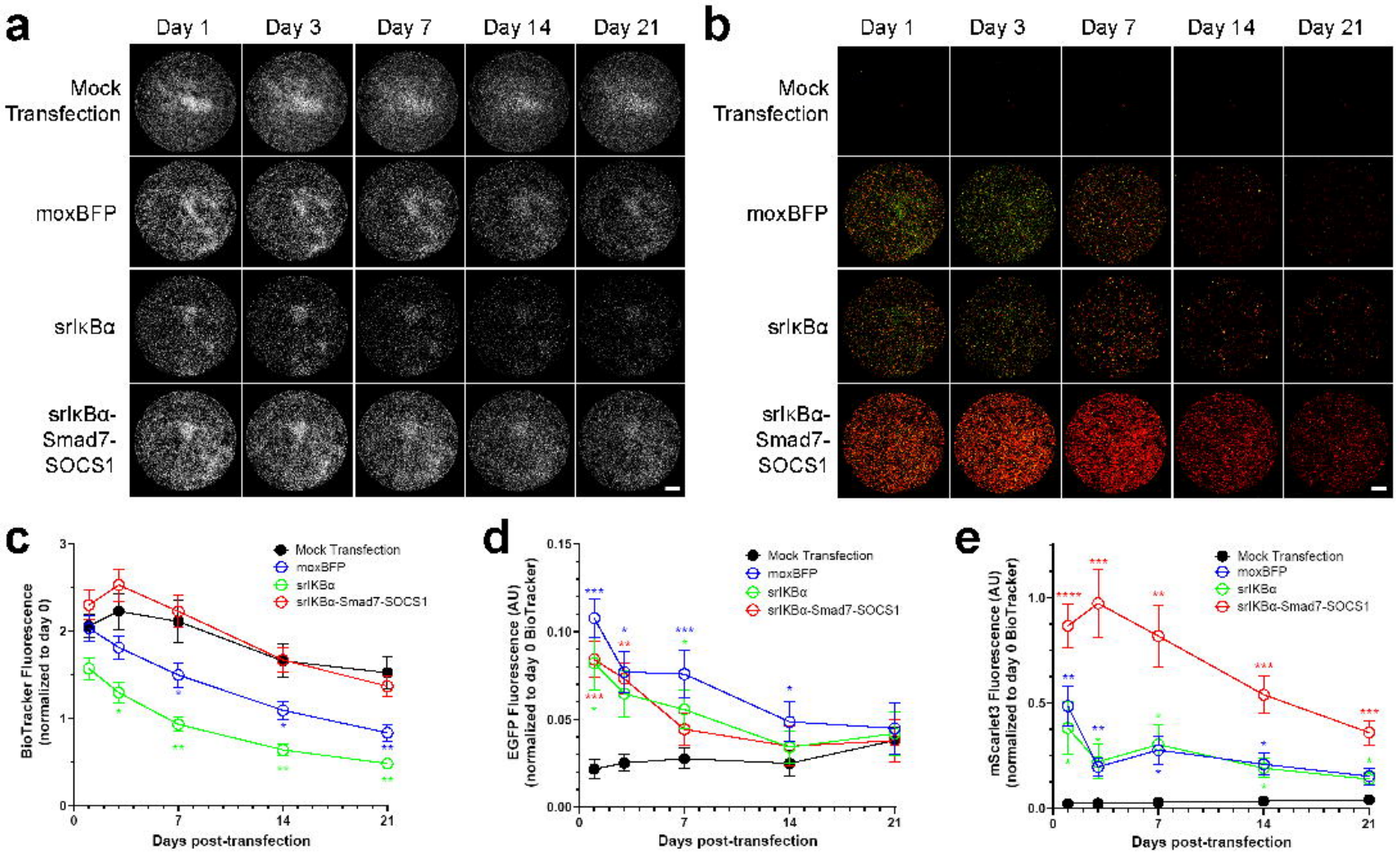
a
Day 1
Day 3
Day 7
Day 14
Day 21
Mock Transfection
moxBFP
srIκBα
srIκBα-Smad7-SOCS1
b
Day 1
Day 3
Day 7
Day 14
Day 21
Mock Transfection
moxBFP
srIκBα
srIκBα-Smad7-SOCS1
c
BioTracker Fluorescence (normalized to day 0)
Days post-transfection
Mock Transfection
moxBFP
srIKBα
srIKBα-Smad7-SOCS1
d
EGFP Fluorescence (AU) (normalized to day 0 BioTracker)
Days post-transfection
Mock Transfection
moxBFP
srIKBα
srIKBα-Smad7-SOCS1
e
mScarlet3 Fluorescence (AU) (normalized to day 0 BioTracker)
Days post-transfection
Mock Transfection
moxBFP
srIKBα
srIKBα-Smad7-SOCS1

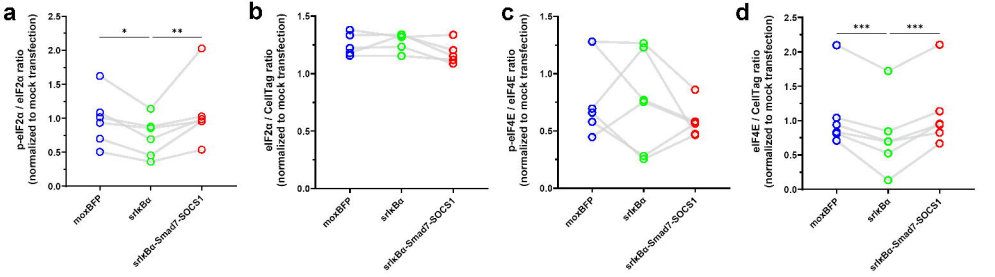
a
p-eIF2α / eIF2α ratio
(normalized to mock transfection)
2.5
2.0
1.5
1.0
0.5
0.0
*
**
moxBFP
srkBα
srkBα-Smad7-SOCS1
b
eIF2α / CellTag ratio
(normalized to mock transfection)
1.5
1.0
0.5
0.0
moxBFP
srkBα
srkBα-Smad7-SOCS1
c
p-eIF4E / eIF4E ratio
(normalized to mock transfection)
1.0
0.5
0.0
moxBFP
srkBα
srkBα-Smad7-SOCS1
d
eIF4E / CellTag ratio
(normalized to mock transfection)
2.5
2.0
1.5
1.0
0.5
0.0
***
***
moxBFP
srkBα
srkBα-Smad7-SOCS1

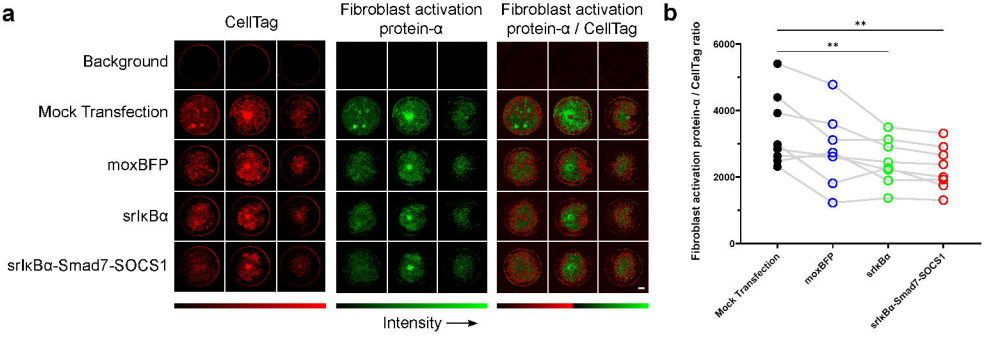
a
CellTag
Fibroblast activation protein-α
Fibroblast activation protein-α / CellTag
Background
Mock Transfection
moxBFP
srIκBα
srIκBα-Smad7-SOCS1
Intensity
b
Fibroblast activation protein-α / CellTag ratio
6000
4000
2000
0
**
**
Mock Transfection
moxBFP
srIκBα
srIκBα-Smad7-SOCS1

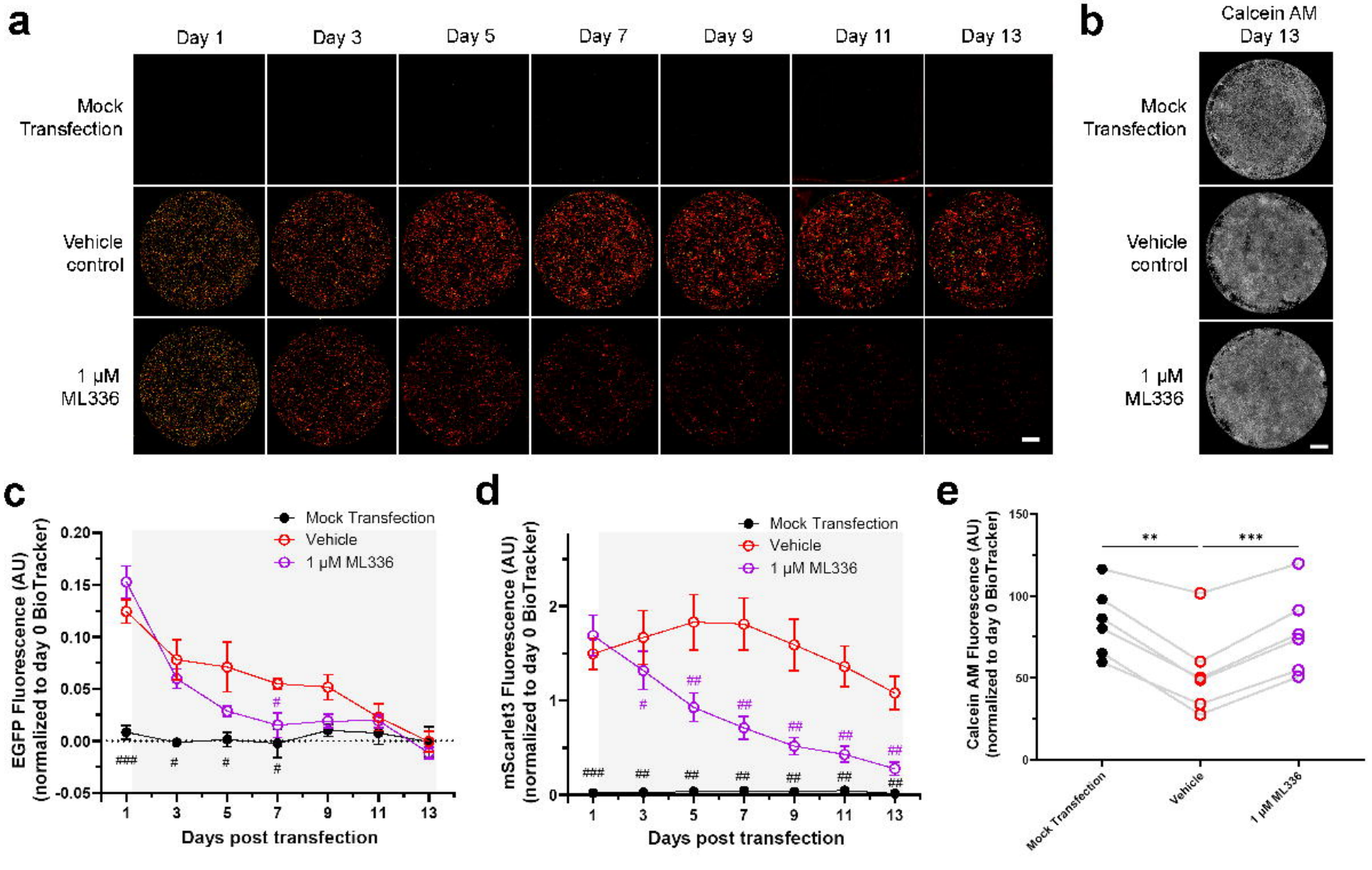
a
Day 1
Day 3
Day 5
Day 7
Day 9
Day 11
Day 13
Mock Transfection
Vehicle control
1 μM ML336
b
Calcein AM Day 13
Mock Transfection
Vehicle control
1 μM ML336
c
Mock Transfection
Vehicle
1 μM ML336
EGFP Fluorescence (AU) (normalized to day 0 BioTracker)
Days post transfection
d
Mock Transfection
Vehicle
1 μM ML336
mScarlet3 Fluorescence (AU) (normalized to day 0 BioTracker)
Days post transfection
e
Calcein AM Fluorescence (AU) (normalized to day 0 BioTracker)
Mock Transfection
Vehicle
1 μM ML336

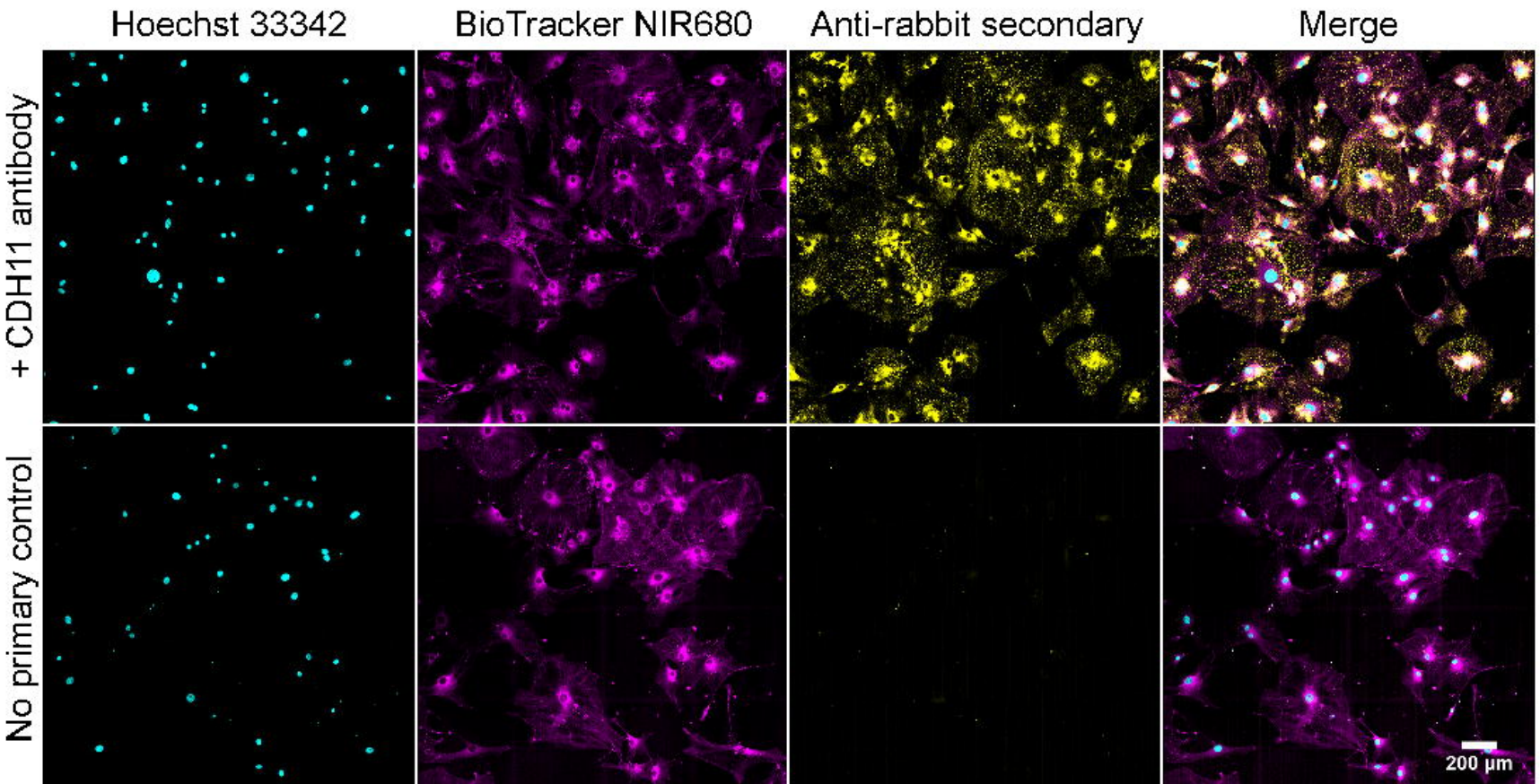
Hoechst 33342
BioTracker NIR680
Anti-rabbit secondary
Merge
+ CDH11 antibody
No primary control
200 µm

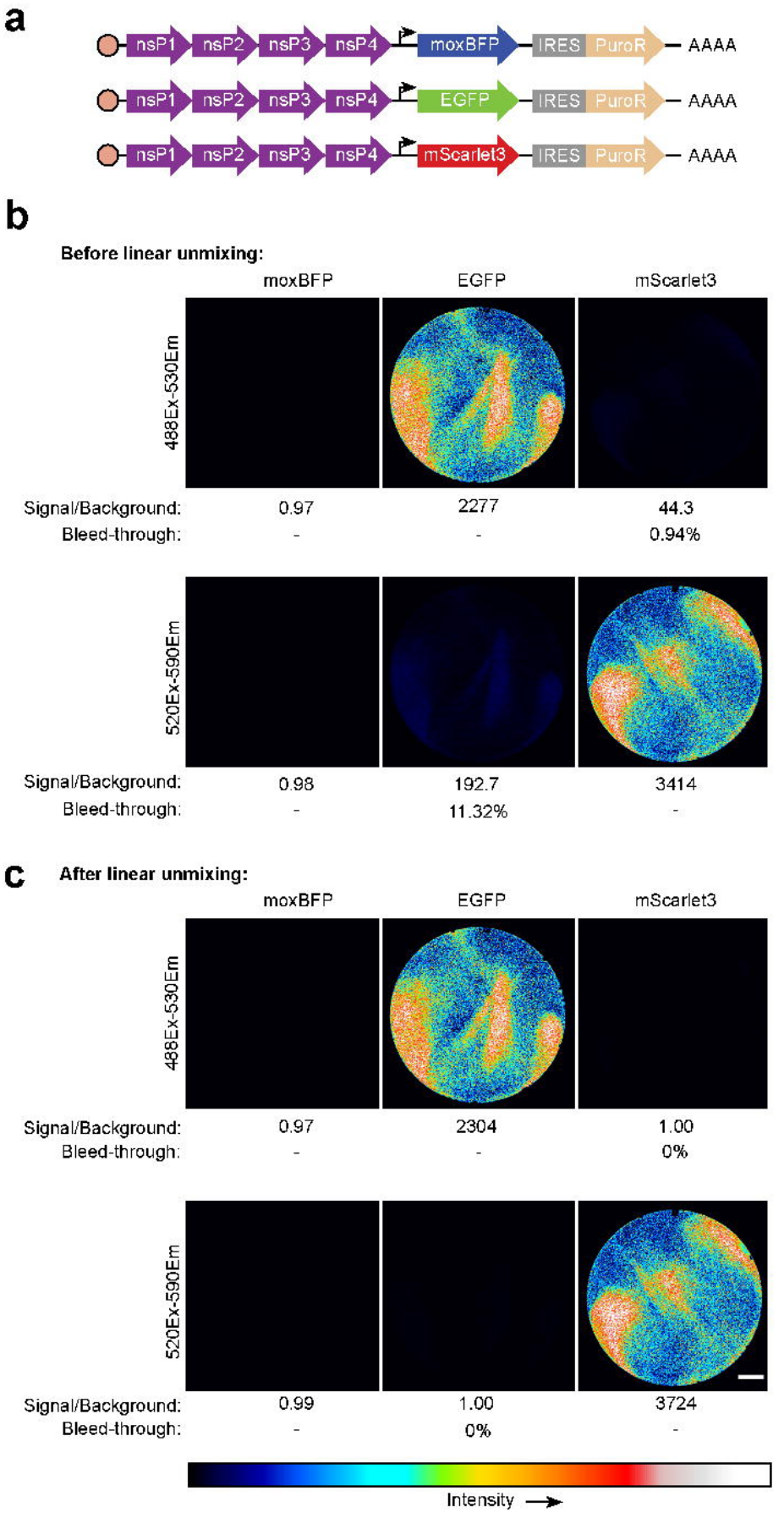
a
nsP1
nsP2
nsP3
nsP4
moxBFP
EGFP
mScarlet3
IRES
PuroR
AAAA
b
Before linear unmixing:
moxBFP
EGFP
mScarlet3
488Ex-530Em
Signal/Background:
0.97
2277
44.3
Bleed-through:
-
-
0.94%
520Ex-590Em
Signal/Background:
0.98
192.7
3414
Bleed-through:
-
11.32%
-
c
After linear unmixing:
moxBFP
EGFP
mScarlet3
488Ex-530Em
Signal/Background:
0.97
2304
1.00
Bleed-through:
-
-
0%
520Ex-590Em
Signal/Background:
0.99
1.00
3724
Bleed-through:
-
0%
-
Intensity

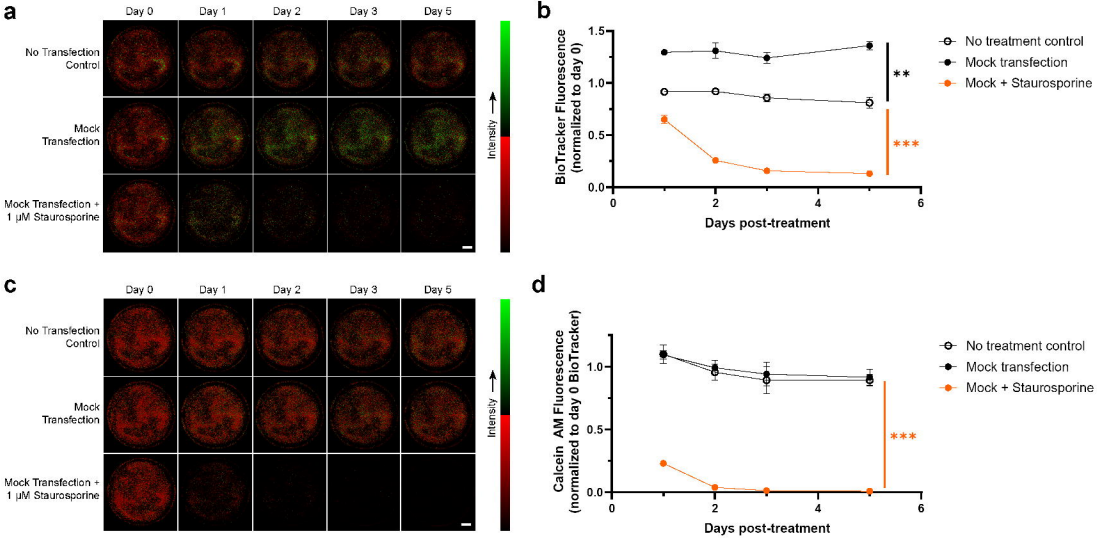
a
Day 0
Day 1
Day 2
Day 3
Day 5
No Transfection Control
Mock Transfection
Mock Transfection + 1 µM Staurosporine
Intensity
b
BioTracker Fluorescence (normalized to day 0)
1.5
1.0
0.5
0.0
0
2
4
6
Days post-treatment
**
***
No treatment control
Mock transfection
Mock + Staurosporine
c
Day 0
Day 1
Day 2
Day 3
Day 5
No Transfection Control
Mock Transfection
Mock Transfection + 1 µM Staurosporine
Intensity
d
Calcein AM Fluorescence (normalized to day 0 BioTracker)
1.0
0.5
0.0
0
2
4
6
Days post-treatment
***
No treatment control
Mock transfection
Mock + Staurosporine

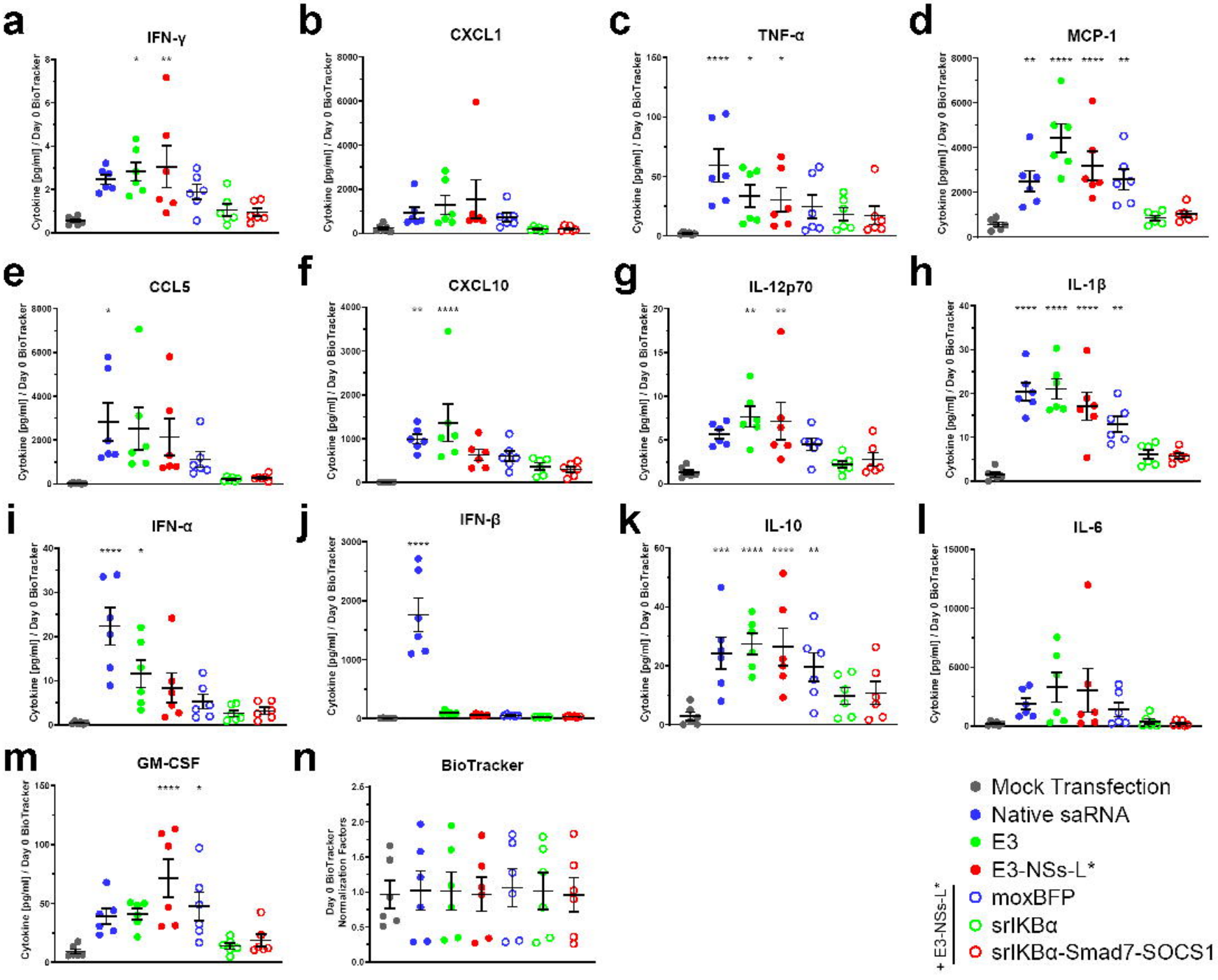
a
IFN-γ
b
CXCL1
c
TNF-α
d
MCP-1
e
CCL5
f
CXCL10
g
IL-12p70
h
IL-1β
i
IFN-α
j
IFN-β
k
IL-10
l
IL-6
m
GM-CSF
n
BioTracker
Cytokine [pg/ml] / Day 0 BioTracker
Day 0 BioTracker Normalization Factors
Mock Transfection
Native saRNA
E3
E3-NSs-L*
moxBFP
srIKBα
srIKBα-Smad7-SOCS1
+ E3-NSs-L*

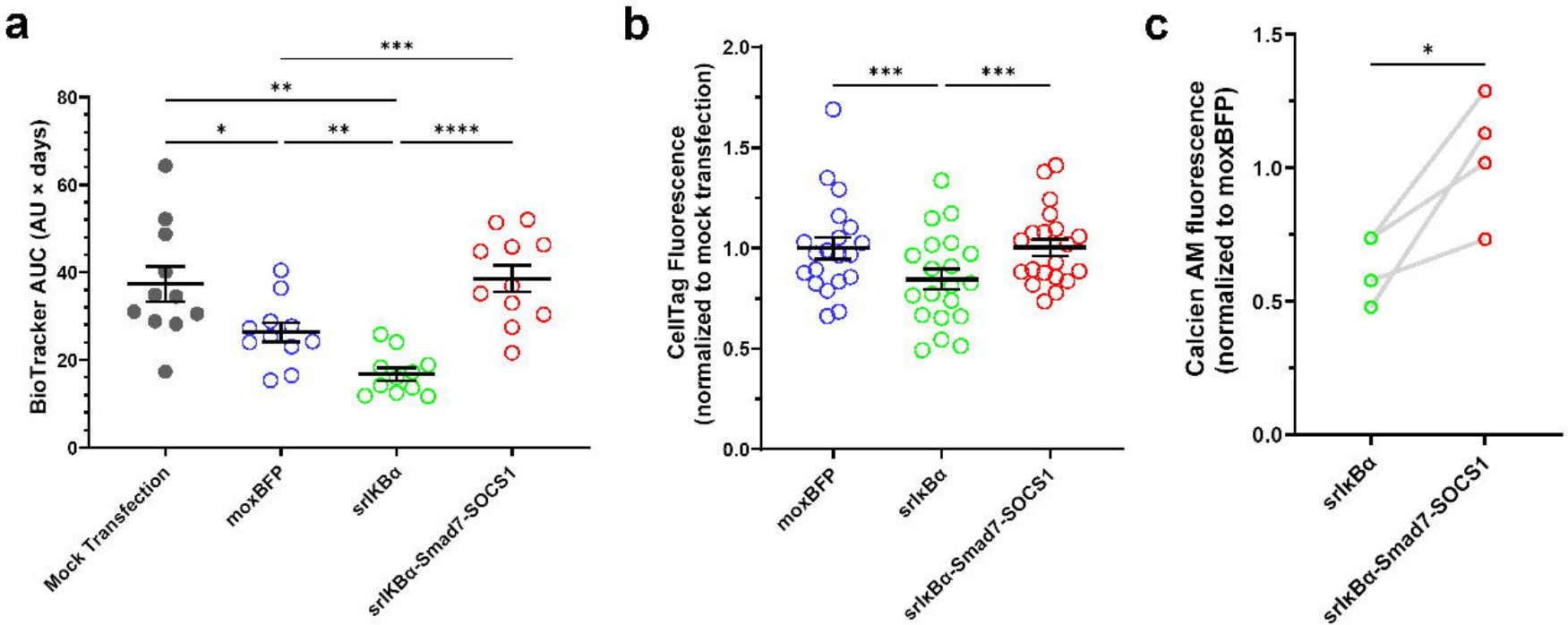
a
BioTracker AUC (AU × days)
0
20
40
60
80
***
**
*
**
****
Mock Transfection
moxBFP
srIKBα
srIKBα-Smad7-SOCS1
b
CellTag Fluorescence
(normalized to mock transfection)
0.0
0.5
1.0
1.5
2.0
***
***
moxBFP
srIκBα
srIκBα-Smad7-SOCS1
c
Calcien AM fluorescence
(normalized to moxBFP)
0.0
0.5
1.0
1.5
*
srIκBα
srIκBα-Smad7-SOCS1